



January 2020

## Coupled Simulation Of Hydraulic Fracturing, Production, And Refracturing For Unconventional Reservoirs

Xincheng Wan

[How does access to this work benefit you? Let us know!](#)

Follow this and additional works at: <https://commons.und.edu/theses>

---

### Recommended Citation

Wan, Xincheng, "Coupled Simulation Of Hydraulic Fracturing, Production, And Refracturing For Unconventional Reservoirs" (2020). *Theses and Dissertations*. 3127.  
<https://commons.und.edu/theses/3127>

This Dissertation is brought to you for free and open access by the Theses, Dissertations, and Senior Projects at UND Scholarly Commons. It has been accepted for inclusion in Theses and Dissertations by an authorized administrator of UND Scholarly Commons. For more information, please contact [und.common@library.und.edu](mailto:und.common@library.und.edu).

COUPLED SIMULATION OF HYDRAULIC FRACTURING, PRODUCTION,  
AND REFRACTURING FOR UNCONVENTIONAL RESERVOIRS

by

**Xincheng Wan**

Bachelor of Resources Exploration Engineering, China University of Petroleum-  
East China, Qingdao, Shandong, China, 2015

Master of Petroleum Engineering, University of Southern California, Los Angeles,  
California, United States, 2017

A Dissertation  
Submitted to the Graduate Faculty  
of the  
University of North Dakota  
In fulfillment of the requirements

for the degree of


Doctor of Philosophy


Grand Forks, North Dakota

May


2020


This dissertation, submitted by Xincheng Wan in partial fulfillment of the requirements for the Degree of Doctor of Philosophy in Petroleum Engineering from the University of North Dakota, has been read by the Faculty Advisory Committee under whom the work has been done and is hereby approved.

DocuSigned by:  
  
440F27A8B8104C1D  
Vamegh Rasouli

DocuSigned by:  
  
1E15210A42159496  
Minou Rabiei

DocuSigned by:  
  
C03B5B854E144E  
Hui Pu

DocuSigned by:  
  
9E1071C501C7407  
Kegang Ling

DocuSigned by:  
  
3302187791948  
Branko Damjanac

\_\_\_\_\_  
Name of Committee Member 5

This dissertation is being submitted by the appointed advisory committee as having met all of the requirements of the School of Graduate Studies at the University of North Dakota and is hereby approved.

DocuSigned by:  
  
730639104228

Chris Nelson  
Dean of the School of Graduate Studies

5/5/2020

\_\_\_\_\_  
Date

## PERMISSION

Title                      Coupled Simulation of Hydraulic Fracturing, Production, and Refracturing  
for unconventional Reservoirs

Department              Petroleum Engineering

Degree                     Doctor of Philosophy

In presenting this document in partial fulfillment of the requirements for a graduate degree from the University of North Dakota, I agree that the library of this University shall make it freely available for inspection. I further agree that permission for extensive copying for scholarly purposes may be granted by the professor who supervised my dissertation work or, in her/his absence, by the Chairperson of the department or the Dean of the Graduate School. It is understood that any copying or publication or other use of this dissertation or part thereof for financial gain shall not be allowed without my written permission. It is also understood that due recognition shall be given to me and to the University of North Dakota in any scholarly use which may be made of any material in my dissertation.

Xincheng Wan

5/4/2020

# Table of Contents

Table of Contents .....	iv
List of Figures .....	vii
List of Tables .....	xi
Acknowledgments.....	xii
Abstract .....	xv
Chapter 1 .....	1
Introduction.....	1
1.1 Background and Problem Statement.....	1
1.2 Objectives .....	4
1.3 Methodology .....	5
1.4 Significance.....	6
1.5 Thesis Structure .....	6
1.6 Summary .....	8
Chapter 2.....	9
Literature Review.....	9
2.1 Evolution of Hydraulic Fracturing.....	9
2.2 Different Parameters affecting Fracture Propagation .....	11
2.3 Hydraulic Fracturing Models .....	13
2.4 Production from Fracture Models.....	18
2.5 Refracturing Models .....	19
2.6 Summary .....	21
Chapter 3.....	22
Lattice Numerical Simulations .....	22
3.1 Introduction.....	22

3.2 Formulation of Lattice Model .....	23
3.2.1 Lattice and Spring Formulation .....	23
3.2.2 Fluid Flow Formulation .....	25
3.2.3 Mechanical Incompressible Flow Formulation .....	25
3.3 Scaling Law .....	26
3.4 Model Verification.....	27
3.4.1 Toughness Verification.....	27
3.4.2 Viscosity dominated regime verification.....	32
3.4.3 Toughness dominated regime verification.....	36
3.5 Summary .....	38
Chapter 4.....	40
Hydraulic Fracturing Simulation .....	40
4.1 Introduction.....	40
4.2 Model Set Up .....	41
4.3 Intermediate Scale Simulations.....	44
4.3.1 Case 1: One-layer model.....	48
4.3.2 Case 2: Three-layer model, different rock properties .....	50
4.3.3 Case 3: Three-layer model, different stresses .....	53
4.3.4 Case 4: Three-layer model, different rock properties and stresses .....	56
4.4 Field Scale Simulation .....	59
4.5 Summary .....	63
Chapter 5.....	64
Integrated Hydraulic Fracturing and Production Model.....	64
5.1 Introduction.....	64
5.2 Multi-stage hydraulic fracturing simulation using lattice model .....	65
5.3 Fracture geometry characterization.....	67
5.3.1 Moving tip clustering algorithm .....	67

5.3.2 Linear regression clustering algorithm .....	70
5.3.3 Fracture identification .....	73
5.4 Gas slippage simulation using LBM.....	77
5.5 Modeling multiple complex hydraulic fractures using EDFM.....	80
5.6 History matching and production prediction .....	80
5.7 Summary .....	89
Chapter 6.....	90
Integrated Model for Refracturing Optimization .....	90
6.1 Introduction.....	90
6.2 Model description .....	91
6.3 Numerical Simulation .....	92
6.3.1 Hydraulic fracturing simulation.....	93
6.3.2 Well production simulation.....	96
6.3.3 Refracturing simulation .....	103
6.3.4 Post refracturing production simulation.....	105
6.4 Summary .....	107
Chapter 7.....	108
Conclusions and Recommendations .....	108
7.1 Conclusions.....	108
7.2 Recommendations and Future Works.....	109
References.....	112

## List of Figures

Figure 2.1 hydraulic fracturing from a vertical well and a horizontal well .....	10
Figure 2.2 Sketch showing: (a) KGD model (Geertsma and Klerk, 1969) and (b) PKN model (Perkins and Kern, 1961; Nordgren, 1972).....	15
Figure 2.3 Mechanism of refracturing due to production induced stress reversal (dash lines represents maximum horizontal stress direction) .....	20
Figure 3.1 Schematic of lattice model showing a joint cuts springs: joint occurs if spring forces reach limit. Blue circle represents lattice nodes (Cundall, 2011). .....	23
Figure 3.2 Sample geometry for toughness test.....	29
Figure 3.3 Apparent toughness $KIC'$ for different lattice resolutions and number of nodes per fracture length .....	31
Figure 3.4 Toughness and viscosity dominated regime verification tests sample geometry .....	33
Figure 3.5 Front view of viscosity dominated regime verification test at 3 s. Aperture (left) and fracture pressure (right) distribution .....	34
Figure 3.6 Comparison of numerical results from viscosity dominated regime verification tests with analytical solutions at three times: (a) aperture profiles, (b) pressure profiles, (c) dimensionless aperture profiles, (d) dimensionless pressure profiles.....	35
Figure 3.7 Front view of toughness dominated regime verification Test at 7.5 s. Aperture (left) and fracture pressure (right) distribution .....	36
Figure 3.8 Comparison of numerical results from toughness dominated regime verification tests with analytical solutions at three times: (a) aperture profiles, (b) pressure profiles, (c) dimensionless aperture profiles, (d) dimensionless pressure profiles.....	37
Figure 4.1 Rock mechanical model (RMM) and rock elastic properties for a well in NPB (Rasouli and Sutherland, 2014).....	42
Figure 4.2 Side (left) and top (right) views of the sample after the hydraulic fracturing experiment (Rasouli and Sutherland, 2014).....	47
Figure 4.3 General model geometry used for simulations .....	47



Figure 4.4 Case 1: one-layer model. Aperture (left) and fracture pressure (right) distribution....	48
Figure 4.5 Aperture contours after 7 second for Case 1: (a) front view; (b) left side view; (c) top view; (d) front view outline; (e) left side view outline; (f) top view outline .....	49
Figure 4.6 Viscosity dominated regime asymptotic solution for aperture contour (left) and outline (right) after 7 second .....	49
Figure 4.7 Case 2: Three-layer model, different rock properties. Aperture (left) and fracture pressure (right) distribution.....	51
Figure 4.8 Aperture contours after 8 second for case 2: (a) front view; (b) left side view; (c) top view; (d) front view outline; (e) left side view outline; (f) top view outline .....	52
Figure 4.9 Case 3. Three-layer model. Aperture (left) and fracture pressure (right) distribution	54
Figure 4.10 Aperture contours after 8 second for case 3: (a) front view; (b) left side view; (c) top view; (d) front view outline; (e) left side view outline; (f) top view outline .....	55
Figure 4.11 Case 4: Three-layer model, different rock properties and stresses. Aperture (left) and fracture pressure (right) distribution .....	57
Figure 4.12 Aperture contours after 8 second hydraulic fracture simulation for case 4: (a) front view; (b) left side view; (c) top view; (d) front view outline; (e) left side view outline; (f) top view outline.....	58
Figure 4.13 Case 5: Field scale simulation. Aperture (left) and fracture pressure (right) distribution .....	60
Figure 4.14 Aperture contours after 2000 second hydraulic fracture simulation for case 5: (a) front view; (b) left side view; (c) top view; (d) front view outline; (e) left side view outline; (f) top view outline.....	61
Figure 4.15 Viscosity dominated regime asymptotic solution for aperture contour (left) and outline (right) after 2000 second.....	62
Figure 5.1 Lattice simulation of multi-stage hydraulic fracturing model.....	66
Figure 5.2 Moving tip clustering algorithm workflow for: (a) $y > W/2$ , (b) $y < W/2$ . .....	69
Figure 5.3 Moving tip clustering algorithm for ( $N = 3$ ) clusters: (a) locate the three injection points, (b) group microcrack dots in range $S1$ and $T1$ into the three clusters and locate fracture “tips” in this range, (c) group microcrack dots in range $S2$ and $T2$ into the three clusters and locate fracture “tips” in this range, (c) group microcrack dots in range $S3$ and $T3$ into the three clusters and locate fracture “tips” in this range. ....	70
Figure 5.4 Linear regression clustering algorithm workflow for: (a) $y > W/2$ , (b) $y < W/2$ . ..	72

Figure 5.5 Linear regression clustering algorithm for ( $N = 3$ ) clusters: (a) locate the three injection points, (b) group microcrack dots in range $S1$ and $T1$ into the three clusters and find a linear fit line segment in the range $S1'$ and $T1'$ , (c) group microcrack dots in range $S2$ and $T2$ into the three clusters and find a linear fit line segment in the range $S2'$ and $T2'$ , (c) group microcrack dots in range $S3$ and $T3$ into the three clusters and find a linear fit line segment in the range $S3'$ and $T3'$ .....	73
Figure 5.6 Multi-stage hydraulic fracturing simulation: 2D cross section plots of (a) microcracks distribution in the hydraulic fracturing simulator, (b) fracture paths based on moving tip clustering algorithm, (c) fracture paths based on linear regression clustering algorithm. ....	75
Figure 5.7 3D fracture paths using (a) moving tip clustering algorithm, (b) linear regression clustering algorithm, (c) DDM method (Yu et al., 2018a). ....	76
Figure 5.8 Lattices and velocities of the D2Q9 model (modified from Sukop and Thorne, 2006). ....	77
Figure 5.9 LBM simulation of changing ratio of apparent matrix permeability over intrinsic matrix permeability due to pressure change with nanopore size of 10 nm (modified from Yu et al., 2018a).....	81
Figure 5.10 Comparison of bottomhole pressure and gas production data using zig-zag and smooth fractures with field data.....	84
Figure 5.11 Comparison of pore pressure distribution after 190 days of production using: (a) zig-zag fractures, (b) smooth fractures.....	85
Figure 5.12 Comparison of pore pressure distribution after 10 years of production using: (a) zig-zag fractures, (b) smooth fractures.....	86
Figure 5.13 Relationship of normalized fracture and matrix permeability over pressure (modified from Yu et al., 2018a). ....	88
Figure 5.14 Impacts of fracture closure, and matrix shrinkage on cumulative gas production in 30 years. ....	88
Figure 6.1 Reservoir model and horizontal well geometry used for simulations .....	93
Figure 6.2 Reservoir model, well location and aperture contours for hydraulic fracture (a) general view, (b) front view, (c) side view, (d) top view .....	96
Figure 6.3 Model geometry (a) and pore pressure contours after 1 year of production: (b) center XZ plane, (c) center YZ plane, (d) center XY plane .....	99

Figure 6.4 Distribution of total stresses before well production at the center XY plane: (a) x direction total stress  $\sigma_{xx}$ , (b) y direction total stress  $\sigma_{yy}$ , (c) tensor field of the minimum horizontal stress ..... 101

Figure 6.5 Distribution of total stresses after 1 year of production at the center XY plane: (a) contour of x direction total stress  $\sigma_{xx}$ , (b) contour of y direction total stress  $\sigma_{yy}$ , (c) tensor field of the minimum horizontal stress..... 102

Figure 6.6 Reservoir model, well location and aperture contour for initial hydraulic fractures and refractures: (a) general view, (b) front view, (c) side view, (d) top view ..... 105

Figure 6.7 pore pressure contours after 1 year of production: (a) center XZ plane, (b) center YZ plane, (c) center XY plane ..... 107

## List of Tables

Table 3.1 Model input parameters and results of toughness tests for five different sample resolutions .....	30
Table 4.1 Rock properties used for simulations.....	43
Table 4.2 Description and input summary for all cases.....	45
Table 4.3 Penetration areas and depths for intermediate scale simulations.....	46
Table 4.4 Penetration areas and depths for field scale simulations .....	60
Table 6.1 Reservoir properties for numerical simulations.....	92

# Acknowledgments

I would like to express my gratitude and appreciation to my advisor Dr. Vamegh Rasouli for his continuous guidance and support during my Ph.D. study. I would miss the time when I spent two or three hours discussing with Dr. Rasouli in his office. His wisdom never failed to help me solve problems and generate new ideas.

I would like to thank my committee member Dr. Hui Pu for offering me an opportunity to pursue Ph.D. degree in University of North Dakota (UND). His support and encouragement gave me my initial motivation to work on hydraulic fracturing simulation. I would like to thank Dr. Branko Damjanac for answering all my questions regarding hydraulic fracturing simulation and providing critical comments and valuable suggestions. I also acknowledge the support of my committee members Dr. Kegang Ling and Dr. Minou Rabiei throughout my Ph.D. study. The support of Dr. Wei Yu for giving me the opportunity to learn building an integrated hydraulic fracturing and production model.

My thanks also go to the member of the Hydraulic Fracturing Research Group at the Department of Petroleum Engineering including Dezhi Qiu, Agustinus Zandy, Foued Badrouchi, Nour Benouadah, Imene Bouchakour, Nejma Djabelkhir, Omar Akash, and Amar Amata. Their comments and suggestions during our frequent group meetings and discussions were really valuable for my research. I look forward to future collaborations with them. I would also like to thank my colleagues Chuncheng Li, Shaojie Zhang, and Xun Zhong for their valuable friendship and help throughout my research study.

Funding support from North Dakota Industrial Commission (NDIC), Energy & Environmental Research Center (EERC), and University of North Dakota (UND) is appreciated. Software and consulting support from Itasca Consulting Group, Inc. and Sim Tech, LLC is acknowledged.

At last I want to thank my beloved Xueling Song who I came to know in 2019 when she came to UND as a visiting scholar. It's a miracle that we fell in love with each other and wish our love would last forever.

To my parents,

who encouraged me to travel 6670 miles away from home

to pursue my dream of becoming a Ph.D.

# Abstract

Horizontal well drilling and multi-stage hydraulic fracturing are two key techniques for the development of unconventional reservoir. However, the production from tight formation is associate with fast depletion of reservoir. When oil price is low, drilling new horizontal wells is not profitable. Creating secondary fractures from existing hydraulic fractured wells, i.e., refracture is an alternative method to increase stimulated reservoir volume (SRV) and gain additional production from existing hydraulic fractured wells. To optimize refracturing well selection and operation, it's of economic importance to acquire knowledge from initial hydraulic fracturing operation, production history, and refracturing design perspectives. This initiated the idea of this research to develop an integrated hydraulic fracturing, production, and refracturing model.

This research work mainly comprises of three sections. In the first section, hydraulic fracturing models were built using XSite software, a lattice-based simulator, to analyze the effect of changing rock properties and in-situ stresses on fracture propagation in a layered reservoir. The challenge was to quantify degree of fracture containment using the hydraulic fracturing simulator. To overcome this fracture aperture contours were obtained to quantify fracture containment with two proposed penetration parameters. The modeling results suggest that brittle rocks favor vertical migration of hydraulic fracture, while increasing minimum horizontal stress tends to inhibit vertical growth of hydraulic fracture and lead to containment at layer interface.

In the Second part of this study, an innovative integrated multi-stage hydraulic fracturing and production model was built for a shale gas reservoir. The challenge was to utilize distributed fracture data presented from the lattice-based hydraulic fracturing simulator for history matching



in the reservoir simulator. To identify fracture geometry, a moving tip clustering and linear regression clustering algorithms were developed to discretize distributed fracture data points using multiple crack segments. The former algorithm is prone to capture fracture with microcracks that contribute to SRV, thus contributing to higher simulated production. The latter algorithm mainly captures the major fracture path without consideration of microcracks. The modeling results also suggest that gas slippage, matrix shrinkage, and fracture closure play important roles in shale gas production.

In the third section, an innovative hydraulic fracturing, production, refracturing, and post-refracturing production model was developed. The challenge in this part was to simulate refracture propagation based on existing fracture geometry and pore pressure distribution with higher accuracy and efficiency. A model was built by simulating the fracture and refracture propagation in XSite and modeling reservoir depletion and post refracturing reservoir depletion in the continuum mechanism based simulator. The results suggest the propagation of refractures is driven by proppant and depletion induced stress shadow and contributes to larger SRV and higher hydrocarbon production.

The proposed algorithms and integrated models can potentially be applied in the field for better refracturing design to enhance ultimate recovery of oil and gas.

# Chapter 1

## Introduction

### 1.1 Background and Problem Statement

Horizontal well drilling and multi-stage hydraulic fracturing have contributed to the boom of the oil and gas production in unconventional tight formations. These techniques have also enabled the U.S. to reclaim the largest oil production country in the world since 2013 (U.S. Energy Information Administration, 2019a). Horizontal well production has gradually dominated unconventional oil and gas production in the U.S since 2009, by the end of 2018, more than 100,000 horizontal wells had been drilled in the U.S. tight formations, contributing to more than 96% of tight oil and shale gas production (U.S. Energy Information Administration, 2019b).

Hydraulic fracturing is the primary technique to enhance oil and gas production in unconventional reservoirs. In order to fully understand the mechanisms of hydraulic fracturing, numerous laboratory experiments have been conducted (Lamont and Jessen, 1963; Blanton, 1982; Rubin, 1983; Chang, 2004; Bohloli, 2006; Germanovich, L. N. et al., 2012; Sarmadivaleh, 2012; Gwaba et al., 2019). However, the laboratory tests are limited in scale. The relative homogeneous and intact rock sample in the laboratory may not fully represent the relative heterogeneous reservoir with geological features and natural fractures. The hydraulic fracturing pumping schedule in the field cannot be applied to the laboratory either. To simulate hydraulic fracturing at different scales,

scaling law is needed to make sure the fracture propagates in the same propagation regime (Savitski and Detournay, 2002). Analytical and numerical models have been proposed for studying hydraulic fracturing in various sizes from laboratory to field scale (Perkins and Kern, 1961; Geertsma and Klerk, 1969; Nordgren, 1972; Settari and Cleary, 1982; Palmer and Carroll Jr., 1983). However, these models have simplified assumptions for either fracture geometry or pressure distribution.

The propagation of hydraulic fracture is affected by rock properties and in-situ stresses. The change of these factors have great impacts on the fracture geometry, pressure and propagation direction as well as the interaction between hydraulic and natural fractures, consequently affecting oil and gas production from the tight formations. It is of economic significance to characterize and quantify the influence of these parameters. The effects of Young's modulus, Poisson's ratio, and in-situ stresses on fracture containment have been studied by laboratory experiments as well as analytical and numerical solutions (Hucka and Das, 1974; Teufel and Clark, 1981; Warpinski et al., 1981; Luan et al., 2014; Wang et al., 2015; Zhang et al., 2016; Gholami et al., 2016). However, the combined effect of rock properties and in-situ stresses on fracture containment needs further investigation.

Conventional hydraulic fracturing method is to drill a vertical well and create a single fracture at the bottom of the wellbore. This approach increases stimulated reservoir volume (SRV) near the fracture, but it is not efficient for the development of the unconventional reservoirs because large reservoir volumes between vertical wells would be unstimulated. Despite higher expense is needed to drill a horizontal well than a vertical well, but to produce the same amount of oil, fewer horizontal wells are needed compared to vertical wells (Joshi, 2003). One important factor that

should be addressed for multi-stage hydraulic fracturing is the stress shadow effect, which is the change of stresses due to the propagation of one hydraulic fracture. The stress shadow of the previous stage fractures leads to turning of the next stage fracture. The effect is mainly caused by small fracture spacing as well as large net pressure (Warpinski and Branagan, 1989; Nagel et al., 2013). Conventional reservoir simulation of multi-stage hydraulic fractures usually assumes fractures of different stages have planar geometry with constant fracture length, however, this method reduces the complexity of fracture geometry and potentially gives rise to inappropriate estimation of fracture production. Some studies transferred complex fracture geometry into reservoir simulator for production simulation (Mirzaei and Cipolla, 2012; Moïnfar et al., 2013; Du et al., 2016), but the method of refining grids near fracture usually results in slower production simulation.

Despite that multi-stage hydraulic fracturing contributes to larger fracture conductivity, greater stimulated reservoir volume (SRV), and more production, the technique also leads to greater production decline and reservoir depletion. Refracturing is a new technique that allows operators to enhance production from existing hydraulic fractured wells. It is known that the reservoir depletion near fractures creates stress reversal regime (Warpinski and Branagan, 1989; Sharma, 2013). Some recent studies have investigated numerically the impact of depletion induced stress reversal on refracture propagation (Sharma, 2013; Huang et al., 2016; Kumar et al., 2018), but for the purpose of optimizing refracturing operation and improving secondary production from refractures, an integrated hydraulic fracturing – production – refracturing model is needed.

## 1.2 Objectives

The ultimate goal of this study is to build an integrated model for hydraulic fracturing, production, and refracturing for unconventional reservoirs. Therefore, the objectives of this study are summarized as below.

1. Review the laboratory, analytical and numerical approaches for hydraulic fracturing, fracture production, and refracturing. The advantages and limitations of each method will be discussed.
2. Study the impacts of rock properties and in-situ stresses on hydraulic fracture propagation; review the influence of existing fracture geometry and production time on refracture propagation and its production.
3. Compare the results of the lattice-based hydraulic fracturing models versus analytical solutions; apply scaling law to simulate hydraulic fracture containment in layered reservoir with various rock properties and in-situ stresses.
5. Simulate multi-stage hydraulic fracturing and the sequential well production; investigate influence of fracture closure, matrix closure, gas slippage, etc. on production from fractures.
6. Build an integrated hydraulic fracturing – production – refracturing model; study the impact of depletion induced stress reversal on refracture propagation.

### **1.3 Methodology**

Laboratory and field data will be obtained, analytical and numerical approaches will be applied, innovative parameters and algorithms will be proposed, to achieve the goal and objectives of this study. They are briefly summarized here.

1. A lattice based hydraulic fracturing simulator XSite will be used for hydraulic fracturing simulation. Tip asymptotic solutions of toughness and viscosity dominated regimes will be used to verify the corresponding numerical results.
2. Penetration parameters including penetration length and area will be proposed to quantify degree of fracture containment in each layer.
3. Innovative data mining algorithms including moving tip clustering and linear regression clustering algorithms will be proposed, in order to discretize fracture geometry obtained from the lattice based hydraulic fracturing simulator into multiple linear fracture segments.
4. For simulation of production from a multi-stage hydraulic fracturing well, a non-intrusive Embedded Discrete Fracture Model (EDFM) method will be used to transfer fracture geometry into the third party reservoir simulator CMG for shale gas production and prediction.
5. Gas slippage effect contributes to higher production during late stage fracture production. This effect will be simulated using Lattice-Boltzmann Method (LBM).
6. FLAC3D, a general-purpose software widely used in civil, mining and mechanical engineering, will be used for simulation of shale oil production, the resultant pressure distribution will be exported back to XSite for refracturing simulation.

## **1.4 Significance**

The innovations of this research work are multi fold including the followings:

1. A lattice based hydraulic fracturing simulator was used for building hydraulic fracturing models at different scales. The use of this method with XSite software is relatively new.
2. Penetrative parameters were proposed to characterize fracture containment in different layers.
3. Data mining algorithms including moving tip clustering and linear regression clustering algorithms were proposed to characterize complex fracture geometry.
4. An innovative XSite – EDFM – CMG method was proposed for simulation of hydraulic fracturing and shale gas production analysis.
5. An integrated hydraulic fracturing, production, and refracturing model method was proposed using XSite and FLAC3D for refracturing optimization.

## **1.5 Thesis Structure**

This dissertation is composed of 7 chapters.

Chapter 1 introduces the background of hydraulic fracturing, fracture production, and refracturing simulations and also provides limitations of previous laboratory, analytical, and numerical studies. It also consists of goal and objectives, methodology, and significance of this study.

Chapter 2 briefly reviews the history of hydraulic fracturing and refracturing. A summary of different parameters impacting hydraulic fracture propagation and its interaction with natural fractures is presented. Different analytical and numerical hydraulic fracturing models will be

discussed. Review of production from hydraulic fractures modeling will be given. Refracturing concepts and recent refracturing modeling techniques will be also discussed.

Chapter 3 summarizes features of XSite and theory of lattice based simulation. It verifies the results of the lattice based hydraulic fracturing models versus classical hydraulic models. Theory of scaling law will be explained. Examples of lattice based hydraulic fracturing models for toughness dominated regime and viscosity dominated regime will be presented.

Chapter 4 provides hydraulic fracturing simulations regarding fracture containments, as an example, in the North Perth Basin. Four the intermediate scale, models will be built using scaling law. One field scale model will be built accounting for in-situ stresses and rock properties. Penetration parameters will be utilized to quantify degree of fracture containment.

Chapter 5 presents an integrated multi-stage hydraulic fracturing and fracture production model for Marcellus shale gas reservoir. Moving tip clustering and linear regression clustering fracture identification algorithms will be proposed and utilized for fracture discretization. Non-intrusive EDFM method will be introduced and utilized for transferring fracture to CMG software to perform production simulation and prediction.

Chapter 6 presents an integrated hydraulic fracturing, production and refracturing model for Shale oil production in Bakken. Development of the integrated model using XSite and FLAC3D will be presented. Impact of production induced stress reversal on refracture propagation will be discussed.

Chapter 7 summarize the results and discussions from this study. Recommendations for field applications and future research will be presented.



## **1.6 Summary**

This Chapter presented a brief summary of the problems that will be studied in this research work. Modeling of hydraulic fracturing, production, and refracturing were briefly introduced. Limitations of laboratory studies and previous analytical and numerical studies were discussed. The main goal and detailed objectives of this study were outlined. The methodology, significance, and the structure of this dissertation were also presented.

The next Chapter will provide a detailed review of the past studies investigating the impact of various parameters on hydraulic fracture propagation. Detailed discussion of advantages and shortcomings of previous hydraulic fracturing, fracture production, and refracturing models will be presented.

# Chapter 2

## Literature Review

### 2.1 Evolution of Hydraulic Fracturing

Hydraulic fracturing is the primary technique for stimulating the tight formations. The first endeavor of fracking a well dated back to 1864, when Colonel Edward August Leonard Roberts “shot a well” for the first time using gunpowder and nitroglycerin. This method is called torpedo technology, which is highly dangerous. Even a small mistake in operation may lead to severe injury or fatality (Adomites, 2011). The birth of hydraulic fracturing was in 1949 when J.B. Clark published a paper regarding stimulating wells using hydraulic process with Stanolind Oil & Gas Company. The hydraulic process is comprised of injection of viscous fluids with proppants to create hydraulic fractures in the formation as well as viscosity reduction of the injection fluids during prior to well production (Clark, 1949; Testa, 2016).

Horizontal well drilling and multi-stage hydraulic fracturing are two important techniques for the development of unconventional reservoirs (Lecampion et al., 2015; Roussel and Sharma, 2011). By creating multiple transverse fractures in a horizontal well, fewer vertical wells are needed to create same number of fractures. As shown in Figure 2.1, a horizontal well is capable of creating multiple fractures and significantly increasing SRV, contributing to much more oil or gas production than that of a vertical well. This is despite the fact that the stress shadow effect may

inhibit growth of some fractures in a horizontal well. The production from the rest of fractures tends to save the budget for drilling new vertical wells.

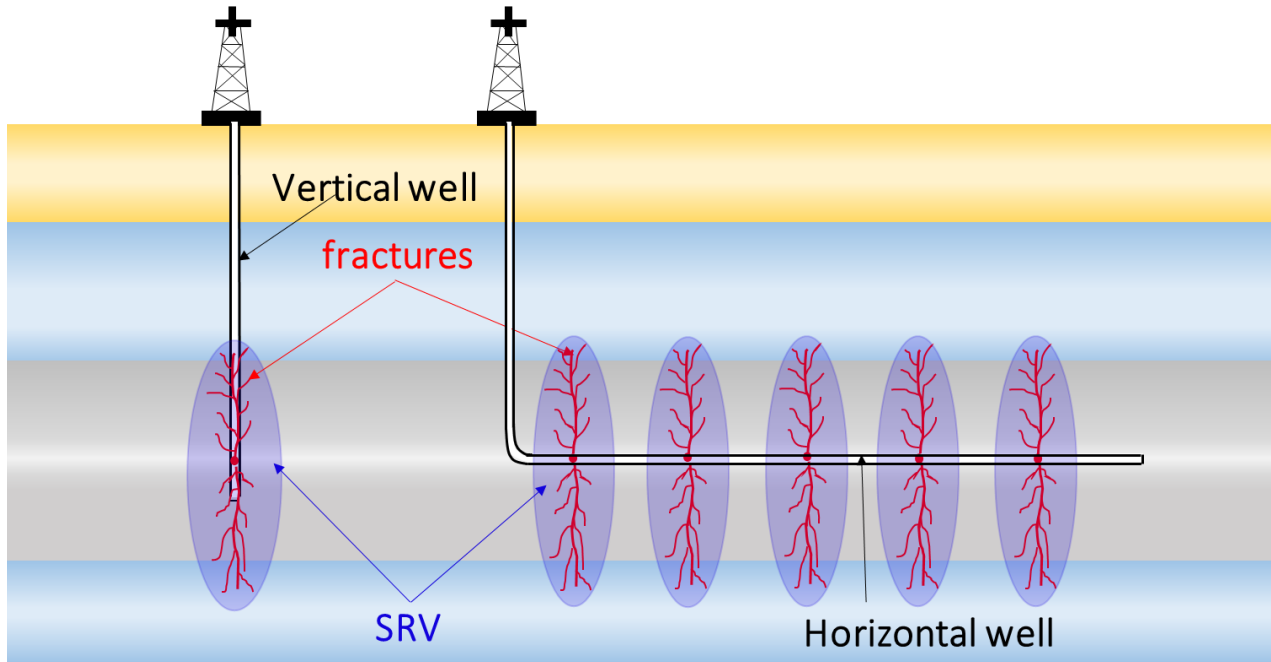


Figure 2.1 hydraulic fracturing from a vertical well and a horizontal well

The first recorded horizontal oil well was completed in 1929 (Testa, 2016). However, it was not until the early 1980s that commercial achievements were obtained from horizontal well drilling by the French oil company Elf Aquitaine (Testa, 2016). By 2004, only 15% of U.S crude oil in tight formations was produced from horizontal wells (U.S. Energy Information Administration, 2019b). The primary factor that held back applications of horizontal well drilling might come from the high risk. In 2003, the commercial success rate for horizontal well drilling in the U.S was approximately 65% (Josh, 2003). With the improvement of drilling technologies and better understanding of the unconventional reservoirs, horizontal wells have been dominating oil and gas production from unconventional reservoirs since 2008. By the end of 2018, more than 96% of U.S

crude oil and gas production from unconventional reservoirs were produced by horizontal wells (U.S. Energy Information Administration, 2019b).

Despite horizontal well drilling and multi-stage hydraulic fracturing may allow operators to obtain huge amount of oil or gas at the early production period, fast production decline at the later period may lead to loss of revenues. Besides, the multiple fractures created along a horizontal well may have undesirable fracture geometry or poor fracture conductivity. When the oil price is low, these factors tend to inhibit operators from drilling costly horizontal wells, therefore, refracturing an existing well is an alternative approach for re-stimulating the reservoirs with lower expenses. The mechanisms of refracturing includes improving existing hydraulic fractures, re-energizing natural fractures, and creating new fractures (Vincent, 2010). The first refracturing treatment by dated back to 1953 in the Southern Oklahoma and North Central Texas region (Sallee and Rugg, 1953). The treatment was conducted by sequential fracturing with different pumping schedule. After that, the interest in refracturing grew. In 1970, approximately 35% of the 500,000 fracturing treatments were re-stimulated (Coulter and Menzie, 1973). However, the interest dropped during 1990's with less than 3% of hydraulic fracturing jobs directed to refracturing (Vincent, 2010). This might be the result of relatively low cost of performing a hydraulic fracturing treatment in a vertical well. With increasing interest in horizontal well drilling and multi-stage hydraulic fracturing for the development of unconventional reservoir, refracturing gradually regained attention from industry.

## **2.2 Different Parameters affecting Fracture Propagation**

The propagation of hydraulic fractures at the depth of thousands of feet underground is influenced by many factors. Mechanical properties of the rock matrix, stress and temperature distribution,

pumping schedule and presence of natural fractures would cause geometry changing or reorientation of fracture propagation (Gholami et al., 2016; Ghassemi et al., 2008; Dahi-Taleghani, 2009). It is of economic interest to have a good knowledge of the impact of these factors on the fracture propagation in order to maximize the fold of increase in production by optimizing the design parameters.

The deep formations are inhomogeneous and anisotropic. Brittle rocks with large Young's modulus and small Poisson's ratio favor fracture propagation and generate large micro fracture network around the main fracture plane, which effectively enhances production from tight formations (Hucka and Das, 1974; Luan et al., 2014; Zhang et al., 2016; Wang et al., 2015; Gholami et al., 2016; Feng et al., 2020). In some cases, the breakthrough of the propagating fracture into the surrounding layers is undesirable. Fracture propagation into the overburden will unseal the cap rock and cause the release of the hydrocarbon which may present environmental concerns (Ingram and Urai, 1999). As another example, fracture breakthrough into water-bearing formations will increase water cut dramatically (Teufel and Clark, 1981). The contrast of minimum horizontal stress between the two layers governs vertical containment of the hydraulic fracture. Fracture can be contained if the minimum horizontal stress is larger in the adjacent layer, whereas it can break into the new layer if it faces a lower minimum horizontal stress (Teufel and Clark, 1981).

The aperture changes during the hydraulic fracturing process has been widely studied (Crouch and Starfield, 1983; Garagash and Detournay, 1999; Ghassemi et al., 2008). The two main theories governing the change of hydraulic fracture aperture are the Poiseuille's law and the theory of linear elasticity. Poroelastic and thermoelastic effects also play an important role on the change of

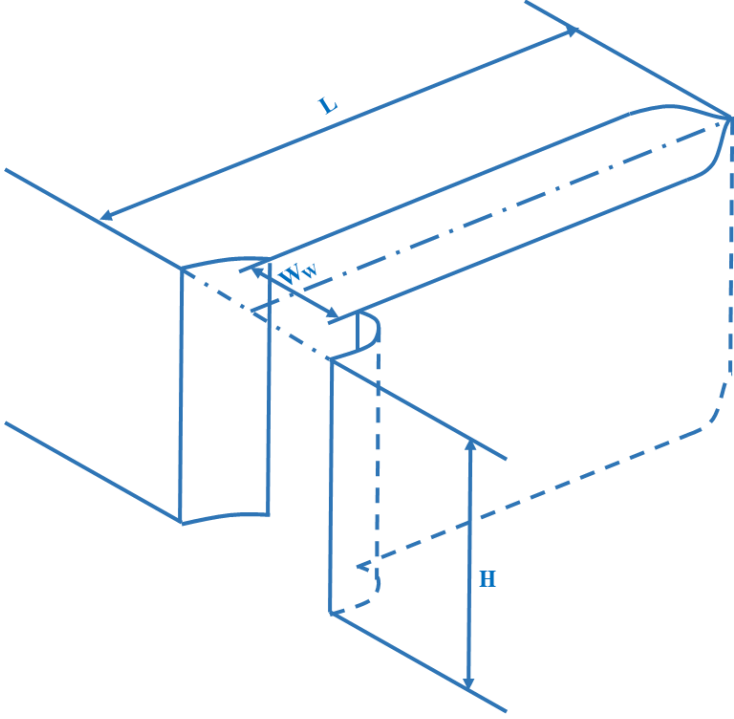
hydraulic fracture aperture. Due to fluid leak-off into the formation, the pressure in the hydraulic fractures drop, leading to a decrease in fracture aperture (Detournay et al., 1989). If the reservoir is deep with high temperature, when the cold hydraulic fracturing fluid is injected, the rock matrix contracts, leading to expansion of hydraulic fractures (Perkins, 1985).

The interaction between hydraulic fracture and natural fractures is another factor that significantly affects propagation of hydraulic fractures. Four major interaction mechanisms are known as opening, crossing, arresting and offsetting. The mechanisms are governed by the properties of the rock matrix and natural fractures, the stress distribution, orientation of natural fractures, fracturing fluids properties, etc. (Sarmadivaleh, 2012). Capillary effect may also affect hydraulic fracture and natural fracture interaction, small natural fractures with strong fracturing fluid wettability is easy to be initiated by hydraulic fractures. Furthermore, several studies suggest that small natural fractures may have either positive or adverse impacts on shale gas production due to capillary effect. (Cheng, 2012; Wang et al., 2016; Chen et al., 2018).

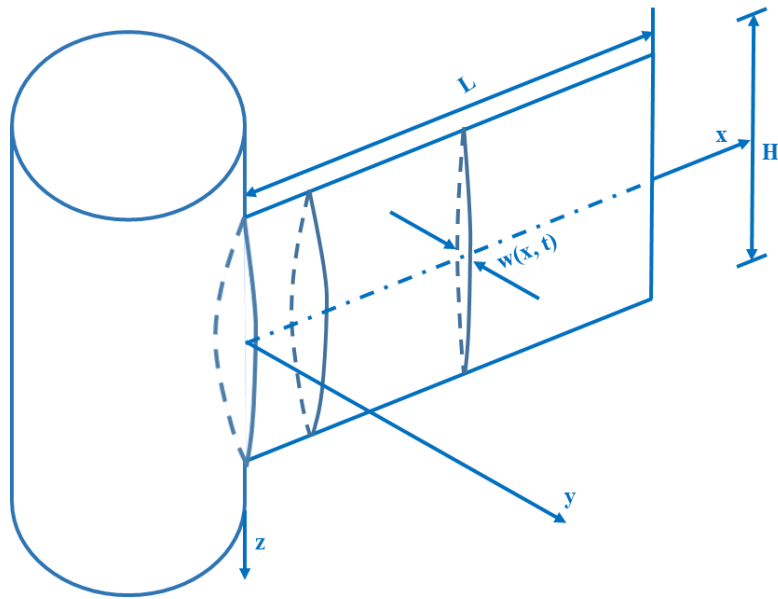
### **2.3 Hydraulic Fracturing Models**

Two well-known 2D classical hydraulic fracturing models are Khristianovic-Geertsma-de Klerk (KGD) model (Geertsma and Klerk, 1969) and Perkins-Kern-Nordgren (PKN) model (Perkins and Kern, 1961; Nordgren, 1972), as shown in Fig. 3. Both models assume that the fracture propagates only in length direction without change of height. This assumption is only valid when the growth of fracture is contained in one layer, but could not show change of fracture geometry in multiple layers with various rock mechanical properties and in-situ stresses. Another assumption for PKN and KGD models is that the fracture is planar and is perpendicular to the minimum principal stress.

This assumption limits their application of modeling fracture propagation under complex stress field, such as stress shadow.



(a)



(b)

Figure 2.2 Sketch showing: (a) KGD model (Geertsma and Klerk, 1969) and (b) PKN model (Perkins and Kern, 1961; Nordgren, 1972)

To analyze the complexity of hydraulic fracture propagation in layered geology with variable rock properties and in-situ stresses, numerous numerical models have been developed. Pseudo-Three-Dimensional (P3D) model, developed in 1980s, is an efficient method to describe vertical propagation of hydraulic fractures (Settari and Cleary, 1982; Palmer and Carroll Jr., 1983). As an extension of the PKN model, P3D model also assumes fracture height to be much less than fracture length, but it allows fracture height to grow. Finite element formulations for modeling of hydraulic fracture propagation in layered reservoirs were proposed in 1990 (Advani et al., 1990). This model is a planar 3D (PL3D) model. It is more accurate than P3D because it does not need horizontal stresses in different layers to be monotonic function of depth, although it requires greater computational efforts (Adachi et al., 2007).



Both P3D and finite element PL3D models solved the problem of vertical growth of hydraulic fracture into the upper and lower layers, however, they are limited to planar fracture geometry. Non-planar fracture geometry is expected when the principal stresses ahead of fracture tip rotate. A two-dimensional displacement discontinuity method (2D DDM) introduces coordinate transformation for pressurized crack problems (Crouch and Starfield, 1983). The method allows fracture reorientation under certain stress conditions. Shou (1997) extended 2D DDM into three-dimensional displacement discontinuity method (3D DDM) (Shou et al., 1997). To improve computational efficiency, Olson (2004) introduced correlation factor  $G$  to 2D DDM to compensate the three-dimensional effect of a limited-height fracture (Olson, 2004). This pseudo three-dimensional displacement discontinuity method (P3D DDM) can solve single fracture propagation but is inadequate to deal with multiple fractures interaction (Wu, 2014). Finite element method (FEM) modeling of fracture reorientation requires remeshing and is computationally expensive (Martha et al., 1993). To improve computational efficiency, extended finite element method (XFEM) was introduced (Moës et al., 1999). XFEM method applied enrichment function to avoid remeshing, and it was used to simulate fracture reorientation and interaction between hydraulic fractures and natural fractures (Dahi-Taleghani, 2009; Wang, 2015).

The mentioned methods P3D, PL3D, DDM, FEM, and XFEM are based on continuum mechanics. They tend to encounter difficulties in modeling non-linear situations such as block rotation, slip, and self-propping. For instance, it's difficult to represent permeability change due to block rotation in these methods (Dusseault and McLennan, 2011). The introduction of distinct element method (DEM) (Cundall, 1971) lent another methodology to study fracture propagation in a more realistic approach. Initially, the method aimed at solving general rock and soil mechanics problems such as

analyzing particle behavior under loading and unloading conditions (Cundall and Strack, 1979). Later, bonded particle model (BPM) was developed and incorporated into the DEM to simulate crack propagation as coalescence of microcracks represented by broken bonds (Potyondy and Cundall, 2004). To simulate jointed rock mass, the synthetic rock mass (SRM) model was developed by applying BPM to represent intact rock with multiple joints. Each joint is represented using smooth-joint contact model (SJM) (Pierce et al., 2007; Ivars et al., 2011). DEM and SRM concepts have been used in general purpose codes PFC2D and PFC3D, which are assembled by circular/spherical particles, to represent rock matrix (Itasca, 2008a; Itasca, 2008b).

Recently, the concepts have been implemented into a hydraulic fracturing simulator XSite (Damjanac et al., 2011), which applies a lattice model to represent rock matrix and simulates hydraulic fracturing process. The point masses connected by springs in the lattice model of the hydraulic fracturing simulator replace finite-size particles and contacts of PFC2D/PFC3D, resulting in higher computational efficiency (Damjanac et al., 2016). The implementation of SJM enables the hydraulic fracturing simulator to overcome the conventional limitation in simulating hydraulic fracture propagation under complex natural fracture conditions (Damjanac et al., 2011; Damjanac et al., 2016). The lattice based hydraulic fracturing simulator has been used in some recent studies for different applications of hydraulic fracturing (Xing et al., 2018; Bakhshi et al., 2018; Fu and Bungler, 2019; Fu et al., 2019; Yildirim et al., 2019; Djabelkhir et al., 2019; Zhang et al., 2019).

## 2.4 Production from Fracture Models

In order to estimate the effectiveness of fractures, it is of importance to use appropriate fracture geometry to perform production simulation (Cipolla and Wallace, 2014; Tripoppoom et al., 2020). The simplified method to simulate production decline in a horizontal well with multiple fractures is to assume that the fractures are planar and transverse with constant length. This method has been widely applied for production history matching (Yu, Luo et al., 2014; Jin et al., 2017; Fan et al., 2010; Iwere et al., 2012). However, the propagation of one fracture would lead to reorientation of other fractures nearby due to the effect of stress shadow (Warpinski and Branagan, 1989). Some methods have been proposed to simulate production decline for reservoirs with complex fracture geometry (Mirzaei and Cipolla, 2012; Moinfar et al., 2013; Du et al., 2016). To allow faster and more accurate reservoir simulation, a non-intrusive embedded discrete fracture model (EDFM) method was proposed to embed complex fracture geometry into a third-party reservoir simulator to simulate well production (Xu, 2015; Xu et al., 2017a; Xu et al., 2017b).

In addition to capture the non-planar fracture geometry, non-Darcy flow and gas transport mechanisms should be included in reservoir simulation of shale gas production (Yu et al., 2017). In conventional gas reservoirs, Darcy's flow dominates gas flow in the porous media (Javadpour et al., 2007). In shale gas reservoirs, gas flow can be characterized by Knudsen diffusion (Freeman et al., 2011). In micropores, Darcy's flow can still be applied, but in nanopores, gas slippage dominates gas flow (Klinkenberg, 1941; Javadpour et al., 2007). For both shale gas and coalbed methane reservoirs, a large amount of gases is adsorbed on the surfaces of the rock matrix. When reservoir is depleted and the reservoir pressure reaches critical desorption pressure, the adsorbed gases are released from the matrix (Ross and Bustin, 2007; Guo, 2013). Both gas slippage and

desorption contribute to larger apparent permeability of rock matrix and additional shale gas production (Javadpour et al., 2007; Yu et al., 2017).

## **2.5 Refracturing Models**

The propagation of fracture depends on the total stresses around the fracture. It is well-known that the fracture propagation direction is perpendicular to the minimum principal stress. For the case of the Bakken Formation, the in-situ minimum horizontal stress ( $\sigma_h$ ) tends to be the minimum principal stress and governs fracture propagation direction. However, reservoir depletion highly affects total stresses. During production, the stress parallel to the fracture plane (in-situ maximum horizontal stress) tends to decrease faster than the stress perpendicular to the fracture plane (in-situ minimum horizontal stress), creating a stress reversal regime (Warpinski and Branagan, 1989; Palmer, 1993) as shown in Figure 2.3. Therefore, refracturing operation allows the secondary fracture to propagate perpendicular to the initial hydraulic fracture.

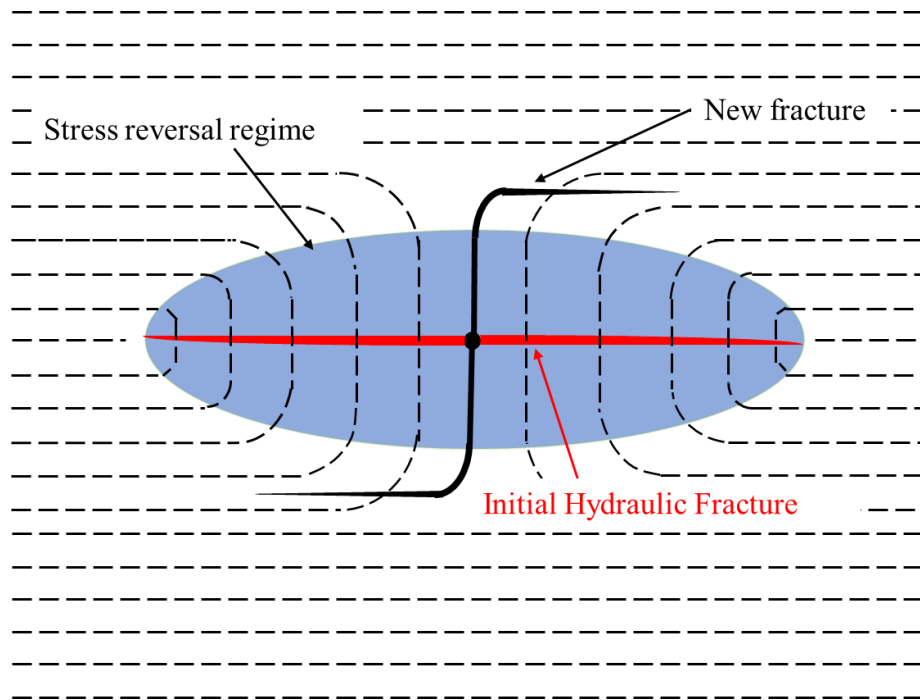


Figure 2.3 Mechanism of refracturing due to production induced stress reversal (dash lines represents maximum horizontal stress direction)

Different numerical studies have been done to investigate the effect of reservoir depletion on the stress reversal regime around a hydraulic fracture. Sharma (2013) built a FLAC3D model to analyze the stress reversal effect for a constant height fracture under different conditions such as boundary, permeability, and rock properties (Sharma, 2013). Huang et al. (2016) combined finite element method (FEM) and cohesive zone method (CZM) and used ABAQUS to simulate fracture propagation and well production of refracturing wells under different reservoir and perforation conditions (Huang et al., 2016). Recent work by Kumar et al. (2018) combined displacement discontinuity method (DDM) and Galerkin's FEM to simulate stress reversal regime around multiple hydraulic fractures in a horizontal well (Kumar et al., 2018).

## **2.6 Summary**

This chapter reviewed the development of conventional hydraulic fracturing, multi-stage hydraulic fracturing, and refracturing. Various approaches of hydraulic fracturing models were compared and analyzed. Production from fracture models using simple and complex fracture geometry were reviewed. Recent refracturing models were also discussed.

The next chapter will introduce lattice simulation for hydraulic fracturing modeling. The lattice based hydraulic fracturing model will be verified with analytical results. Scaling law will be introduced. Modeling of fracturing propagation in viscosity and toughness dominated regimes will be presented.

# Chapter 3

## Lattice Numerical Simulations

This Chapter is modified from the published paper: Wan et al. (2020a).

### 3.1 Introduction

A lattice based hydraulic fracturing simulator XSite was used in this study. The simulator is capable of simulating hydraulic fracturing in single or multiple wells with single or multiple stages. It can simulate fracture propagation from laboratory scale to reservoir scale. Multiple layers with various rock mechanical properties and in-situ stresses can be added to the models. The interaction of hydraulic fractures with arbitrary number and orientation of natural fractures can be simulated. Microseismicity can be predicted by the simulator. Heat exchange between fluids and rocks can also be investigated using the simulator (Damjanac et al., 2011).

The lattice can be considered as quasi-random array of nodes which are connected by springs. A smooth joint model (SJM) has been implemented to represent and model fractures. The lattices are distributed relatively uniformly but in an irregular pattern. The response of a high resolution model is similar to that of a continuum model. The normal and shear stiffness assigned to the spring represent the rock's overall stiffness properties. If the loads on the spring reach the limit, the spring will break and create a joint. The joints can also insert anywhere in the model to simulate model slip on the joint, as shown in Figure 3.1 (Cundall, 2011).

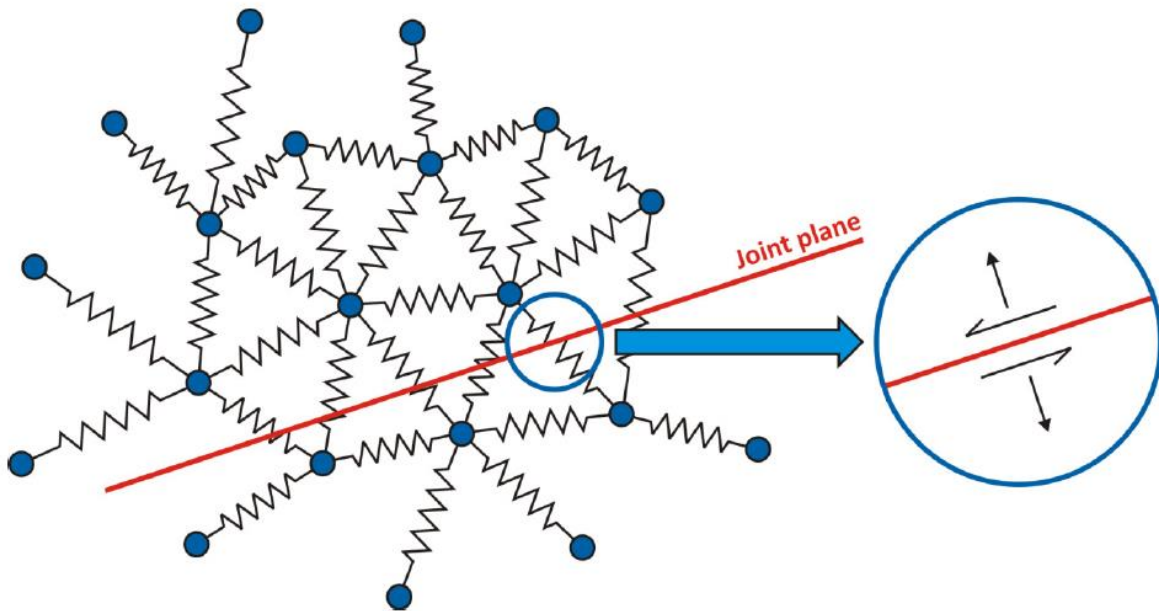


Figure 3.1 Schematic of lattice model showing a joint cuts springs: joint occurs if spring forces reach limit. Blue circle represents lattice nodes (Cundall, 2011).

Fluid flow can be calculated explicitly using the lubrication theory. The pressure change and deformation are updated as time evolve to allow fully coupled fluid flow-mechanical calculation. A mechanical incompressible-flow (MIF) formulation is used in the hydraulic fracturing simulator to allow faster simulation (Damjanac et al., 2011; Damjanac et al., 2016).

## 3.2 Formulation of Lattice Model

### 3.2.1 Lattice and Spring Formulation

The central difference method is the main body of equations that is used to compute the transitional degrees of freedom in the hydraulic fracturing simulator based on:

$$v_i^{t+\Delta t/2} = v_i^{t-\Delta t/2} + \sum F_i^t \Delta t / m \quad (3-1)$$

$$u_i^{t+\Delta t} = u_i^t + v_i^{t+\Delta t/2} \Delta t$$



where  $u_i^t$  and  $v_i^t$  are, respectively, the position and velocity of component  $i$  ( $i = 1, 3$ ) at time  $t$ ,  $\sum F_i^t$  is the sum of all the force-components  $i$  acting on the node of mass  $m$  during the time step  $\Delta t$  (Damjanac et al., 2011).

The angular velocities of component  $\omega_i^t$ , are calculated based on conservation of angular momentum:

$$\omega_i^{t+\Delta t/2} = \omega_i^{t-\Delta t/2} + \frac{\sum \Delta M_i^t}{I} \quad (3-2)$$

where  $\sum \Delta M_i^t$  is the sum of the moment change during time  $t$ ,  $I$  is the moment of inertia. The update of spring force is calculated by:

$$\begin{aligned} F_i^N &\leftarrow F_i^N + \Delta u_i^N k^N \\ F_i^S &\leftarrow F_i^S + \Delta u_i^S k^S \end{aligned} \quad (3-3)$$

where  $F_i^N$  and  $F_i^S$  are the normal and shear spring forces respectively.  $k^N$  and  $k^S$  are the normal and shear spring stiffness respectively.  $\Delta u_i^N$  and  $\Delta u_i^S$  are the normal and shear relative displacement of component  $i$  respectively. If the normal spring force  $F_i^N$  in component  $i$  exceed its spring strength  $F_i^{Nmax}$ , normal and shear spring force,  $F_i^N$  and  $F_i^S$ , will be reset to 0 (Damjanac et al., 2011).

The calculation of fracture propagation in the hydraulic fracturing simulator is by comparing the local stress intensity factor  $K_I$  and fracture toughness  $K_{IC}$ . If fractures are not detected in the region and stress amplification is insignificant, i.e., if  $K_I \ll K_{IC}$ , the spring failure is calculated based on spring tensile strength. Otherwise  $K_I > K_{IC}$  is used as the condition for spring failure and fracture propagation (Damjanac et al., 2011).

### 3.2.2 Fluid Flow Formulation

The hydraulic fracturing simulator allows fluid to flow in both existing joints and joints newly generated by broken springs. The penny-shaped microcracks are represented by fluid nodes which can store pressure. They are connected by pipes to simulate pressure change and fluid flow inside fractures. Based on the existing fluid flow network, new fluid nodes will be automatically generated and connected by pipes when lattice springs are detected to be broken. Lubrication theory is used to estimate flow rate  $q$  from node  $A$  to node  $B$  along a pipe:

$$q = \beta k_r \frac{a^3}{12\mu} [P^A - P^B + \rho_w g(Z^A - Z^B)] \quad (3-4)$$

where  $\beta$  is a calibration parameter used to match network conductivity with local joint conductivity.  $k_r$  is relative permeability.  $a$  is aperture.  $\mu$  is viscosity.  $\rho_w$  is fluid density.  $P^A$  and  $P^B$  are fluid pressure of nodes A and B respectively.  $Z^A$  and  $Z^B$  are elevations of nodes A and B respectively. The update of pressure with time is calculated by:

$$\Delta P = \frac{\sum q_i}{V} K_{fa} \Delta t \quad (3-5)$$

where  $\Delta P$  is pressure increment at time step  $\Delta t$ .  $\sum q_i$  is sum of flow rate from the pipe connecting to the node.  $V$  is volume of the node.  $K_{fa}$  is the apparent fluid bulk modulus (Damjanac et al., 2011).

### 3.2.3 Mechanical Incompressible Flow Formulation

The fluid flow and mechanical coupling is achieved by mechanical incompressible flow (MIF) formulation in the hydraulic fracturing simulator. The MIF formulation uses apparent fluid bulk modulus  $K_{fa}$  to represent the real fluid bulk modulus  $K_f$ .  $K_{fa}$  is proportional to  $K_r a/R$ , where  $K_r$ ,

$a$  and  $R$  are rock bulk modulus, joint aperture and lattice resolution respectively. Typically fluid used for simulation is considered incompressible, i.e.,  $K_f \gg K_r$ , and  $a \ll R$ . Therefore, the  $K_{fa}$  used in the simulation is much smaller than  $K_f$ . Using  $K_{fa}$  in simulation results in greater time step and needs shorter time to complete the simulation compared to the conventional methods which use  $K_f$  for simulation (Damjanac et al., 2011).

### 3.3 Scaling Law

The scaling law refers to the dimensionless numbers that have been proposed to be used for scaling the hydraulic fracturing parameters in a way to replicate similar fracture propagation as occurs in real field. Pierce and Detournay (2008) summarized the scaling laws for penny shape hydraulic fracturing with no lag and proposed four regimes of viscosity dominated without leak-off ( $M$ ), viscosity dominated with leak-off ( $\tilde{M}$ ), toughness dominated without leak-off ( $K$ ), and toughness dominated with leak-off ( $\tilde{K}$ ). If leak-off is neglected, a dimensionless toughness parameter ( $\kappa$ ) is introduced to identify toughness dominated and viscosity dominated regimes as shown in equation (1):

$$\kappa = K' \left( \frac{t^2}{\mu'^5 Q_0^3 E'^{13}} \right)^{\frac{1}{18}} \quad (1)$$

where

$$K' = 4 \sqrt{\frac{2}{\pi}} K_{IC}$$

$$\mu' = 12\mu$$

$$E' = \frac{E}{1 - \nu^2}$$
(2)

and  $t$  is injection time,  $Q_0$  is injection rate,  $\mu$  is fluid viscosity,  $K_{IC}$  is fracture toughness,  $E$  is Young's modulus, and  $\nu$  is Poisson's ratio (Savitski and Detournay, 2002). All parameters in equation (1) and (2) are in SI units.

Toughness dominated regime corresponds to  $\kappa > 3.5$ , viscosity dominated regime corresponds to  $\kappa < 1$  (Savitski and Detournay, 2002).

### 3.4 Model Verification

#### 3.4.1 Toughness Verification

In order to increase the accuracy of the macroscopic properties in modelling, setting correct lattice resolution in the hydraulic fracturing simulator is very important. The resolution may affect the toughness properties of the rock, whereas the stiffness and strength properties of the lattice springs are calculated automatically to match macroscopic mechanical properties (Damjanac et al., 2016).

The toughness tests were conducted using samples with geometry shown in Figure 3.2. A rectangular through crack with half-length of  $a$  was placed at the center of a finite plate with length  $L$ , width  $W$ , and a small thickness  $h$ . The size of the plate and crack for the sample were selected

based on lattice resolution ( $R$ ) and the number of nodes per fracture length. The number of nodes per fracture length ( $N$ ) can be calculated using equation (3).

$$N = \frac{a}{R} \quad (3)$$

A constant and small loading velocity of 0.001 m/s was applied to the upper boundary of the sample. The calibration force was increased until the sample failed. The calibration force when sample failed was recorded to calculate the yield stress ( $\sigma_Y$ ) and the mode I fracture toughness ( $K_{IC}$ ) of the sample.

Five groups of toughness tests were conducted using lattice resolution ( $R$ ) of 1  $m$  to 5  $m$  with increment of 1  $m$ . Each group was tested for different model sizes with number of nodes per fracture length ( $N$ ) changing from 20 to 40. Both length ( $L$ ) and width ( $W$ ) of the plate changed from 80  $R$  to 160  $R$ . The thickness of the plate ( $h$ ) was 2  $R$  for each group. The specified tensile strength ( $\sigma_{T0}$ ) and the setting mode I toughness ( $K_{IC0}$ ) values in all tests were 5  $MPa$  and 1  $MPa\sqrt{m}$ , respectively. The apparent toughness ( $K_{IC}'$ ) for different samples were calculated using equation (4) (Anderson, 2005). The values of input parameters and testing results are shown in Table 3.1 and plotted in Figure 3.2.

$$K_{IC}' = \sigma_Y \sqrt{\pi a} \left[ \sec \left( \frac{\pi a}{L} \right) \right]^{1/2} \left[ 1 - 0.025 \left( \frac{2a}{L} \right)^2 + 0.06 \left( \frac{2a}{L} \right)^4 \right] \quad (4)$$

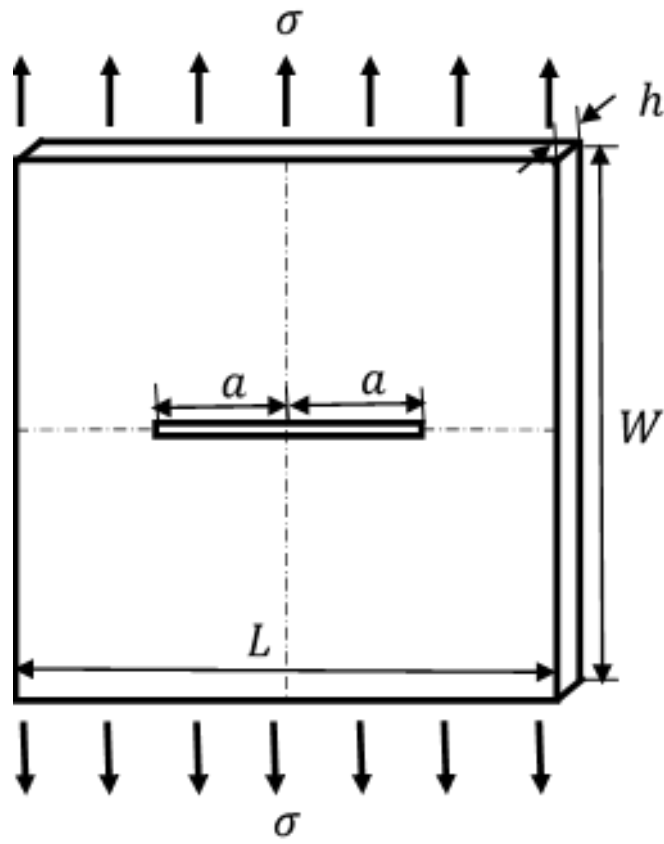


Figure 3.2 Sample geometry for toughness test

Table 3.1 Model input parameters and results of toughness tests for five different sample resolutions

$R, m$	$L, m$	$W, m$	$a, m$	$h, m$	$A, m^2$	$V, m^3$	$N$	$\sigma_y, MPa$	$K_{IC}', MPa\sqrt{m}$	$\delta K_{IC}$
	80	80	20	2	160	1.28E+04	20	0.085	0.799	20.08%
	100	100	25	2	200	2.00E+04	25	0.088	0.920	8.01%
1	120	120	30	2	240	2.88E+04	30	0.079	0.912	8.83%
	140	140	35	2	280	3.92E+04	35	0.085	1.062	-6.17%
	160	160	40	2	320	5.12E+04	40	0.071	0.947	5.25%
	160	160	40	4	640	1.02E+05	20	0.064	0.852	14.81%
	200	200	50	4	800	1.60E+05	25	0.071	1.059	-5.93%
2	240	240	60	4	960	2.30E+05	30	0.059	0.967	3.30%
	280	280	70	4	1,120	3.14E+05	35	0.057	0.997	0.26%
	320	320	80	4	1,280	4.10E+05	40	0.051	0.955	4.50%
	240	240	60	6	1,440	3.46E+05	20	0.051	0.837	16.31%
	300	300	75	6	1,800	5.40E+05	25	0.054	0.991	0.86%
3	360	360	90	6	2,160	7.78E+05	30	0.050	1.007	-0.66%
	420	420	105	6	2,520	1.06E+06	35	0.051	1.103	-10.29%
	480	480	120	6	2,880	1.38E+06	40	0.043	0.992	0.83%
	320	320	80	8	2,560	8.19E+05	20	0.048	0.896	10.38%
	400	400	100	8	3,200	1.28E+06	25	0.049	1.032	-3.16%
4	480	480	120	8	3,840	1.84E+06	30	0.042	0.972	2.83%
	560	560	140	8	4,480	2.51E+06	35	0.042	1.044	-4.40%
	640	640	160	8	5,120	3.28E+06	40	0.038	1.013	-1.29%

	400	400	100	10	4,000	1.60E+06	20	0.041	0.857	14.32%
	500	500	125	10	5,000	2.50E+06	25	0.042	0.992	0.80%
5	600	600	150	10	6,000	3.60E+06	30	0.041	1.047	-4.72%
	700	700	175	10	7,000	4.90E+06	35	0.039	1.081	-8.08%
	800	800	200	10	8,000	6.40E+06	40	0.035	1.033	-3.33%

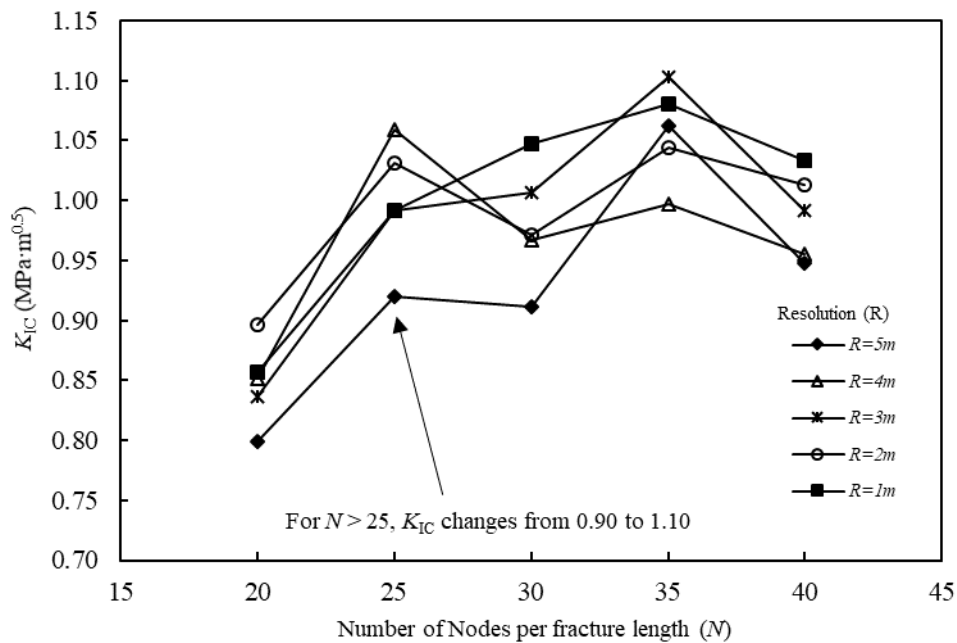


Figure 3.3 Apparent toughness  $K_{IC}'$  for different lattice resolutions and number of nodes per fracture length

As shown in Figure 3.3, for all the five different lattice resolutions, if the number of nodes per fracture length is equal to or greater than 25,  $K_{IC}'$  ranges from 0.9 to 1.1 MPa $\sqrt{m}$  and the absolute error in toughness estimation will be less than 10%. Thus, the code generally matches the target fracture toughness. The increase in the error in approximation of the fracture toughness with



reduction in the number of resolution is a consequence of transition from conditions that can be approximated by linear elastic fracture mechanics (and  $K_{IC}$ ), for large number of resolutions per fracture length, to the condition when size effect does not exist and failure is approximated by plasticity, for few resolutions per fracture length.

### 3.4.2 Viscosity dominated regime verification

Rasouli and Sutherland (2014) conducted laboratory experiments to model the fracture propagated in the viscosity dominated regime that is likely observed in real field. The experimental data were upscaled according to the scaling law to verify the analytical solution ( $M$  solution) for viscosity dominated regime with no leak-off (Savitski and Detournay, 2002; Peirce and Detournay, 2008). Leak-off was neglected in this study. Damjanac et al. (2016) suggest using zero in-stresses so that the numerical test condition corresponds to that of the  $M$ -asymptotic solution defined by Peirce and Detournay (Damjanac et al., 2016; Peirce and Detournay, 2008).

To allow penny shaped fracture propagation, in-situ stresses with small anisotropy were used in this study for verification test shown in Figure 3.4. The initial vertical stress ( $\sigma_v$ ), max horizontal stress ( $\sigma_H$ ), and minimum horizontal stress ( $\sigma_h$ ) are  $2.2 \text{ MPa}$ ,  $2.1 \text{ MPa}$ , and  $2 \text{ MPa}$ , respectively. A cased vertical well with no thickness is located at the center of a cuboid rock with dimensions  $L = 14 \text{ m}$ ,  $W = 12 \text{ m}$ ,  $H = 14 \text{ m}$ . The Young's modulus, Poisson's ratio, and Toughness of the rock model are  $30 \text{ GPa}$ ,  $0.3$ , and  $1 \text{ MPa}\cdot\text{m}^{0.5}$  respectively. A small initial crack with a radius of  $0.6 \text{ m}$ , aperture of  $10^{-5} \text{ m}$ , and stiffness of  $0$  is placed at the center of the rock parallel to the  $XZ$  plane. The small crack, which is perpendicular to the wellbore, ensures initiation of hydraulic fracture perpendicular to the minimum principal stress, which in this example is  $\sigma_h$ . During the verification test, fluid is injected into the initial crack via a cluster with a radius of  $0.4 \text{ m}$ . The

injection rate is  $Q_0 = 0.005m^3/s$  and the injection fluid viscosity is  $\mu = 0.01 Pa \cdot s$ . The selection of these injection rate and injection fluid viscosity ensures fracture to propagate faster and grow into relatively planar geometry. From equation (1) it can be found that  $\kappa = 0.45 < 1$  when injection time  $t = 10 s$ , indicating that the fracture is propagating in the viscosity dominated regime when  $t \leq 10 s$ . The verification tests started with only mechanical mode being active for 0.01 second. Then three verification tests with fluid-mechanical coupled mode being active were conducted for 1 second, 2 second, and 3 second, respectively.

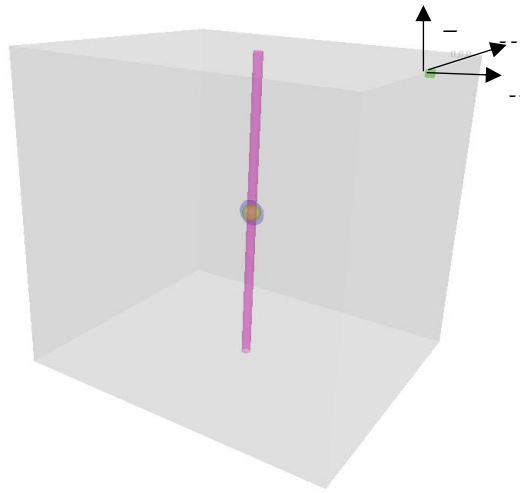


Figure 3.4 Toughness and viscosity dominated regime verification tests sample geometry

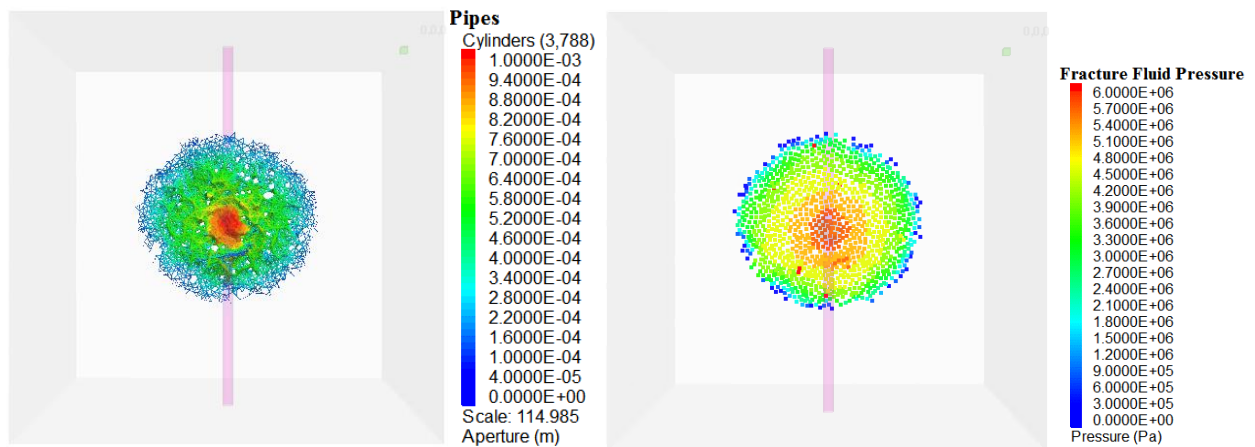
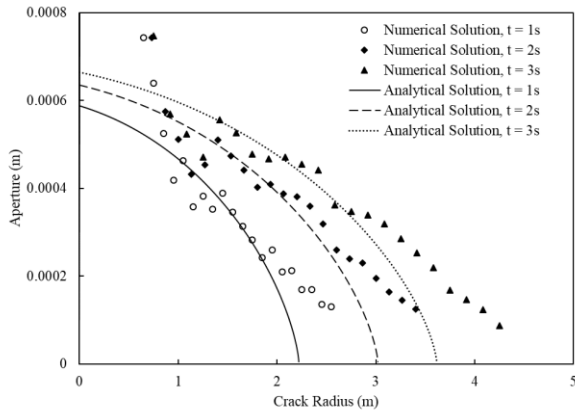


Figure 3.5 Front view of viscosity dominated regime verification test at 3 s. Aperture (left) and fracture pressure (right) distribution

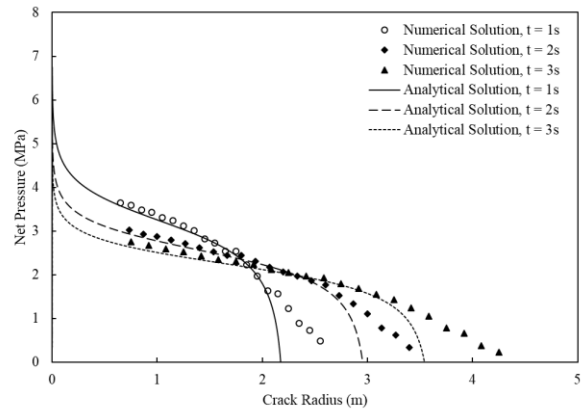
Figure 3.5 shows that after 3 second of fluid injection, the geometry of the hydraulic fracture is almost penny shape. Average numerical results of apertures and pressures (for 30 radius) were compared with asymptotic solutions and the results are shown in Figure 3.6 (a) and (b). Note that the numerical fracture fluid pressure, as shown in Figure 3.5 (right), was subtracted by the minimum horizontal stress ( $\sigma_h$ ) of 2 MPa to obtain the numerical net pressure shown in Figure 3.6 (b). The initial crack led to inappropriate estimation of fracture aperture and pressure within the initial crack radius, thus numerical results with radius less than 0.6 m were deleted. The numerical results show acceptable match with the analytical solutions despite greater deviations occur near the wellbore and the fracture tip, as shown in Figure 3.6 (a) and (b). The deviations near the wellbore are likely to be caused by injection into a cluster with finite radius, which is different from a point source. Near the fracture tip, the finite aperture of the initial fracture of the numerical simulation allows seepage ahead of the fracture tip, leading to deviations (Savitski and Detournay, 2002; Peirce and Detournay, 2008; Damjanac et al., 2016; Xing et al., 2018).

The comparison of dimensionless numerical results against dimensionless analytical results for viscosity dominated regime verification tests are presented in Figure 3.6 (c) and (d). The numerical data with dimensionless crack radius less than 0.9 were used to fit with analytical solutions and calculate coefficient of determination ( $R^2$ ). The calculated  $R^2$  for dimensionless aperture and dimensionless net pressure are 0.71 and 0.96 respectively. The results suggest the numerical data show reasonable match with analytical solution if data near wellbore and fracture tip were excluded. Analytical solutions for viscosity dominated regime dimensionless aperture and net pressure

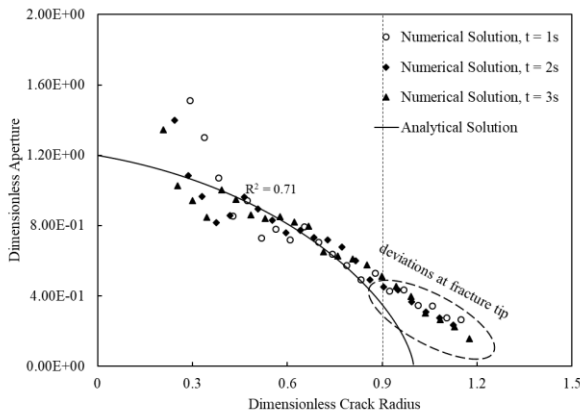
calculations are presented in the literatures (Savitski and Detournay, 2002; Peirce and Detournay, 2008).



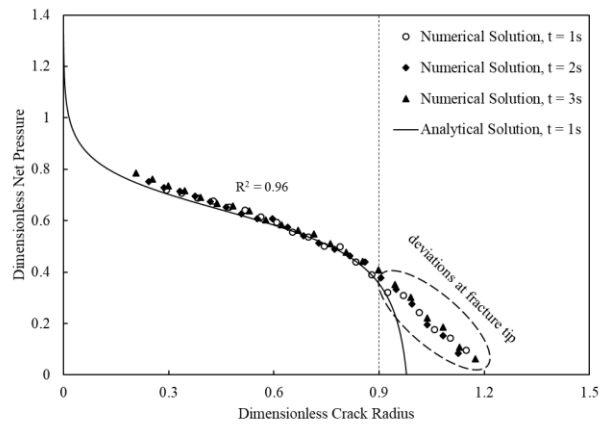
(a)



(b)



(c)



(d)

Figure 3.6 Comparison of numerical results from viscosity dominated regime verification tests with analytical solutions at three times: (a) aperture profiles, (b) pressure profiles, (c) dimensionless aperture profiles, (d) dimensionless pressure profiles

### 3.4.3 Toughness dominated regime verification

To verify toughness dominated fracture propagation in the hydraulic fracture simulator with the analytical solution, the model toughness  $K_{IC}$  was from  $1 \text{ MPa}\cdot\text{m}^{0.5}$  to  $10 \text{ MPa}\cdot\text{m}^{0.5}$ . Recorded injection times were modified to 2.5 s, 5 s, and 7.5 s. Other parameters were kept the same. In this model the dimensionless toughness  $\kappa$  becomes 3.52 when injection time  $t$  is 1 s. Since  $\kappa$  is proportional to  $t^{1/9}$  as equation () suggested, the fracture propagation is in the toughness dominated regime if  $t > 1 \text{ second}$

The aperture and pressure distribution results of the toughness dominated regime verification model are shown in Figure 3.7. The results suggest the fracture geometry deviates from the penny shape and becomes asymmetrical. The asymmetry of the fracture is caused by relatively uniform distribution of fracture pressure as shown in Figure 3.7 (right). When pressure is uniformly distributed, the fracture could not determine where the injection point is, thus it propagates to random direction.

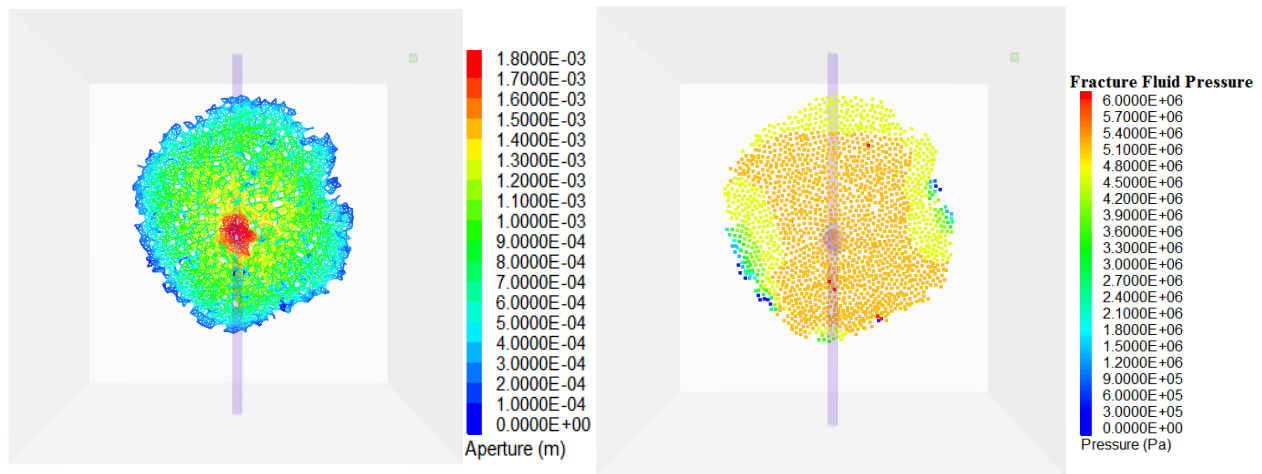
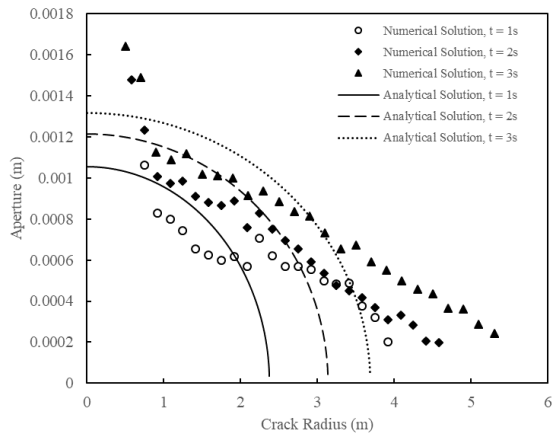
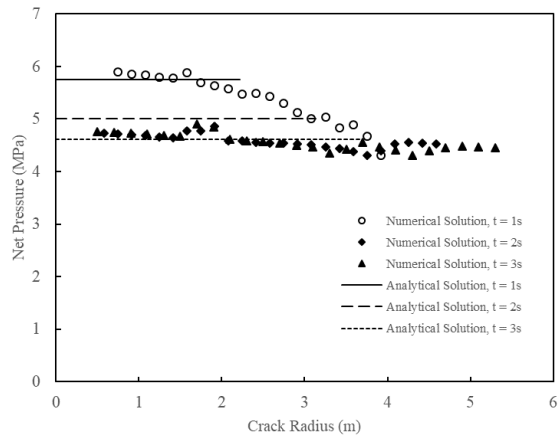


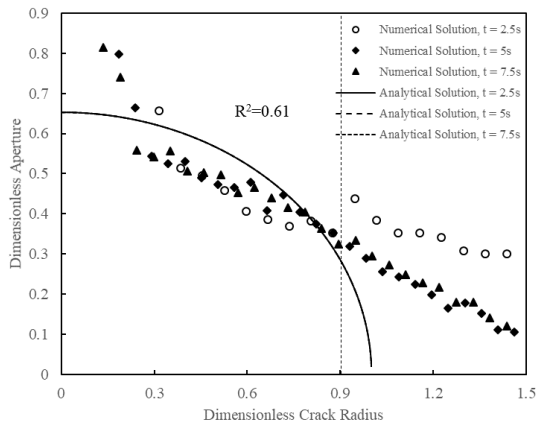
Figure 3.7 Front view of toughness dominated regime verification Test at 7.5 s. Aperture (left) and fracture pressure (right) distribution



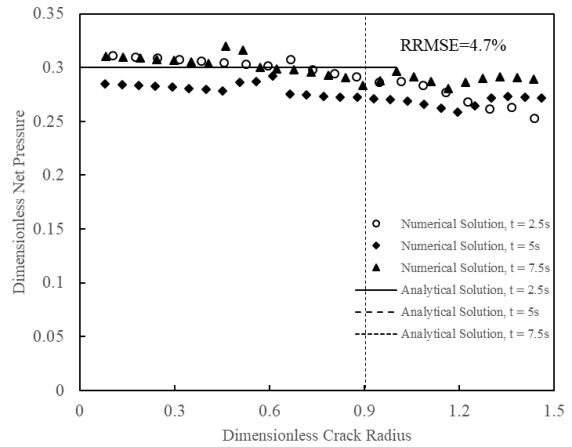
(a)



(b)



(c)



(d)

Figure 3.8 Comparison of numerical results from toughness dominated regime verification tests with analytical solutions at three times: (a) aperture profiles, (b) pressure profiles, (c) dimensionless aperture profiles, (d) dimensionless pressure profiles

For toughness dominated regime verification, the numerical and analytical dimensionless results comparison is presented in Figure 3.8 (c) and (d). Dimensionless crack radius less than 0.9 were used to fit numerical models with analytical solutions. The calculated  $R^2$  for dimensionless aperture is 0.61. The result shows reasonable aperture match for toughness dominated verification

tests, but it is not as good as that of the viscosity dominated verification tests. This is because the simulated fracture geometry deviates from penny shape and the aperture gradient varies in different directions. The results suggest the numerical data show reasonable match with analytical solution if data near wellbore and fracture tip were excluded. The toughness dominated analytical solutions, the dimensionless net pressure is independent of the dimensionless crack radius, as shown in Figure 3.8 (d), thus  $R^2$  is not appropriate for evaluate the accuracy of the numerical model, relative root mean square error (RRMSE) is used to calculate instead. The calculated value for RRMSE of the toughness dominated regime dimensionless pressure is 4.7%, implying good match for dimensionless pressure with dimensionless radius less than 0.9. (Savitski and Detournay, 2002; Peirce and Detournay, 2008). Toughness dominated regime analytical solutions for dimensionless aperture and net pressure are presented in the literatures (Savitski and Detournay, 2002; Peirce and Detournay, 2008).

### **3.5 Summary**

This chapter presented formulation of the lattice based hydraulic fracturing simulators. Scaling law was introduced for hydraulic fracturing simulation in various scales. Lattice based hydraulic fracturing models were verified by toughness verification tests. The results show that apparent toughness has smaller error if number of nodes per fracture length is larger than 25 for different lattice resolutions. Verification tests with consideration of scaling law showed a good agreement with the asymptotic solutions for viscosity dominated regime and toughness dominated regime.

The next chapter will perform hydraulic fracturing simulation for fracture containment analysis using the hydraulic fracturing simulator. Intermediate scale and field scale models will be

presented and compared with observations in laboratory experiment and analytical results.  
Penetration parameters will be introduced to quantify fracture containment.



# Chapter 4

## Hydraulic Fracturing Simulation

This Chapter is modified from the published paper: Wan et al. (2020a).

### 4.1 Introduction

In this chapter, the lattice based hydraulic fracturing simulator was used for modeling hydraulic fracture propagation and analyzing the effects of changing rock properties and in-situ stresses on hydraulic fracture propagation and its containment. The study was done based on the data from one of the shale gas wells in the North Perth Basin (NPB) located at the southwest part of Australia and the hydraulic fracturing lab experimental data on a 50 mm cubical sample. The hydraulic fracturing initiates and propagates within Carynginia Formation surrounded by the Irwin River Coal Measures (IRCM) Formation from the top and Kockatea Formation at the base. The lab experiments were upscaled to both intermediate and field scales to simulate fracture propagation in the viscosity dominated regime. Penetration parameters, including the depth and area of the fracture crossing the interface, were proposed to characterize fracture containment capacity in Kockatea and IRCM Formations. The impacts of rock brittleness and minimum horizontal stress contrast on fracture containment were discussed.

## 4.2 Model Set Up

Rasouli and Sutherland (2014) built a rock mechanical model (RMM) to estimate rock properties and in-situ stresses within the reservoir (Carynginia Formation) and over/under burden rocks. Figure 4.1 shows the RMM output including the continuous profiles of rock elastic and strength properties as well as in-situ stresses. Also, in this figure the formations below and above the reservoir formation are shown. Also, laboratory experiments corresponding to the hydraulic fracturing operation in well Arrowsmith 1, in the NPB were done on 50 mm cubical sample taken from the target zone (Rasouli and Sutherland, 2014). The Carynginia Formation is the targeted shale gas formation in the NPB consisting of shale and siltstone with lesser amounts of interbedded sandstone and conglomerate (Morey et al., 2005). Thin layers of Wagina Sandstone and Beekeeper Formations lie above the Carynginia Formation and underlie Kockatea Shale Formation which consists of clayey siltstone with some ferruginous layer (Morey et al., 2005).. The Carynginia Formation is underlain by the Irwin River Coal Measures (IRCM) Formation, which consists of mixed layers of sandstone, siltstone, carbonaceous shale and coal (Morey et al., 2005).

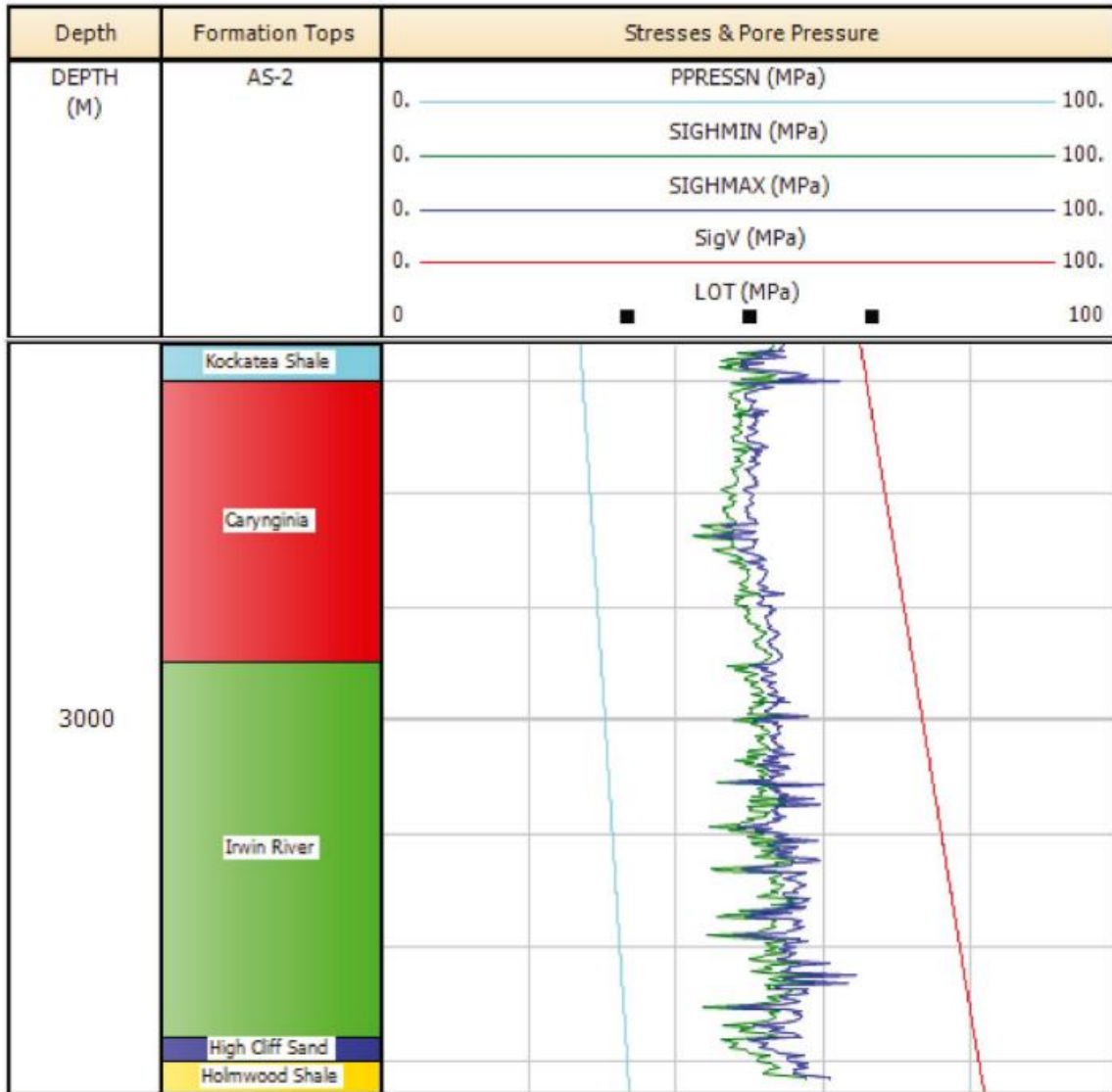


Figure 4.1 Rock mechanical model (RMM) and rock elastic properties for a well in NPB (Rasouli and Sutherland, 2014)

In the simulation, hydraulic fractures were considered to be initiated at the center of the Carynginia Shale Formation. Thin layers of Wagina Sandstone and Beekeeper Formations were neglected. The effects of rock properties of upper Kockatea Shale Formation and lower IRCM Formation, and the effects of in-situ stresses in three different layers on hydraulic fracture propagation were analyzed. Average values of rock properties (except fracture toughness  $K_{IC}$ ) for three different

layers were estimated from the RMM model (Rasouli and Sutherland, 2014) and listed in Table 4.1.  $K_{IC}$  was assumed to be  $1 \text{ MPa} \cdot \sqrt{m}$  for all the layers.  $BI$  is the brittleness index proposed by Luan (2014) using:

$$BI = \frac{E}{\nu} \quad (5)$$

Numerous brittleness indices (BIs) have been proposed by different researchers based on rock elastic properties and strength, stress-strain response, grain size, mineralogy, and energy criteria for fracture propagation (Hucka and Das, 1974; Rickman et al., 2008; Luan et al., 2014; Jin et al., 2015; Zhang et al., 2016; Feng et al., 2020). The BIs defined by different researchers were applied to characterize various rock performance in different applications.

For application of hydraulic fracturing applications, stiffness properties including Young's modulus and Poisson's ratio are two most important parameters measured to characterize rock brittleness (Grieser and Bray, 2007; Luan et al., 2014; Wang et al., 2015; Gholami et al., 2016; Zhang et al., 2016). According to Luan et al. (2014), using ratio of Young's modulus over Poisson's ratio can reasonably quantify brittleness for field application. Therefore, equation (5) was used in this work to quantify formation brittleness.

Table 4.1 Rock properties used for simulations

Formation	$E, GPa$	$\nu$	$BI, GPa$	$\phi$	$UCS, MPa$	$\sigma_t, MPa$	$K_{IC}, MPa \cdot \sqrt{m}$
Kockatea	18	0.4	45	22	30	3	1
Carynginia	30	0.3	100	25	40	4	1

---

IRCM	45	0.2	225	40	55	5.5	1
------	----	-----	-----	----	----	-----	---

---

### 4.3 Intermediate Scale Simulations

Rasouli and Sutherland (2014) used a 50 *mm* cubical sample to conduct a laboratory hydraulic fracturing experiment under true triaxial stress conditions. The experiment results are shown in Figure 4.1. The vertical and two horizontal stresses applied in their experiment were 66 MPa, 52 MPa, and 54 MPa, respectively. To allow hydraulic fracture propagating in the viscosity dominated regime, they used maximum available pumping rate of 0.02 *cc/min* and fluid viscosity of 100,000 *cp* (Rasouli and Sutherland, 2014). The very low flow rate and high viscosity of the fluid used in the lab is to ensure that the fracture can propagate very slowly for a few seconds and allow recording the pressure data before fluid reaches the ends of the sample. However, for hydraulic fracturing operations in the field, viscosity of fracturing fluids is much smaller, and the injection rate is much larger. Also, the typical length and height of hydraulic fracture in real field is in the range of 10 to 1,000 *m*.

Four simulation cases are presented here, which start from a simple one-layer model to three-layer models with the same rock properties in three layers (in-situ stresses change), same in-situ stresses in three layers (rock properties change) and both rock properties and in-situ stresses changing in the three layers. The latter case corresponds to the real field case study. Description and input summary for intermediate scale and field scale simulations are presented in Table 4.2. However, the results of the first three case studies help to understand the extent of the impact of rock properties and in-situ stresses on fracture containment due to layering, separately.

Table 4.2 Description and input summary for all cases

Case	Method	Formation	Thickness, m	$S_v$ , MPa	$S_H$ , Mpa	$S_h$ , MPa	$Q_0$ , m <sup>3</sup> /s	$\mu$ , Pa·s	$t$ , s
0	Analytical	Carynginia	14	\	\	\	0.005	0.01	8
1	Numerical	Carynginia	14	15	3	1	0.005	0.01	8
		Kockatea	3	15	3	1			
2	Numerical	Carynginia	8	15	3	1	0.005	0.01	8
		IRCM	3	15	3	1			
		Carynginia	3	15	5	3			
3	Numerical	Carynginia	8	15	3	1	0.005	0.01	8
		Carynginia	3	15	5	3			
		Kockatea	3	15	5	3			
4	Numerical	Carynginia	8	15	3	1	0.005	0.01	8
		IRCM	3	15	5	3			
		Kockatea	50	15	5	3			
5	Numerical	Carynginia	250	15	3	1	0.005	0.24	2000
		IRCM	50	15	5	3			
6	Analytical	Carynginia	350	\	\	\	0.005	0.24	2000

In the following four case studies, the sample dimension for the laboratory experiment (Rasouli and Sutherland, 2014) was upscaled to  $14\text{ m} \times 12\text{ m} \times 14\text{ m}$  (length ( $L$ )  $\times$  width ( $W$ )  $\times$  height ( $H$ )). It's more appropriate to upscale the laboratory sample to the field scale. However, field scale simulation generally requires longer simulation time and higher computation effort. For computational efficiency, intermediate scale was utilized. However, the scaling laws ensured that the fracture propagation remains in the same regime as of those field and lab scale testing. This approach was found to be appropriate for the purpose of studying the fracture containment, which is the main objective of this study.

A new approach was proposed to characterize fracture containment using penetration parameters.  $A_{1i}$  and  $A_{2i}$  ( $i = 0,1,2,3,4$ ) are the penetration areas.  $D_{1i}$  and  $D_{2i}$  ( $i = 0,1,2,3,4$ ) are the fracture penetration depths above  $Z = -3 \text{ m}$  and below  $Z = -11 \text{ m}$ , respectively. Subscript  $i$  is the case number, and  $i = 0$  represents case of the analytical solution to be compared with Case 1. Note that penetration depths are the same in the front and side view of the fracture geometry for all cases. These parameters are marked in the following figures of fracture outline and listed in Table 4.3. They are used to characterize the capacity of fracture containment.

Table 4.3 Penetration areas and depths for intermediate scale simulations

Case No. $i$	$A_{1i}, \text{m}^2$	$A_{2i}, \text{m}^2$	$D_{1i}, \text{m}$	$D_{2i}, \text{m}$
0	5.98	5.98	1.27	1.27
1	5.40	4.02	1.26	0.98
2	4.34	5.61	1.03	1.32
3	2.40	2.71	0.59	0.64
4	1.91	3.01	0.50	0.78

The resolution of the main lattice was set to be  $0.5 \text{ m}$ . Sub-lattice of  $0.25 \text{ m}$  was applied to ensure more accurate calculation for fracture propagation. The application of sub-lattice allowed the software to calculate pressure and velocity using main lattice while solve fracture propagation using the sub-lattice, thus reducing computational effort. Stress boundary conditions were applied on the sides of the model. In each case, a cased wellbore with no thickness was placed at the center of the rock sample. Fracturing fluid with viscosity of  $10 \text{ cp}$  ( $0.01 \text{ Pa} \cdot \text{s}$ ) was injected via a cluster with radius of  $0.3 \text{ m}$  and an initial crack with radius of  $0.5 \text{ m}$  and aperture of  $0.00001 \text{ m}$  in  $XZ$  plane. The injection rate was  $0.005 \text{ m}^3/\text{s}$ . Using these input values, from equation (1) it is seen

that  $\kappa = 0.73 < 1$  when injection time  $t \leq 10$  s, i.e. the fracture propagation will be viscosity dominated if injection time is no greater than 10 s, similar to the real field conditions. The general model for all cases studied is shown in Figure 4.3. In each case, simulation started with 0.05 second at mechanical active mode to allow the model reaching equilibrium, and continued running 4 second at coupled fluid-mechanical active mode.

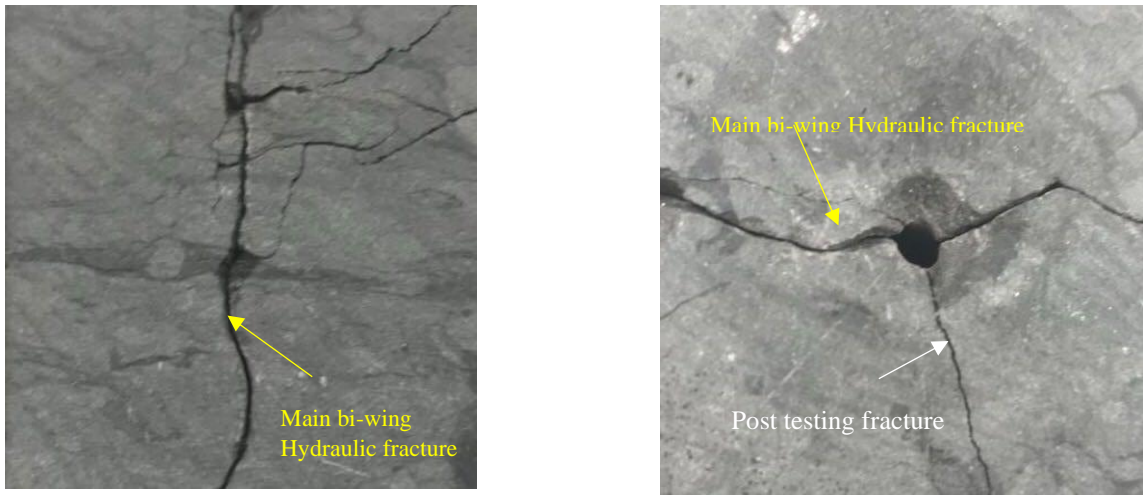


Figure 4.2 Side (left) and top (right) views of the sample after the hydraulic fracturing experiment (Rasouli and Sutherland, 2014)

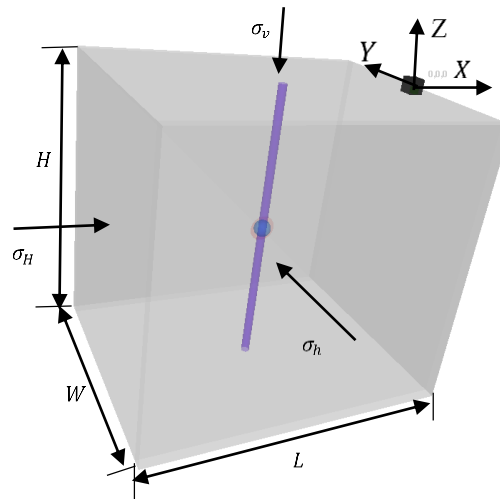


Figure 4.3 General model geometry used for simulations



### 4.3.1 Case 1: One-layer model

This case simulates fracture propagation under simple reservoir conditions. The formation was assumed to be homogeneous and isotropic having similar properties as the reservoir, i.e. Carynginia Formation. Three principal stresses were scaled down to  $\sigma_v = 15 \text{ MPa}$ ,  $\sigma_H = 3 \text{ MPa}$ , and  $\sigma_h = 1 \text{ MPa}$ , and applied to the model. The stress anisotropies between three principal stresses were kept the same, while downscaling contributed to less computational effort. Simulation results corresponding to Case 1 are shown in Figure 4.4 and Figure 4.5.

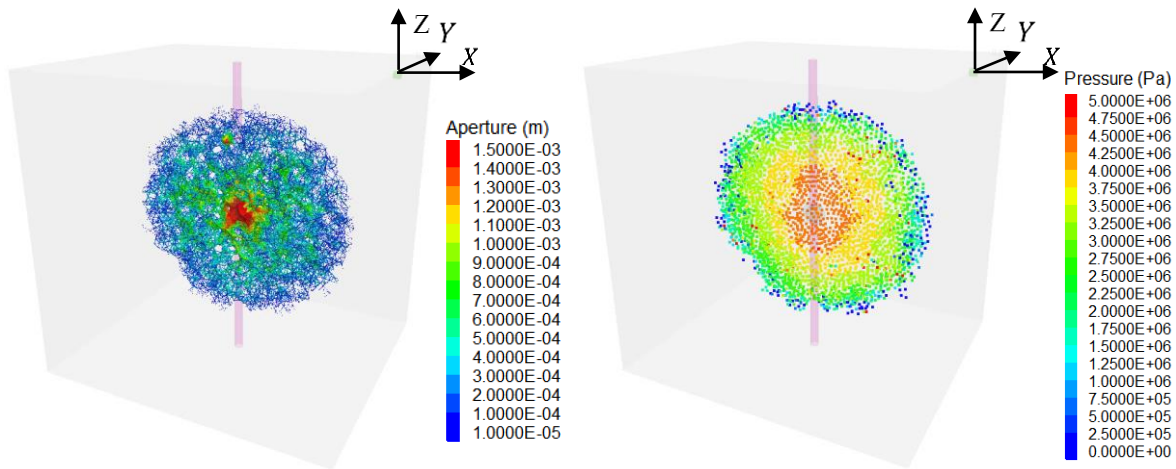


Figure 4.4 Case 1: one-layer model. Aperture (left) and fracture pressure (right) distribution

Figure 4.4 shows that the induced hydraulic fracture is almost penny shaped with the larger aperture and pressure near the wellbore, reducing as approaches the tip. The result indicated viscosity dominated fracture propagation. Front view, left side view, and top view of hydraulic fracture contours and their geometry outlines as depicted in Figure 4.5 indicate that the fracture is almost located at the center of the  $Y = 0$  plane and almost propagated perpendicular to the minimum horizontal stress direction. Note that the fracture outlines shown in Figure 4.5 describe the outer boundaries of all the cracks. Figure 4.5 (e) and (f) indicate that the simulated hydraulic

fracture contains multiple braches of micro cracks close to the main fracture plane. The orientations of these micro cracks deviate from the main fracture plane due to injection-induced stresses.

Figure 4.5 Aperture contours after 7 second for Case 1: (a) front view; (b) left side view; (c) top view; (d) front view outline; (e) left side view outline; (f) top view outline

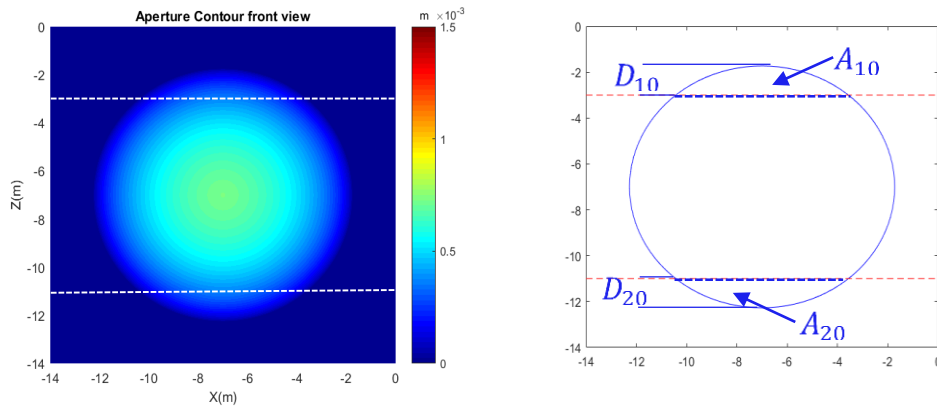


Figure 4.6 Viscosity dominated regime asymptotic solution for aperture contour (left) and outline (right) after 7 second

Figure 4.5 (b) and (c) of the Case 1 simulation results can be compared with Figure 4.2 (left) and (right) of the laboratory experiment results. Both show that the primary fracture planes are perpendicular to the minimum horizontal stress, however, in both cases we observe a tortuous and rough geometry for the propagating fracture planes due to the low stress anisotropy (i.e. difference between maximum and minimum horizontal stresses). At large stress anisotropy condition, the fracture geometry will be more planar and perpendicular to the minimum horizontal stress. In contrast, when stress anisotropy is low, the rock structure and grain properties will play a more important role in fracture initiation and propagation, thus the fracture plane will be more rough and tortuous and we may observe multiple branches of fractures developing around the wellbore.

In simulation, the non-planar fracture geometry is likely to occur due to both small stress anisotropy and the random distribution of lattice properties.

The Case 1 simulation results shown in Figure 4.5 (a) to (d) can also be compared with the analytical results of Figure 4.6. The analytical results show similar aperture distribution with that of the simulation results. It is to note that the large aperture magnitudes at the center of the numerical model belong to the wellbore area and should be discarded. This is because the wellbore area is a finite volume, rather than a point source, which is assumed in the analytical solution. The numerical fracture outline in Figure 4.5 (d) has similar shape and area with those of the analytical fracture outline in Figure 4.6 (right), while the numerical fracture outline is not a perfect circle. The penetration parameters ( $A_{11}$ ,  $A_{21}$ ,  $D_{11}$ , and  $D_{21}$ ) obtained from numerical models are less than analytical results ( $A_{10}$ ,  $A_{20}$ ,  $D_{10}$ , and  $D_{20}$ ) as tabulated in Table 4.3, indicating that the hydraulic fracture in this case elongates more in the horizontal direction, thus the fracture geometry deviates from the circular shape. The relatively elliptical shape of the numerical fracture outline is likely to be the result of random distribution of lattice properties.

#### **4.3.2 Case 2: Three-layer model, different rock properties**

This case investigates the effect of different rock properties on propagation of hydraulic fracture. The model was divided into three layers from top to bottom corresponding to the properties of the Kockatea, Carynginia, and IRCM Formations, respectively, as shown in Table 4.1. The upper, middle, and lower layers thickness are 3 m, 8 m, and 3 m, respectively. The in-situ stresses applied to the all the three layers were the same as Case 1. The simulation results are presented in Figure 4.7 and Figure 4.8.

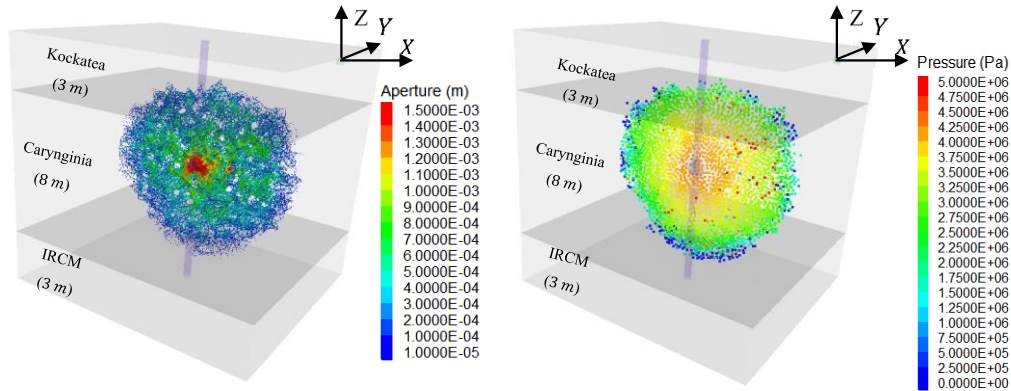


Figure 4.7 Case 2: Three-layer model, different rock properties. Aperture (left) and fracture pressure (right) distribution

Figure 4.7 and Figure 4.8 (a) and (d) show that the induced hydraulic fracture deviates from penny shaped geometry due to being interfered by different rock properties of the three layers. The hydraulic fracture penetrates into both IRCM and Kockatea Formations, as shown in Figure 4.8 (d) and (e). However, Table 4.3 shows that  $A_{12}$  and  $D_{12}$  for Case 2 are less than  $A_{11}$  and  $D_{11}$  for Case 1, respectively, suggesting that the Kockatea Formation inhibits fracture propagation. In contrast,  $A_{22}$  and  $D_{22}$  for Case 2 are larger than  $A_{21}$  and  $D_{21}$  for Case 1, respectively, suggesting that IRCM Formation favors fracture propagation. These results agree with the effect of brittleness on hydraulic fracture propagation (Hucka and Das, 1974; Wang H., 2015; Gholami et al., 2016).

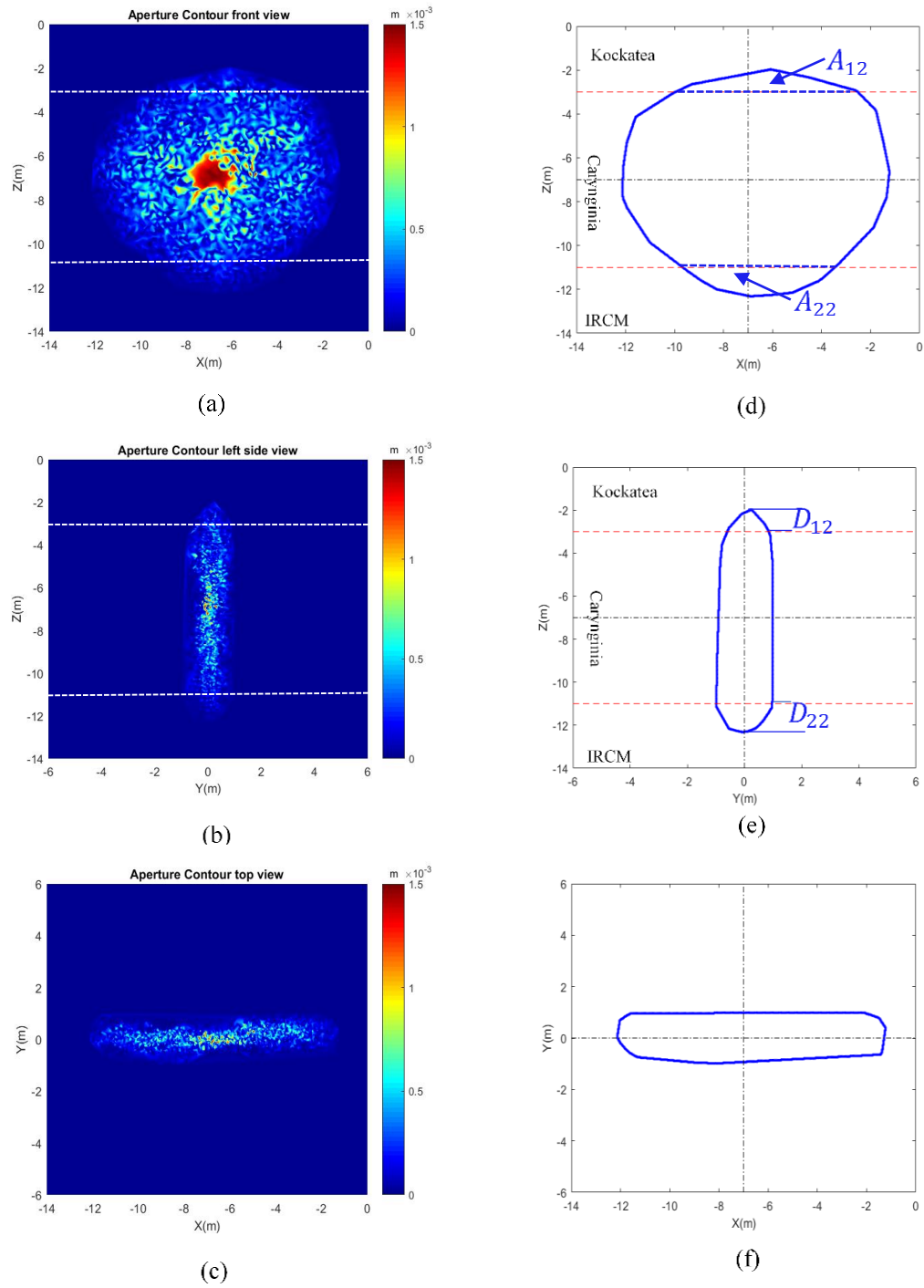


Figure 4.8 Aperture contours after 8 second for case 2: (a) front view; (b) left side view; (c) top view; (d) front view outline; (e) left side view outline; (f) top view outline

The Kockatea Formation is a shale formation with the smallest brittleness index among the three layers, as is seen from Table 4.1. Therefore, Kockatea Formation tends to inhibit vertical migration of hydraulic fracture. In contrast, IRCM Formation has the largest brittleness index among the three layers, hence the highest brittleness (see Table 4.1), which favors vertical propagation of hydraulic fracture. These results can be further verified by comparing Figure 4.8 and Figure 4.5. The aperture and pressure distribution still shows higher magnitude near the wellbore and lower magnitude near the fracture tip as is shown in Figure 4.7. The result verify the fracture propagates in the viscosity dominated regime, despite changing of rock properties. All the fracture contour plots and their geometry outlines shown in Figure 4.8 indicate that the hydraulic fracture is still almost placed at the  $Y = 0$  plane and is almost perpendicular to the minimum horizontal stress direction.

#### **4.3.3 Case 3: Three-layer model, different stresses**

In order to study the effect of stress contrast on fracture propagation, all three layers were given the properties of the Carynginia Formation. The thickness of the upper, middle, and lower layers are 3 m, 8 m, and 3 m, respectively. The in-situ stresses applied to the model were similar to the field conditions for Kockatea, Carynginia, and IRCM Formations but scaled down as mentioned before. In this case study, the horizontal stresses within each layer are assumed to be constant. For the upper and lower layers  $\sigma_H = 5 \text{ MPa}$ ,  $\sigma_h = 3 \text{ MPa}$  and for the middle layer,  $\sigma_H = 3 \text{ MPa}$ ,  $\sigma_h = 1 \text{ MPa}$ . The vertical stress  $\sigma_v$  is assumed to be 6.6 MPa for the whole sample. The hydraulic fracturing simulation results are shown in Figure 4.9 and Figure 4.10.

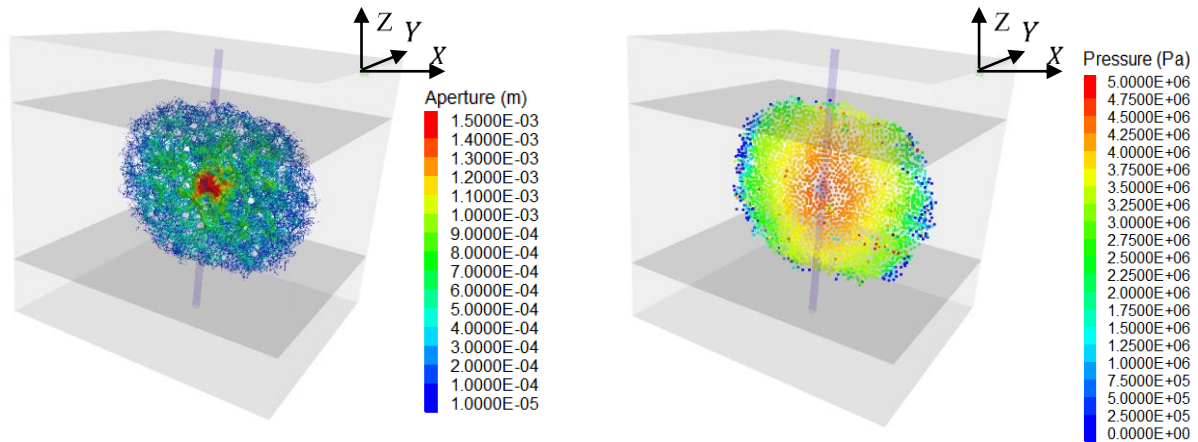


Figure 4.9 Case 3. Three-layer model. Aperture (left) and fracture pressure (right) distribution

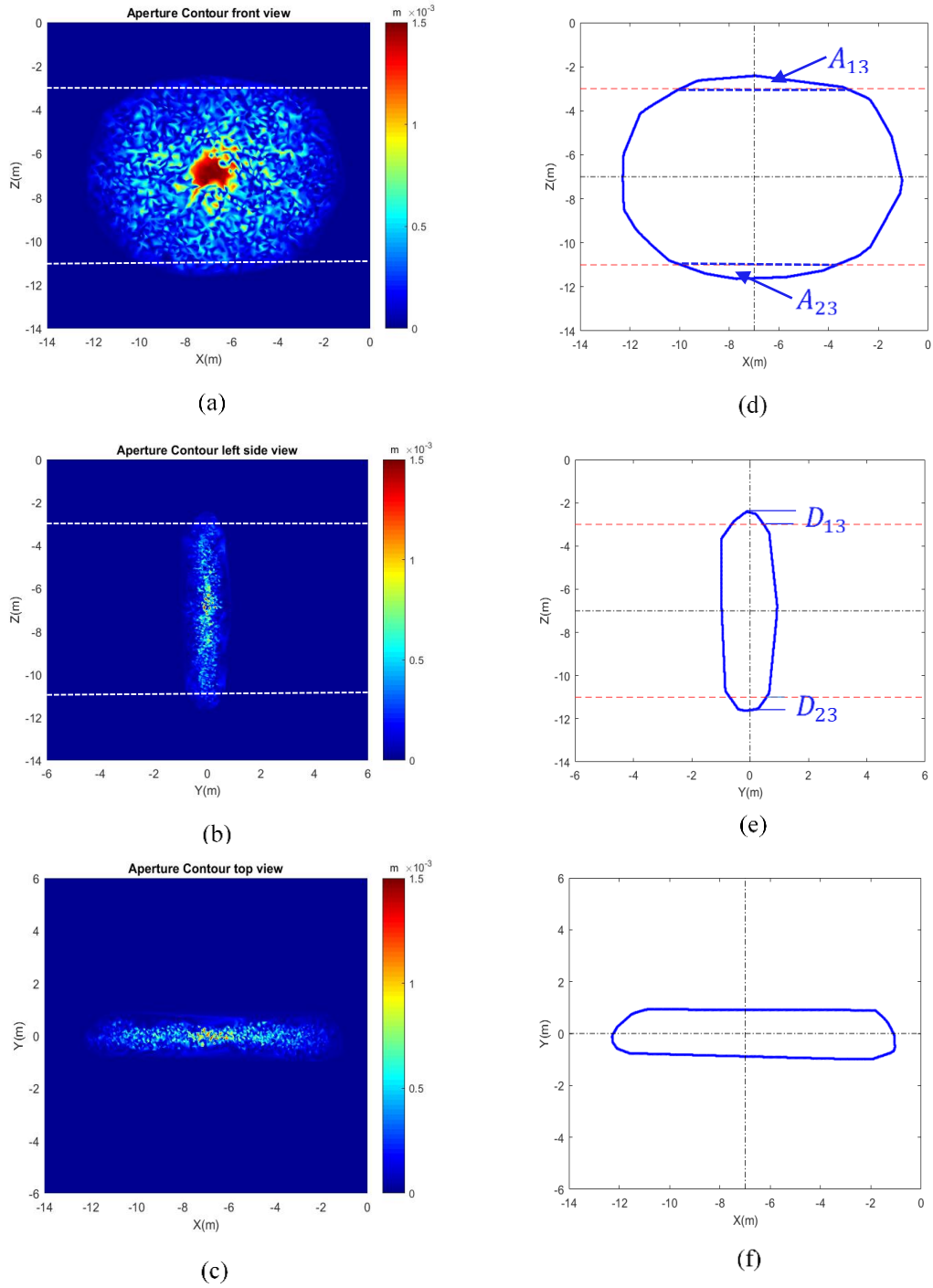


Figure 4.10 Aperture contours after 8 second for case 3: (a) front view; (b) left side view; (c) top view; (d) front view outline; (e) left side view outline; (f) top view outline



The aperture profiles from Figure 4.9 (a) and Figure 4.10 (a) show that the geometry of the hydraulic fracture deviates from the penny shape. Despite the fracture penetrates slightly into the upper and the lower layers, it exhibits containment in both layers, as is shown in Figure 4.10. The penetration parameters in this case ( $A_{13}$ ,  $A_{23}$ ,  $D_{13}$ , and  $D_{13}$ ) are much less than the respective parameters of Case 1 (see Table 4.3), confirming fracture containment by both layers. The containment of hydraulic fracture in the horizontal direction results from the increase in minimum horizontal stress which is perpendicular to the hydraulic fracture plane (i.e., stress barrier).  $A_{13}$  and  $D_{13}$  are also smaller than  $A_{12}$  and  $D_{12}$ , respectively, indicating that the effect of stress barrier has larger influence than decrease of rock brittleness on resisting vertical fracture propagation.

#### 4.3.4 Case 4: Three-layer model, different rock properties and stresses

This model studies the combination effects of different rock properties and in-situ stresses on the propagation of hydraulic fracture. The model has three layers with thicknesses of 3 m, 8 m, and 3 m and rock properties of Kockatea, Carynginia, and IRCM Formations (see Table 4.1) from upper to lower layers, respectively. In-situ stresses same as in Case 3 was applied to the model. This model represents the real formation properties and in-situ stresses corresponding to the NPB. The results are shown in Figure 4.9 and Figure 4.10.

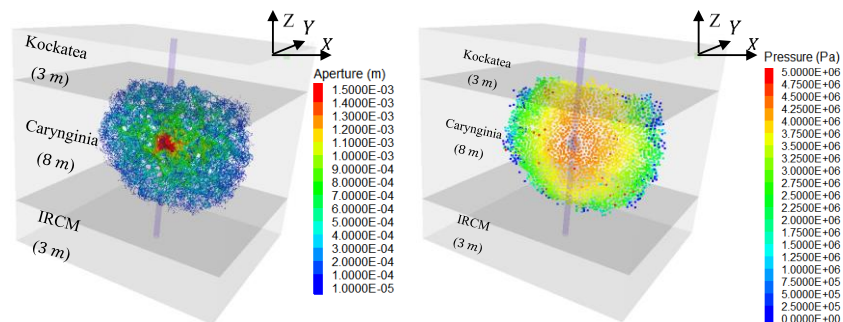


Figure 4.11 Case 4: Three-layer model, different rock properties and stresses. Aperture (left) and fracture pressure (right) distribution

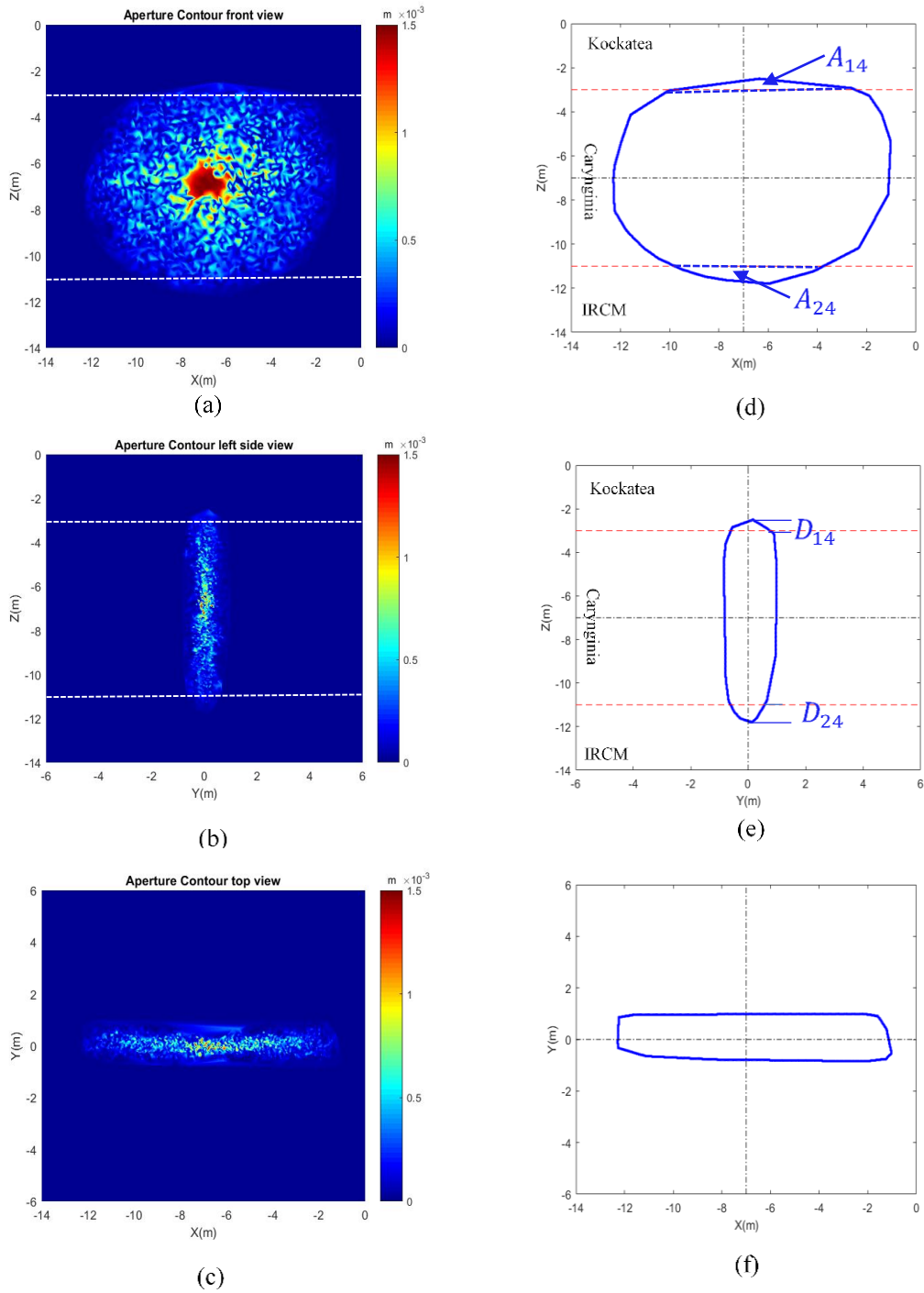


Figure 4.12 Aperture contours after 8 second hydraulic fracture simulation for case 4: (a) front view; (b) left side view; (c) top view; (d) front view outline; (e) left side view outline; (f) top view outline

The geometry of the hydraulic fracture as shown in Figure 4.11 (a) and Figure 4.12 (a) and (d) deviates from penny shape. As is seen from Table 4.3, all penetration parameters ( $A_{14}$ ,  $A_{24}$ ,  $D_{14}$ ,  $D_{24}$ ) in this case are less than that of Case 1, suggesting that the hydraulic fracture is contained. However,  $A_{14}$  and  $D_{14}$  are less than  $A_{24}$  and  $D_{24}$ , respectively, indicating that the hydraulic fracture is less contained by IRCM Formation comparing to Case 4. This result may indicate that the increase of brittleness facilitates fracture propagation despite the presence of stress barrier leading to containment. Comparing Case 4 with Case 3,  $A_{14}$  and  $D_{14}$  are less than  $A_{13}$  and  $D_{13}$ , respectively. The results further confirm that under same in-situ stress conditions, decrease of brittleness resists fracture propagation. In addition,  $A_{24}$  and  $D_{24}$  are larger than  $A_{23}$  and  $D_{23}$ , respectively. The results also confirm that under same stress conditions, increase of brittleness favors fracture propagation.

To sum up, the propagation of hydraulic fracture in the Carynginia Formation is highly influenced by both the change of rock properties and increase of minimum horizontal stress at the upper and lower layers. If the fracture propagates closer to the Kockatea-Carynginia Formation interface, the decrease in rock brittleness and the increase of minimum horizontal stress tends to cause containment, leading to easier propagation of hydraulic fracture in the horizontal direction. On the other hand, if the hydraulic fracture propagates near the lower Carynginia-IRCM Formation interface, the increase in rock brittleness favors the hydraulic fracture to propagate in the vertical direction. However, the increase of minimum horizontal stress resists the vertical migration of the hydraulic fracture in reverse.

## 4.4 Field Scale Simulation

A field scale simulation (Case 5) was performed representing hydraulic fracturing under NPB formation properties and in-situ stress conditions. The sample dimension for the laboratory experiment (Rasouli and Sutherland, 2014) was upscaled to a model with  $350\text{ m} \times 250\text{ m} \times 350\text{ m}$  (length (L)  $\times$  width (W)  $\times$  height (H)) to represent the field scale. The reference point was placed at the center of the right top side of the model. The thickness of the three layers are 50 m, 250 m, 50 m for the upper, middle, and lower layers, respectively. The thickness of the middle layer in the model corresponds to that of the Carynginia Formation in the field, while the thicknesses of the upper and lower layers were reduced to allow faster simulation. Two soft layers with thicknesses of 20 m and Young's modulus of 0.3 GPa were placed at  $Y = 115\text{ m}$  and  $Y = -115\text{ m}$ . The main lattice resolution between  $Y = -50\text{ m}$  and  $Y = 50\text{ m}$  was set to be 6 m, while that of the rest of the model was set to be 10 m. Sub-lattice resolution of 1.5 m was used for faster simulation.

The in-situ horizontal stresses were set to be the same with that of Case 3 for three layers. The vertical stress ( $\sigma_v$ ) was set to be 15 MPa at the center of the model with a gradient of 0.026 MPa/m. The rock properties of the three layers correspond to that of the Kockatea, Carynginia, and IRCM Formations, respectively, as shown in Table 4.1. The simulation results of Case 5 are shown in Figure 4.13 and Figure 4.14 and compared with the results of the M-asymptotic solution (Case 6) shown in Figure 4.15.

A crosslinked fracturing fluid with an average viscosity of 240 cp (0.24 Pa·s) was injected with an injection rate of  $0.2\text{ m}^3/\text{s}$ . The fluid was injected via a cluster with radius of 6 m and an initial crack with radius of 10 m and aperture of 0.0002 m in XZ plane. Under these conditions, the

fracture will propagate in the viscosity dominated regime when injection time is 2000 s because  $\kappa$  calculated using equation (1) will be less than 1.

Table 4.4 Penetration areas and depths for field scale simulations

Case No. $i$	$A_{1i}$ , m <sup>2</sup>	$A_{2i}$ , m <sup>2</sup>	$D_{1i}$ , m	$D_{2i}$ , m
5	52.43	1415.2	1.4	16.1
6	4008.2	4008.2	31.34	31.34

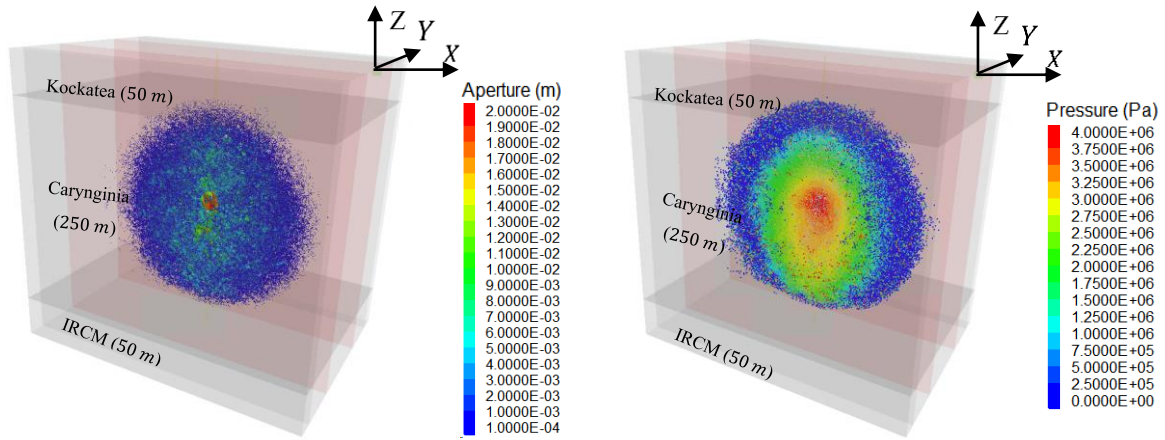


Figure 4.13 Case 5: Field scale simulation. Aperture (left) and fracture pressure (right) distribution

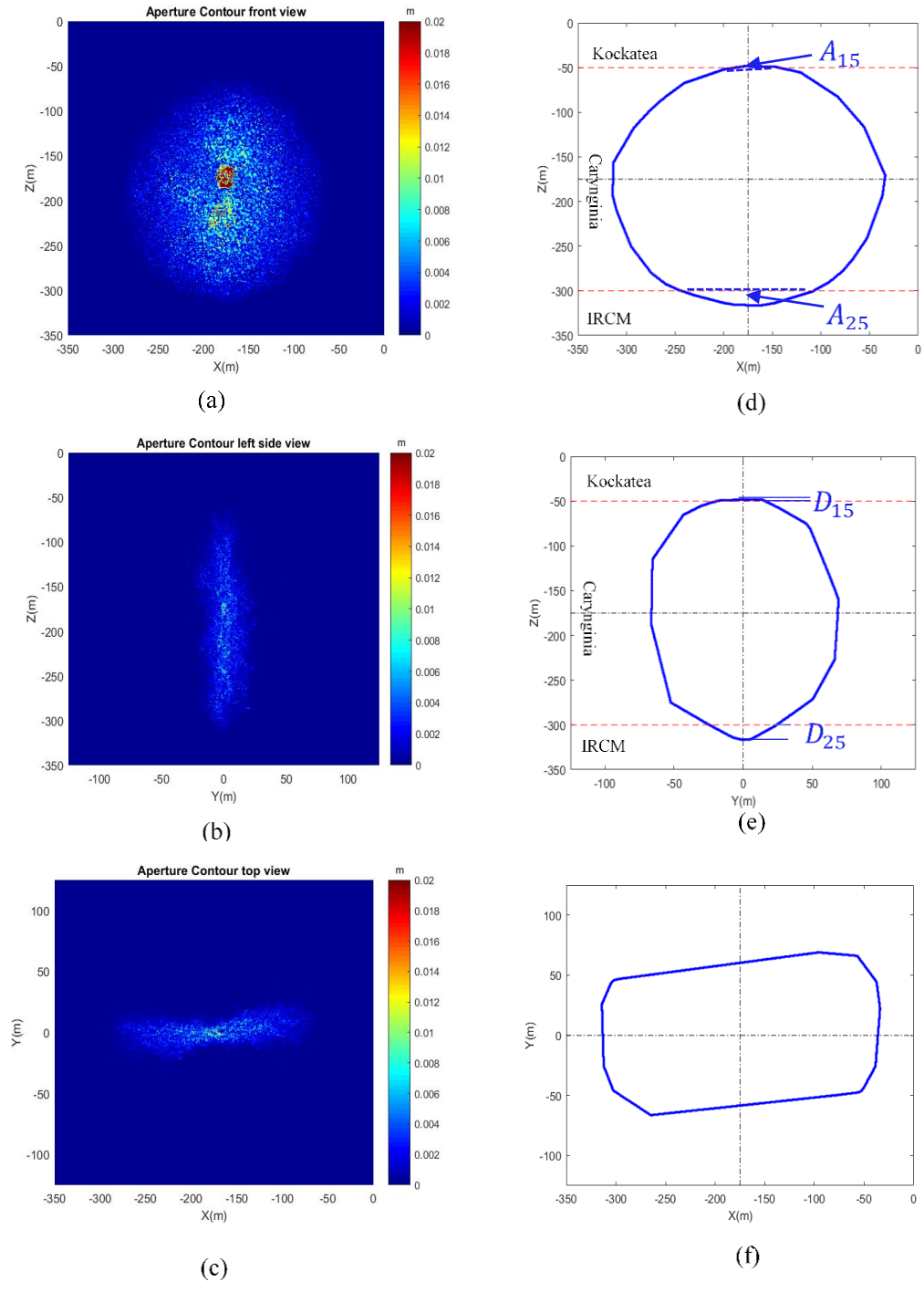


Figure 4.14 Aperture contours after 2000 second hydraulic fracture simulation for case 5: (a) front view; (b) left side view; (c) top view; (d) front view outline; (e) left side view outline; (f) top view outline

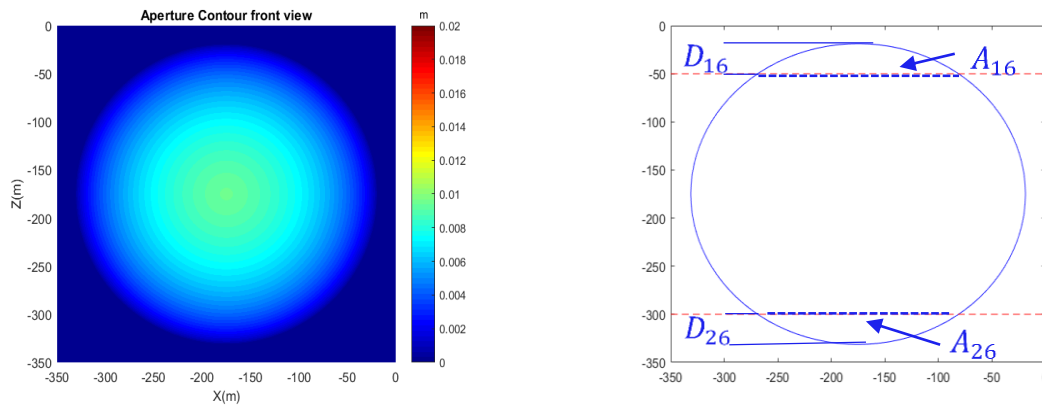


Figure 4.15 Viscosity dominated regime asymptotic solution for aperture contour (left) and outline (right) after 2000 second

The front view of fracture geometry for Case 5 slightly deviates from the penny shape, as are shown in Figure 4.13 and Figure 4.14. However, comparing the front view fracture outline of Case 5 with that of Case 6, the fracture grows less in both horizontal and vertical directions, as are shown in Figure 4.14 (d) and Figure 4.15 (right). This may result from the energy loss during fracture propagation due to the growth of numerous branches of micro cracks near the main fracture plane in the numerical field scale model. The side and top views of the fracture outline, as are shown in Figure 4.14 (e) and (f), for the numerical field scale model suggest that the micro cracks are distributed with a wide range in Y direction. In the field scale model, the effects of low stress anisotropy and random lattice distribution on the growth of branches of micro cracks may be manifested.

The penetration parameters for both numerical and analytical field scale models are calculated and summarized in Table 5. The penetration parameters for numerical model ( $A_{15}$ ,  $A_{25}$ ,  $D_{15}$ ,  $D_{25}$ ) are much smaller than those of analytical model ( $A_{16}$ ,  $A_{26}$ ,  $D_{16}$ ,  $D_{26}$ ) suggesting the fracture is

contained in both upper and lower layers for Case 5 due to the increase of minimum horizontal stresses. However,  $A_{26}$  and  $D_{26}$  are much larger than  $A_{16}$  and  $D_{16}$ , respectively, indicating that fracture propagates more easily in IRCM Formation than in Kockatea Formation. The field scale numerical model of Case 5 validates the results of intermediate scale model presented as Case 4.

## 4.5 Summary

In this chapter the intermediate and field scale hydraulic fracturing simulations for Kockatea, Carynginia, and IRCM Formations in the NPB, Australia were conducted. The simulation results of the simple one-layer model can be matched with the laboratory results. Penetration parameters were proposed to quantify fracture containment. The simulation results of all cases with various rock properties and in-situ stresses indicates that the increase in rock brittleness favors hydraulic fracture propagation. Also, the increase in minimum horizontal stress and decrease in vertical stress resists vertical migration of hydraulic fracture initiated at the Carynginia Formation and results in fracture containment.

The next chapter will present an integrated hydraulic fracturing and production model for history matching and prediction of shale gas production. Two clustering algorithms will be proposed for characterizing fracture geometry. Lattice-Boltzmann Method (LBM) will be applied for modeling gas slippage effect during shale gas production. Impacts of matrix and fracture permeability on shale gas production will be investigated.



# Chapter 5

## Integrated Hydraulic Fracturing and Production

### Model

This Chapter is modified from the preprint: Wan et al. (2020b).

#### 5.1 Introduction

The Middle Devonian Marcellus shale play has evolved into the largest producing shale gas field in the United States with an estimated area of 44,000 square miles, and its daily gas production reached 16 billion cubic feet in 2015 (Zagorski et al., 2017). To estimate stimulation efficiency and predict shale gas production in Marcellus shale play, an integrated hydraulic fracturing and production forecast model is needed. A novel integrated approach that couples hydraulic fracturing and production simulation was proposed for Marcellus shale gas reservoir. A discrete element method based hydraulic fracturing simulator was utilized for multi-stage hydraulic fracturing simulation. Moving tip clustering and linear regression clustering algorithms were proposed to characterize the complex fracture geometry. Embedded discrete fracture model method was used to transfer the complex geometry of multiple fractures into a third-party reservoir simulator for history matching of shale gas production and production forecasting. It was observed that the linear regression clustering algorithm can generate smooth fracture geometries and detect overall fracture

paths reasonably. The moving tip clustering algorithm, however, can capture more branches of microcracks and recover zig-zag fracture paths with larger apparent fracture lengths. The zig-zag fractures contribute to larger stimulated reservoir volume and result in higher production than the smooth fractures. Effects of gas slippage in the nanopores, fracture closure, and matrix shrinkage on shale gas production were also analyzed. The gas slippage effect contributes to higher production at the late stage due to reservoir depletion. Reduction of fracture conductivity and matrix permeability due to decreasing bottomhole pressure leads to decrease of gas production and should be taken into account for long-term production prediction.

## **5.2 Multi-stage hydraulic fracturing simulation using lattice model**

Real shale gas data was used for fracture propagation simulation. The reservoir condition and well information are similar to that in (Yu et al., 2018b). The length ( $L$ ), width ( $W$ ), and height ( $H$ ) of the model are 2,168 ft, 1,000 ft, and 100 ft, respectively. A horizontal well was placed at the center of the model with 7 injection stages and 3 clusters per stage. The cluster spacing in each stage and the distance between adjacent stages are 68 ft and 136 ft, respectively. Water was injected into each stage for 128 minutes with a flow rate of 60 BPM. Young's modulus and Poisson's ratio of the reservoir model are  $3 \times 10^6$  psi and 0.23 respectively. The contrast between maximum horizontal stress ( $S_H$ ) and minimum horizontal stress ( $S_h$ ) is 1,000 psi. The model dimension, in-situ stresses directions, and fracture distribution after the total injection time of 896 minutes are shown in Figure 5.1. The blue dots indicate the location of all the microcracks which can be combined to form hydraulic fractures. It is observed that all the fractures deviate from the transverse direction and some fractures merge into each other. Another observation is that the fracture lengths of different

clusters are different. The reorientation of fracture indicates that the propagation of one fracture creates stress shadow effect, thus interfere the growth of other fractures (Warpinski and Branagan, 1989; Palmer, 1993). Note that the model assumes that after one stage of hydraulic fracturing injection, the next stage starts injection immediately without shut-in period between stages. The fracture pressure in the previous stage is not released, thus the stress shadow is likely to be overestimated. For the field application, the shut-in period between stages tends to result in fracture closure and shrinkage of stress shadow. Consequently less fracture interaction would occur. The variation of fracture lengths derives from different amounts of fluid and proppants distributed in each cluster, the results can be indicated by microseismic data in the field (Ross and Bustin, 2007; Fu and Bunger, 2019). Further investigations are needed for simulating multi-stage hydraulic fracturing using the hydraulic fracturing simulator, but the main objective of this work is to build an integrated hydraulic fracturing-production model.

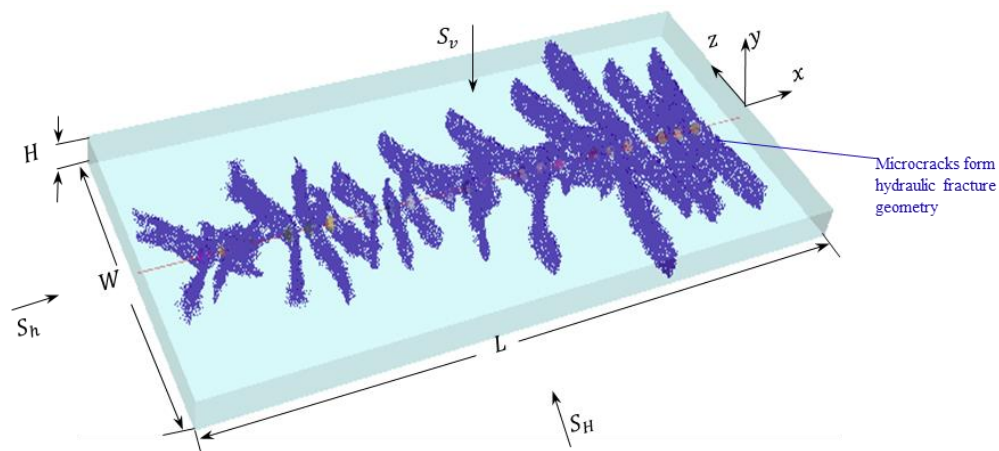


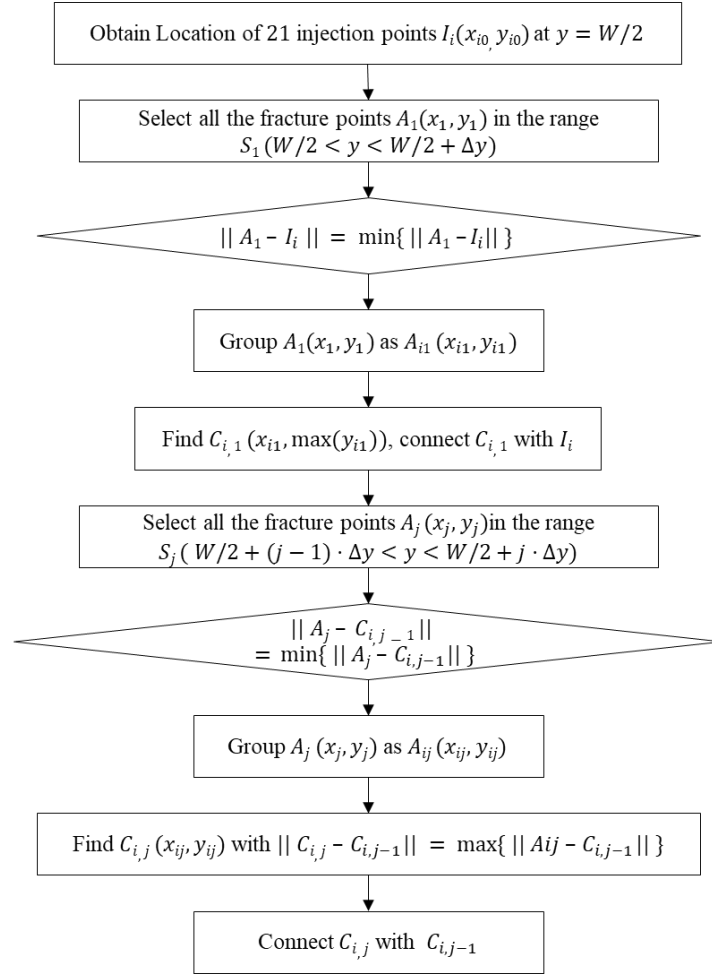
Figure 5.1 Lattice simulation of multi-stage hydraulic fracturing model.

## 5.3 Fracture geometry characterization

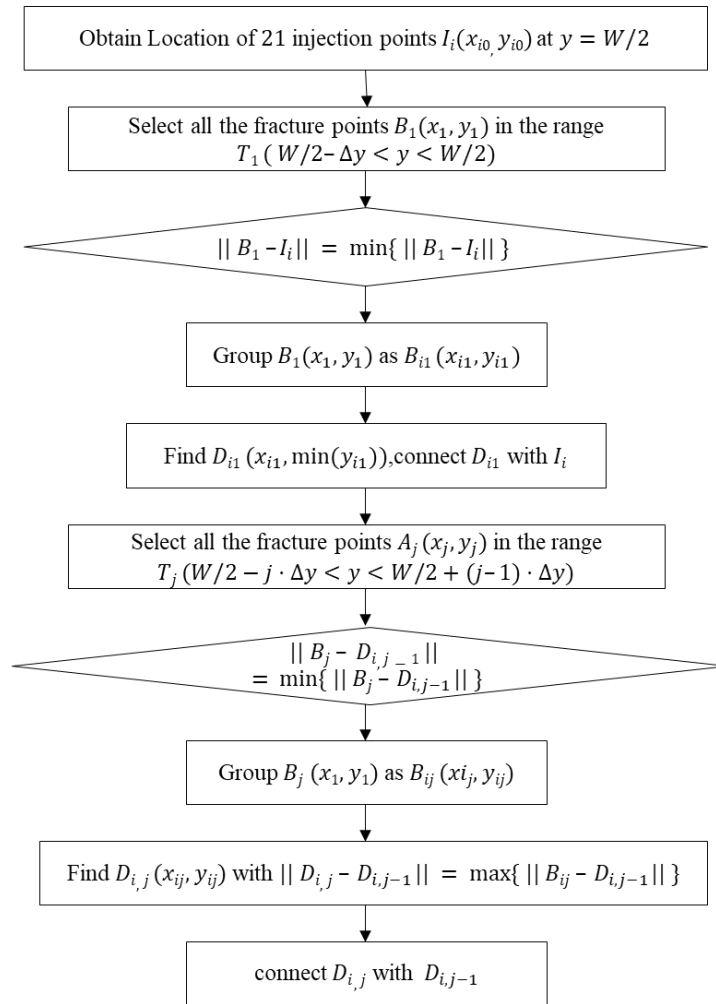
The location of hydraulic fractures simulated by the hydraulic fracturing simulator are presented in the form of microcracks. However, this form of fractures cannot be directly imported into reservoir simulator for production simulation. Moving tip clustering algorithm and linear regression clustering algorithm were implemented to describe complex fracture geometry in the hydraulic fracturing simulator for reservoir simulation.

### 5.3.1 Moving tip clustering algorithm

The workflow and an example of the moving tip clustering algorithm are shown in Figure 5.2 and Figure 5.3, respectively. The algorithm starts by locating all the injection points  $I_i$  ( $i = 1, 2, \dots, N$ , where  $N$  is the total number of clusters). Then microcrack dots in the range of  $S_1$  ( $W/2 < y < W/2 + \Delta y$ ) and  $T_1$  ( $W/2 - \Delta y < y < W/2$ ) were selected and classified. A dot was classified into cluster  $i$  if it has the shortest distance to the injection point  $I_i$ . Then the “tip”  $C_{i,1}$  with the largest  $y$  value and “tip”  $D_{i,1}$  with the lowest  $y$  value were obtained in the range  $S_1$  and  $T_1$ , respectively and connected to  $I_i$  to form planar cracks. In the following step  $j$ , microcrack dots in the range of  $S_j$  ( $W/2 + j \cdot \Delta y < y < W/2 + (j + 1) \cdot \Delta y$ ) and  $T_j$  ( $W/2 + (j - 1) \cdot \Delta y < y < W/2 + j \cdot \Delta y$ ) were selected and grouped. A dot in range  $S_j$  or  $T_j$  was classified into cluster  $i$  if it has the shortest distance to the “tip” in the previous step  $C_{i,j-1}$  or  $D_{i,j-1}$ , respectively. Then “tips”  $C_{i,j}$  and  $D_{i,j}$  with the maximum distance to  $C_{i,j-1}$  were obtained and connected to  $C_{i,j-1}$  and  $D_{i,j-1}$ , respectively to form planar cracks.

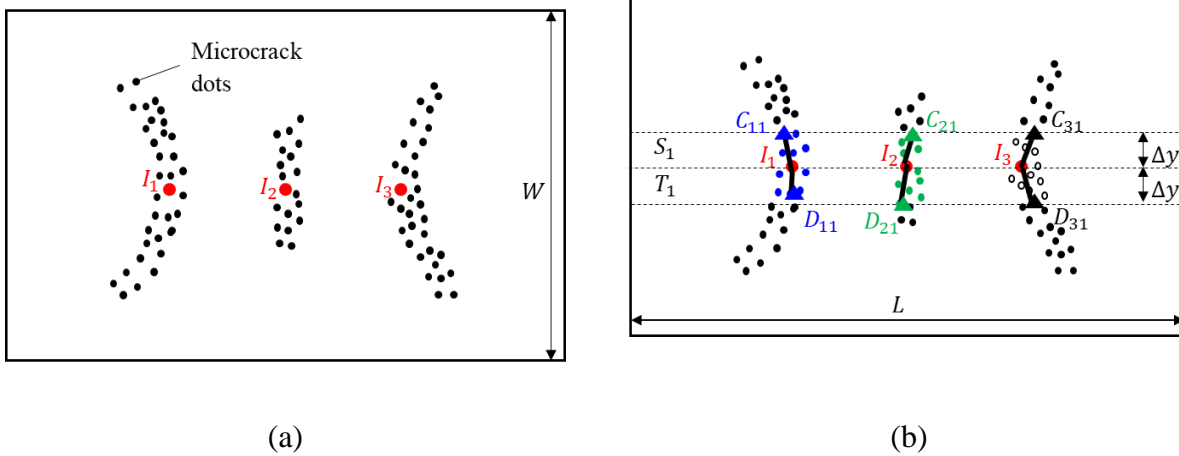


(a)



(b)

Figure 5.2 Moving tip clustering algorithm workflow for: (a)  $y > W/2$ , (b)  $y < W/2$ .



(a)

(b)

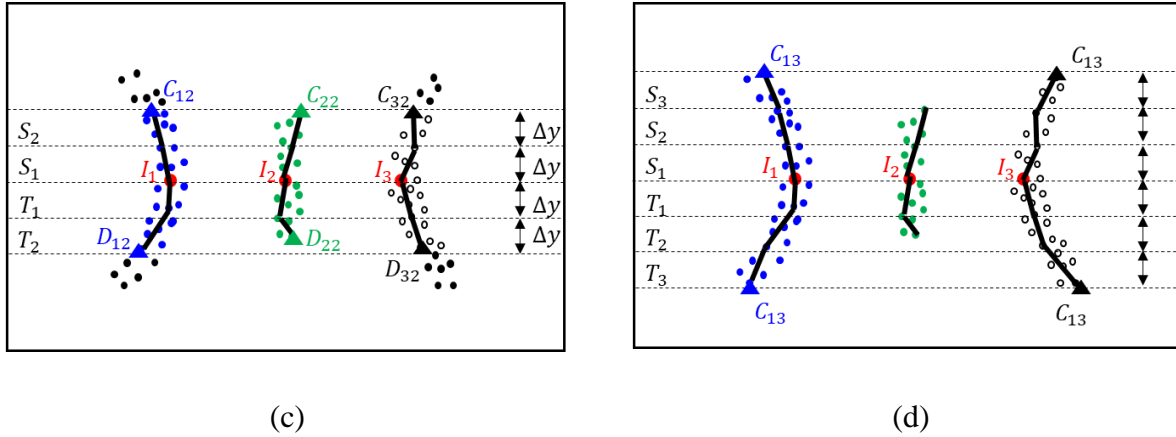
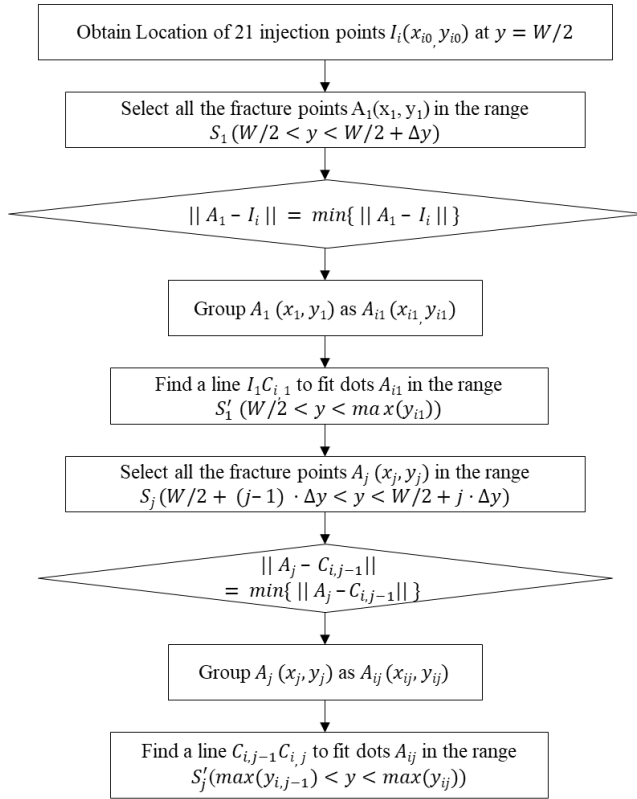


Figure 5.3 Moving tip clustering algorithm for ( $N = 3$ ) clusters: (a) locate the three injection points, (b) group microcrack dots in range  $S_1$  and  $T_1$  into the three clusters and locate fracture “tips” in this range, (c) group microcrack dots in range  $S_2$  and  $T_2$  into the three clusters and locate fracture “tips” in this range, (c) group microcrack dots in range  $S_3$  and  $T_3$  into the three clusters and locate fracture “tips” in this range.

### 5.3.2 Linear regression clustering algorithm

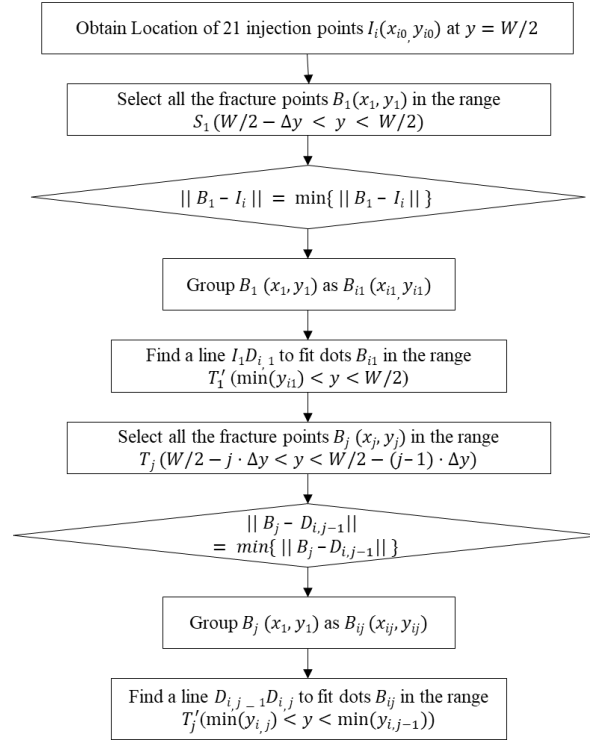
The linear regression clustering algorithm is similar to the moving tip clustering algorithm. In each step, instead of finding a new “tip” that is furthest to the previous “tip”, a line segment is used to linearly fit all the dots in the range  $S_j$  ( $W/2 + j \cdot \Delta y < y < W/2 + (j + 1) \cdot \Delta y$ ). The line segment shares an endpoint of the line in the previous step and has another endpoint with the maximum  $y$  magnitude of the dots in this range. The workflow and an example of the linear regression clustering algorithm are shown in Figure 5.4 and Figure 5.5, respectively.

Comparison of Figure 5.5(d) and Figure 5.3(d) suggests that the fracture segments generated by the linear regression clustering algorithm tend to be centralized in the “dot cloud”. Whereas, the fracture segments created by the moving tip clustering algorithm may randomly go to the sides or centers of the “dot cloud”.



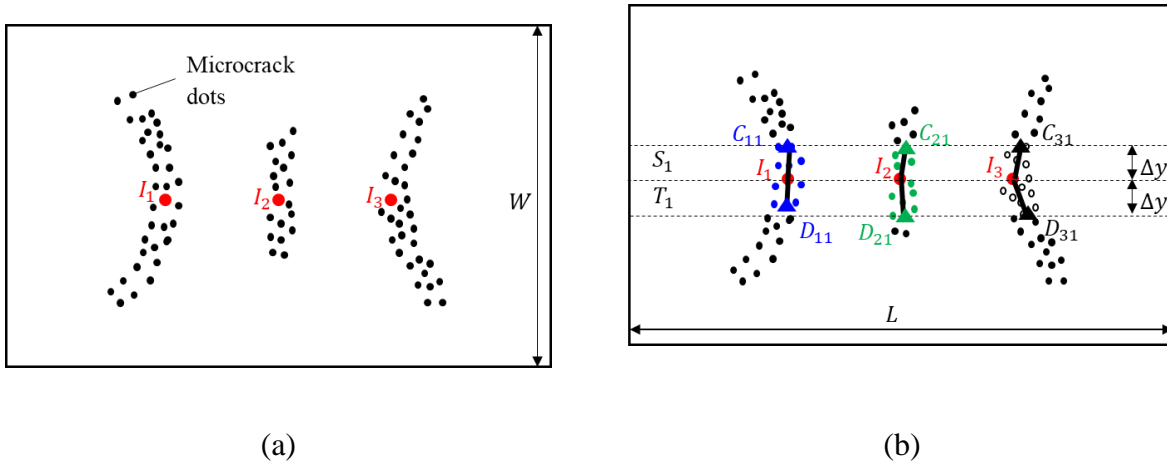
(a)





(b)

Figure 5.4 Linear regression clustering algorithm workflow for: (a)  $y > W/2$ , (b)  $y < W/2$ .



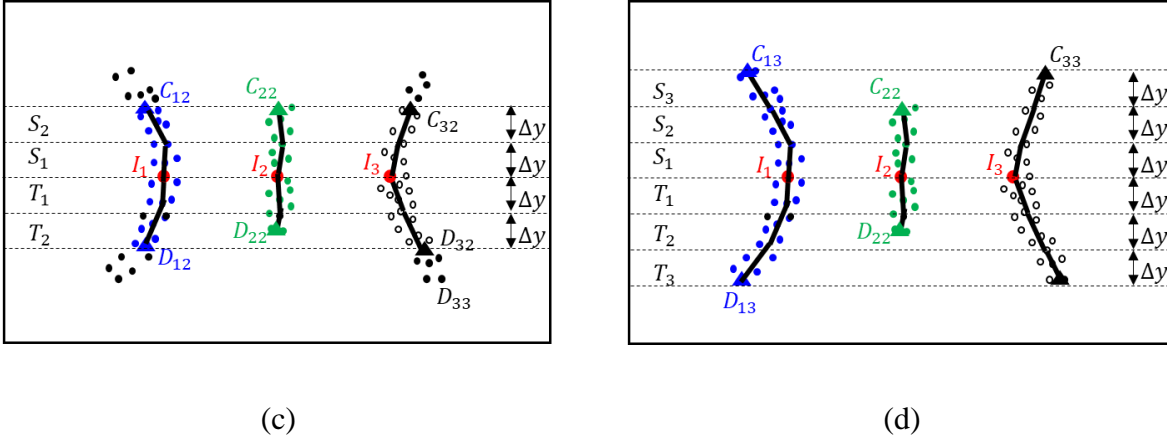


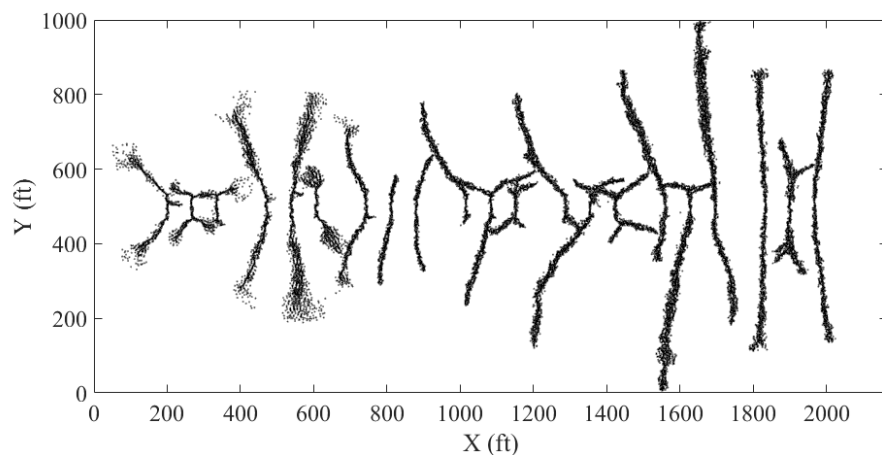
Figure 5.5 Linear regression clustering algorithm for ( $N = 3$ ) clusters: (a) locate the three injection points, (b) group microcrack dots in range  $S_1$  and  $T_1$  into the three clusters and find a linear fit line segment in the range  $S'_1$  and  $T'_1$ , (c) group microcrack dots in range  $S_2$  and  $T_2$  into the three clusters and find a linear fit line segment in the range  $S'_2$  and  $T'_2$ , (d) group microcrack dots in range  $S_3$  and  $T_3$  into the three clusters and find a linear fit line segment in the range  $S'_3$  and  $T'_3$ .

### 5.3.3 Fracture identification

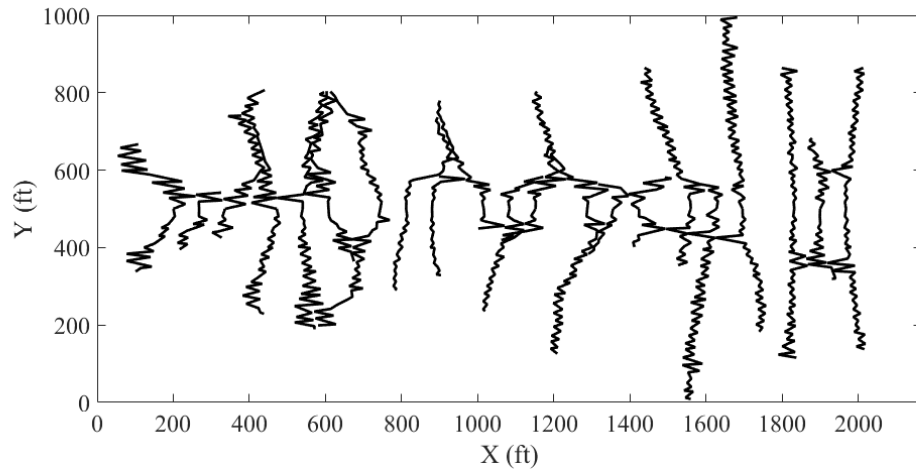
The fracture geometry simulated in the hydraulic fracturing simulator as shown in Figure 5.1 was simplified into a 2D constant height fracture model. The microcracks in the range of  $H/2 - \Delta z < z < H/2 + \Delta z$  ( $\Delta z = 5\text{ft}$ ) were taken to determine the paths of the fracture cross sections, as shown in Figure 5.6(a). Since the fractures mainly grew in length, the variation of fracture front was neglected. The 2D fracture paths were captured using both moving tip clustering and linear regression clustering algorithms as shown in Figure 5.6(b) and (c), respectively. The corresponding 3D fracture paths for two algorithms are shown in Figure 5.7(a) and (b), respectively.

It is observed that the fracture paths in Figure 5.6(b) and Figure 5.7(a) exhibit a zig-zag configuration. This observation indicates that the moving tip clustering algorithm tends to generate fracture paths with large roughness whereas, the fracture paths determined by linear regression clustering algorithm, as shown in Figure 5.6(c) and Figure 5.7(b), exhibit smoother fracture paths.

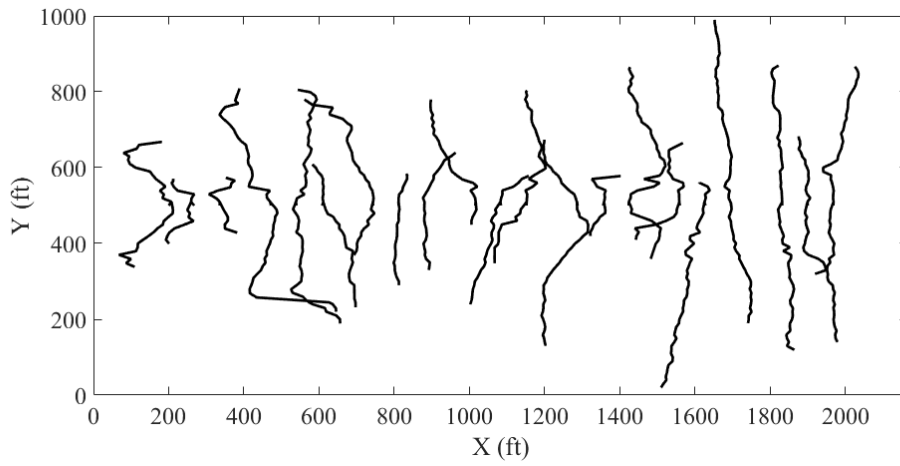
For both methods, apparent fracture half-length ( $L_f$ ) of each fracture can be calculated by adding the lengths of all the fracture segments. The average apparent fracture half-length ( $\overline{L}_f$ ) was calculated by averaging the apparent fracture half-length of each fracture. The  $\overline{L}_f$  calculated from the moving tip clustering and linear regression clustering algorithms are 574.6 ft and 285.6 ft, respectively when step length  $\Delta y = 10$  ft is used. Further investigation is needed to analyze the impact of  $\Delta y$  on  $\overline{L}_f$  and resulting simulated production. The linear regression clustering algorithm allows the main fracture paths to be detected from the microcracks dots. However, the algorithm may underestimate the apparent fracture lengths contributed by the branches of microcracks because most microcracks were not connected to the main paths. On the contrary, the moving tip clustering algorithm is capable of capturing apparent fracture lengths contributed by the branched microcracks by generating fracture paths with high roughness. The fracture paths by both algorithms can be compared with complex hydraulic fractures simulated using DDM method, as shown in Figure 5.7(c), by (Yu et al., 2018a). Both fracture paths are used to simulate production history.



(a)

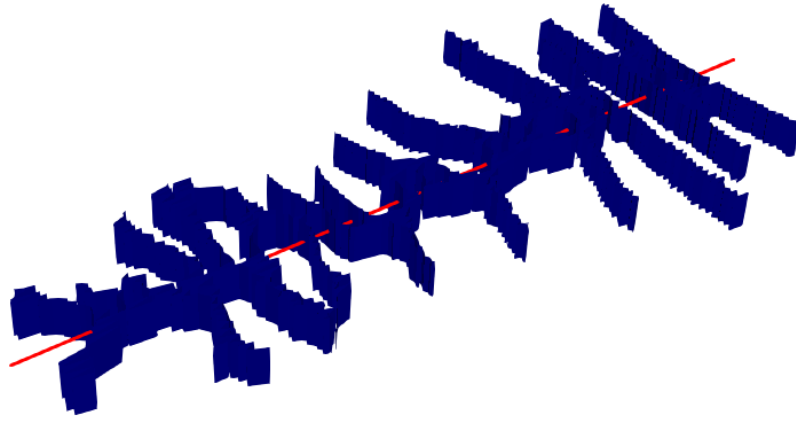


(b)

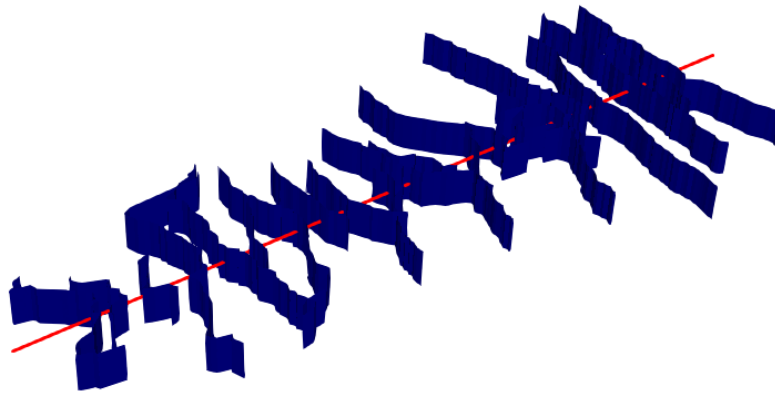


(c)

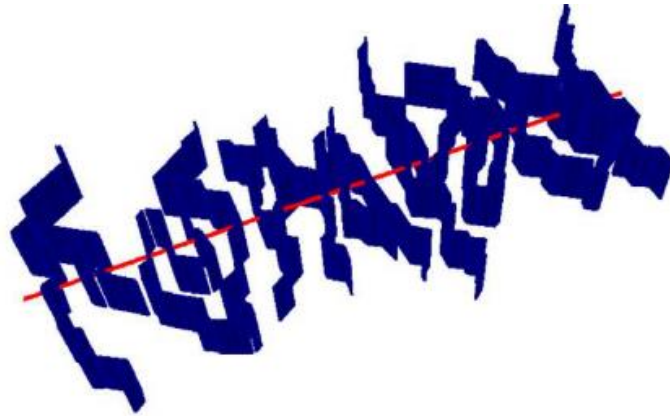
Figure 5.6 Multi-stage hydraulic fracturing simulation: 2D cross section plots of (a) microcracks distribution in the hydraulic fracturing simulator, (b) fracture paths based on moving tip clustering algorithm, (c) fracture paths based on linear regression clustering algorithm.



(a)



(b)



(c)

Figure 5.7 3D fracture paths using (a) moving tip clustering algorithm, (b) linear regression clustering algorithm, (c) DDM method (Yu et al., 2018a).

## 5.4 Gas slippage simulation using LBM

The gas slippage effect in the nanopores of the shale gas reservoir was simulated using LBM method. The mechanism of LBM derives from Boltzmann's work of describing gas particle interaction by notions of streaming and collision process. LBM simplified Boltzmann's theory by reducing particle positions, confining velocity directions and magnitudes, and discretizing time into multiple steps. D2Q9 model is a 2D LBM that consists of 9 velocities for each lattice node, as shown in Figure 5.8.  $e_a$  denotes the microscopic velocity of the lattice, where  $a = 0, 1, 2, \dots, 8$  represents the direction index (Sukop and Thorne, 2006).

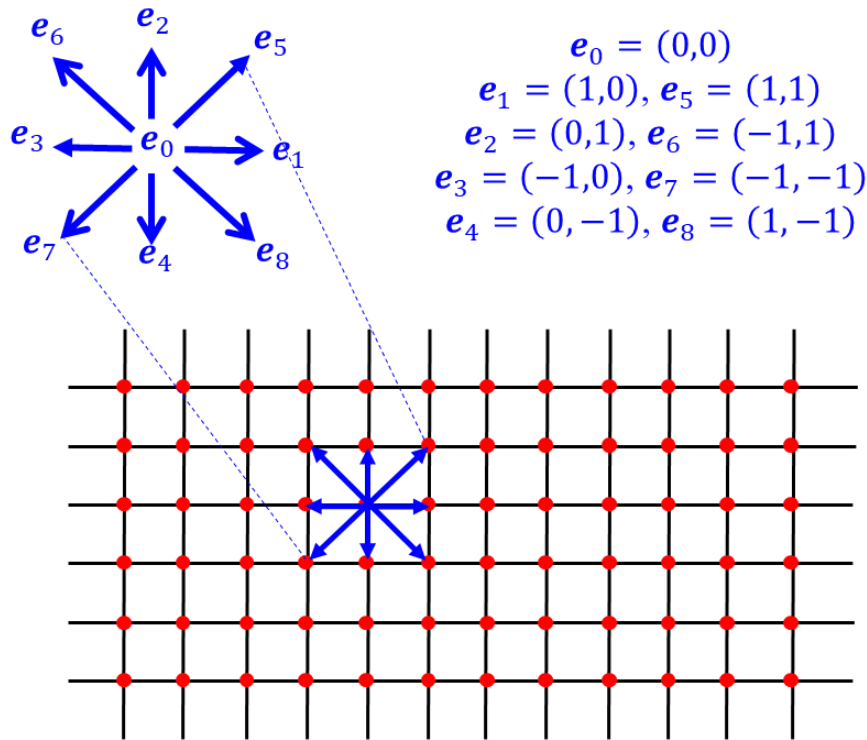


Figure 5.8 Lattices and velocities of the D2Q9 model (modified from Sukop and Thorne, 2006).

The macroscopic fluid density and velocity are obtained by integration of microscopic properties as:

$$\rho = \sum_{a=1}^8 f_a, \quad (6)$$

$$\mathbf{u} = \frac{1}{\rho} \sum_{a=1}^8 f_a \mathbf{e}_a, \quad (7)$$

where  $f_a$  is the local weighted directional density.

The general form of LBM equation is shown in equation (8), where the left-hand side represents the streaming process and the right-hand side represents the collision process.

$$f_a(\mathbf{x} + \mathbf{e}_a \Delta t, t + \Delta t) - f_a(\mathbf{x}, t) = -\frac{f_a(\mathbf{x}, t) - f_a^{eq}(\mathbf{x}, t)}{\tau}. \quad (8)$$

Here,  $\tau$  is the nondimensional relaxation factor

The equilibrium distribution function  $f_a^{eq}$  can be obtained by:

$$f_a^{eq}(\mathbf{x}) = w_a \rho(\mathbf{x}) [1 + 3\mathbf{e}_a \mathbf{u} + 4.5(\mathbf{e}_a \mathbf{u})^2 - 1.5\mathbf{u}^2], \quad (9)$$

where the weight functions  $w_a$  are 4/9 for  $a = 0$ , 1/9 for  $a = 1, \dots, 4$ , and 1/36 for  $a = 5, \dots, 8$ .

The boundary condition for LBM simulation of gas slippage in nanopores is a combination of empirical bounce back rule and specular reflection (Zhang et al., 2005):

$$f_a = (1 - c)f_{bb} + cf_{sr}. \quad (10)$$

$\tau$  in equation (8) should be modified into  $\tau_m$  by taking into account the Knudsen number ( $K_n$ ) for gas slippage in nanopores:

$$\tau_m = \tau \frac{2}{\pi} \arctan \left( \sqrt{2} K_n^{-\frac{3}{4}} \right), \quad (11)$$

where  $K_n$  is obtained from:

$$K_n = \frac{c_B T}{\sqrt{2\pi} P D^2 L_c}. \quad (12)$$

In this equation,  $c_B$  is the Boltzmann constant,  $T$  is the ambient temperature,  $P$  is the pressure of the fluid, and  $L_c$  is the characteristic flow length.

The dynamic viscosity  $\nu$  is calculated as:

$$\nu = \frac{\Delta x^2 (\tau - 0.5)}{3\Delta t}. \quad (13)$$

The ratio of the apparent permeability over intrinsic permeability  $\gamma$  is calculated using:



$$\gamma = \frac{8Q\mu L}{\Delta P A R^2}, \quad (14)$$

where  $Q$  is the flow rate,  $\mu$  is the kinematic fluid viscosity,  $L$  is the flow length,  $\Delta P$  is the pressure drop,  $A$  is the cross-section area of the fluid, and  $R$  is the intrinsic radius of the pores (Yu et al. 2018a).

## 5.5 Modeling multiple complex hydraulic fractures using EDFM

Developed by Xu (2015), the non-intrusive EDFM method is capable of modeling gas flow in a reservoir which has complex hydraulic and natural fractures with high accuracy and computational efficiency (Xu, 2015; Xu et al., 2017a; Xu et al., 2017b; Yu et al., 2018a; Yu et al., 2018b; Fiallos et al., 2019). In this approach, complex fractures are embedded into the matrix cells explicitly, enabling simulation of fluid flow between fracture, matrix, and well cells based on non-neighboring connections (NNCs) (Moinfar, 2013; Xu, 2015). The accuracy of the EDFM approach was demonstrated by comparing the fracture geometry and pressure profiles using EDFM, local grid refinement (LGR), and semi-analytical solution (Xu et al., 2017a; Yu et al., 2018).

## 5.6 History matching and production prediction

The fracture paths detected by both moving tip and linear regression clustering algorithms were imported into the reservoir simulator using EDFM method. The conductivity of the hydraulic fractures is 4 md-ft for the two cases. The intrinsic matrix permeability  $k_i$  for both cases is 1000 nD. The reservoir dimension is corresponding to the multi-stage hydraulic fracturing model as shown in Figure 5.1.

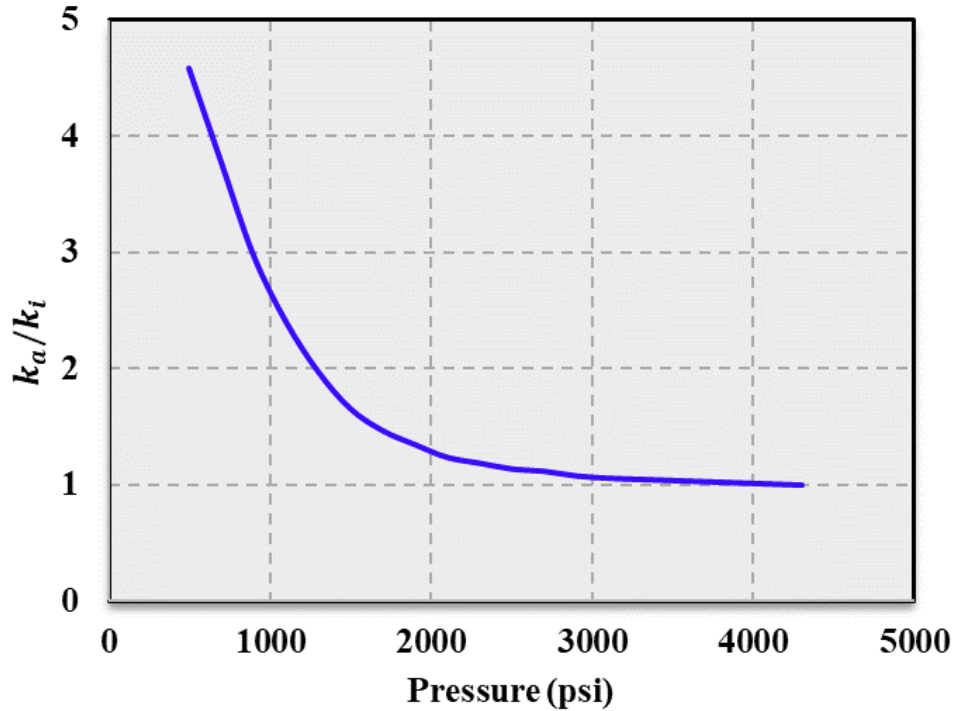
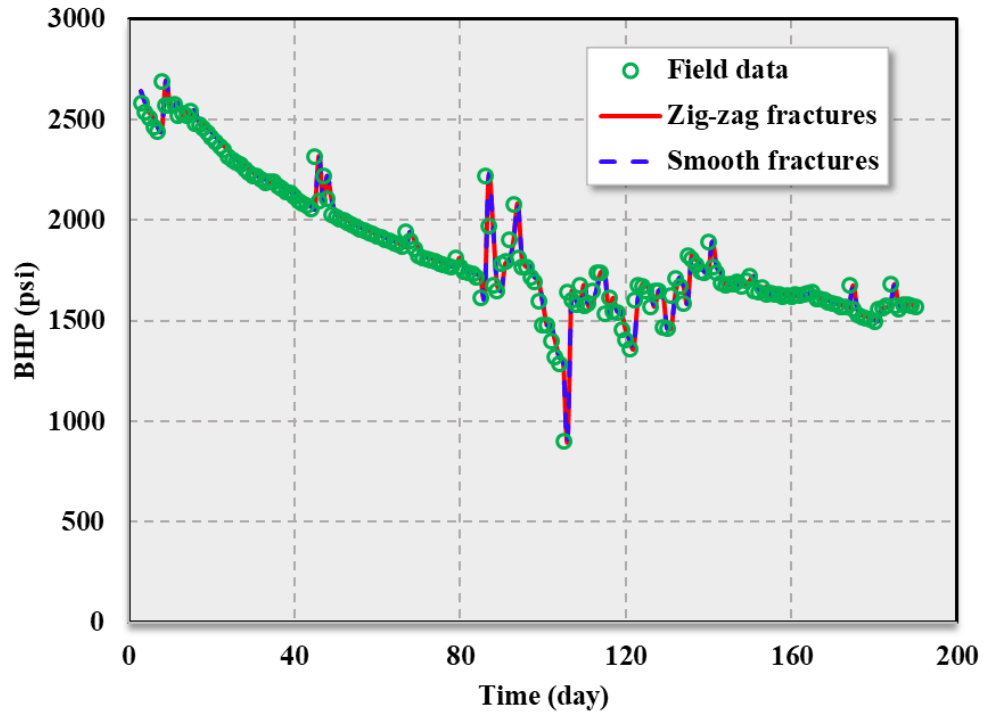


Figure 5.9 LBM simulation of changing ratio of apparent matrix permeability over intrinsic matrix permeability due to pressure change with nanopore size of 10 nm (modified from Yu et al., 2018a).

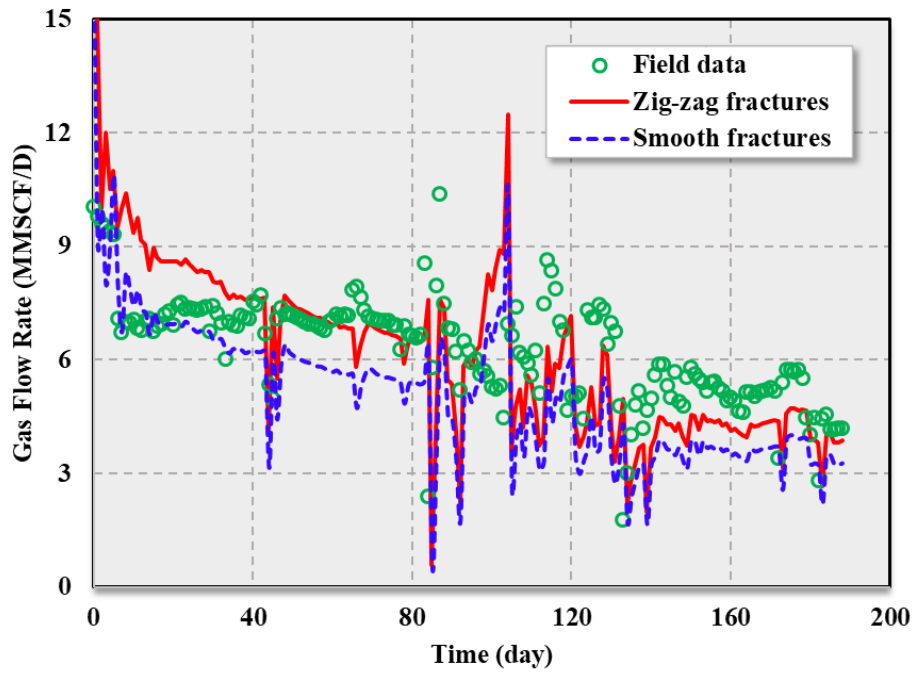
The LBM is applied to simulate the change of apparent matrix permeability during reservoir depletion for the two cases with nanopore size of 10 nm, as presented in Figure 5.9. It is implied that when bottomhole pressure (BHP) is close to 4300 psi, the apparent permeability ( $k_a$ ) is almost equal to the intrinsic matrix permeability ( $k_i$ ) of the reservoir, while  $k_a$  is about 4.6 times of the  $k_i$  as BHP reduces to 500 psi. The results confirm that the apparent matrix permeability  $k_a$  increases as pressure decreases due to the effect of gas slippage, since  $k_i$  is constant (Javadpour et al., 2007; Yu et al., 2018a).

The simulated BHP was set to be the same with the field BHP, as shown in Figure 5.10(a). The gas flow rate histories simulated by moving tip clustering and linear regression clustering algorithms were compared with the field data, as are presented in Figure 5.10(b). The predicted

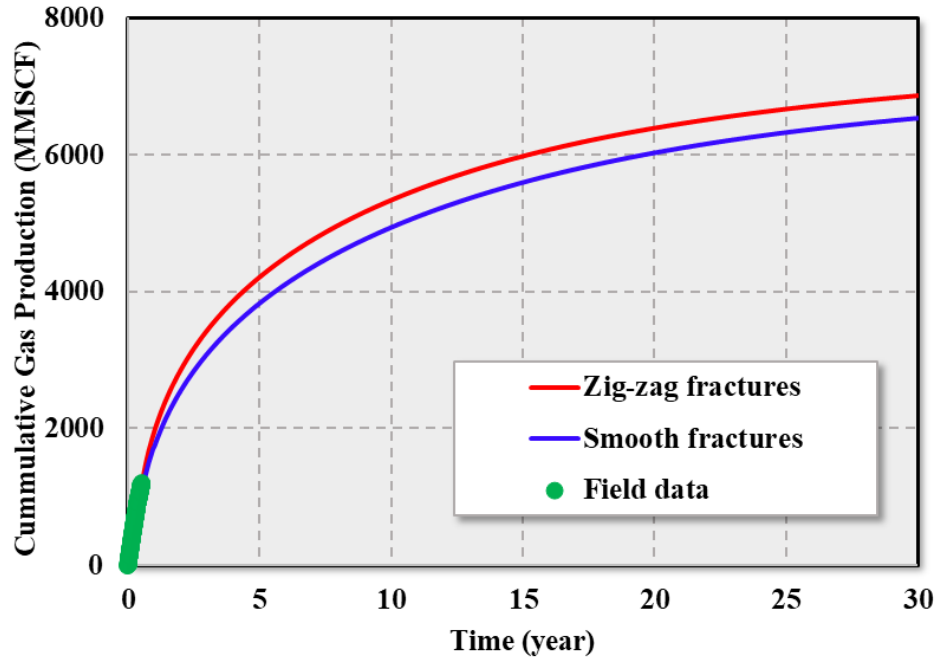
cumulative gas productions in 30 years for the two approaches are presented in Figure 5.10(c). The zig-zag fractures correspond to the moving tip clustering algorithm whereas the smooth fractures are the results of the linear regression clustering algorithm. It is observed from Figure 5.10(b) that the simulated production rates by zig-zag fractures can be matched with the field data when fracture conductivity is 4 md-ft, while the simulated daily production from the smooth fractures are smaller than the field data under the same conditions. Figure 5.10(c) further shows that that the zig-zag fractures contribute to an additional 5.2% gas production in 30 years than that of the smooth fractures when the same fracture conductivities were used. Since the zig-zag fractures given by the moving tip clustering algorithm have larger apparent fracture lengths than the smooth fractures given by the linear clustering algorithm, the zig-zag fractures contribute to larger SRV, thus leading to larger simulated production rate and cumulative production. There is little difference between pore pressure distribution for zig-zag and smooth fractures for same period of production, as suggested from Figure 5.11 and Figure 5.12. The results indicate that the contribution of production from microcracks is insignificant compared to that from major fracture paths.



(a) BHP history in 190 days

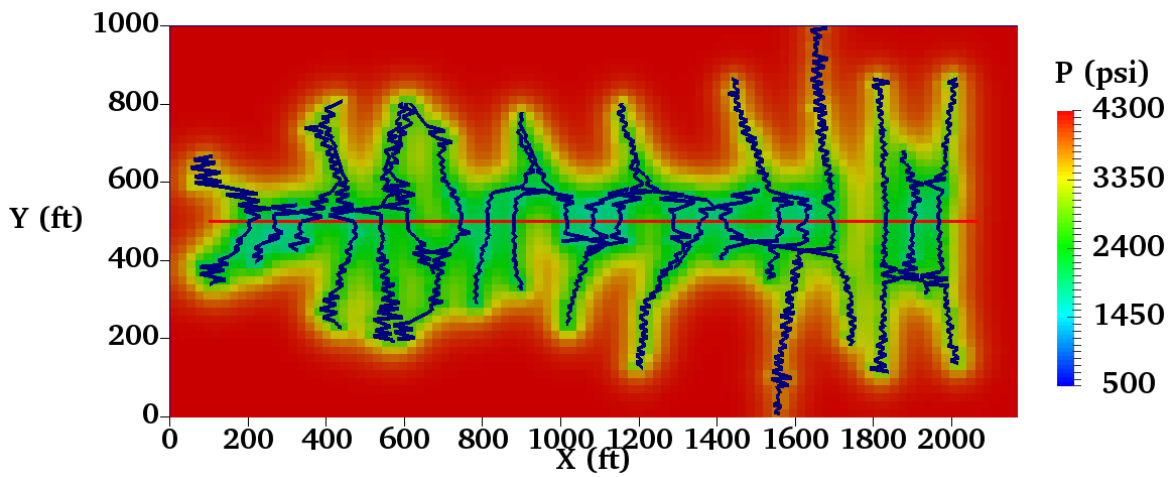


(b) Gas production rate in 190 days

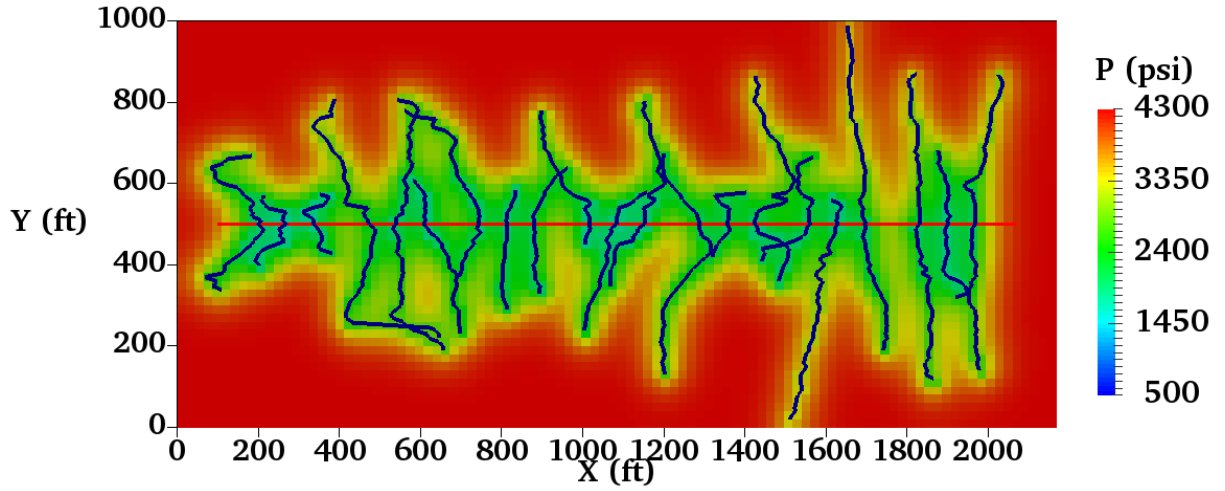


(c) Gas production prediction for 30 years

Figure 5.10 Comparison of bottomhole pressure and gas production data using zig-zag and smooth fractures with field data.

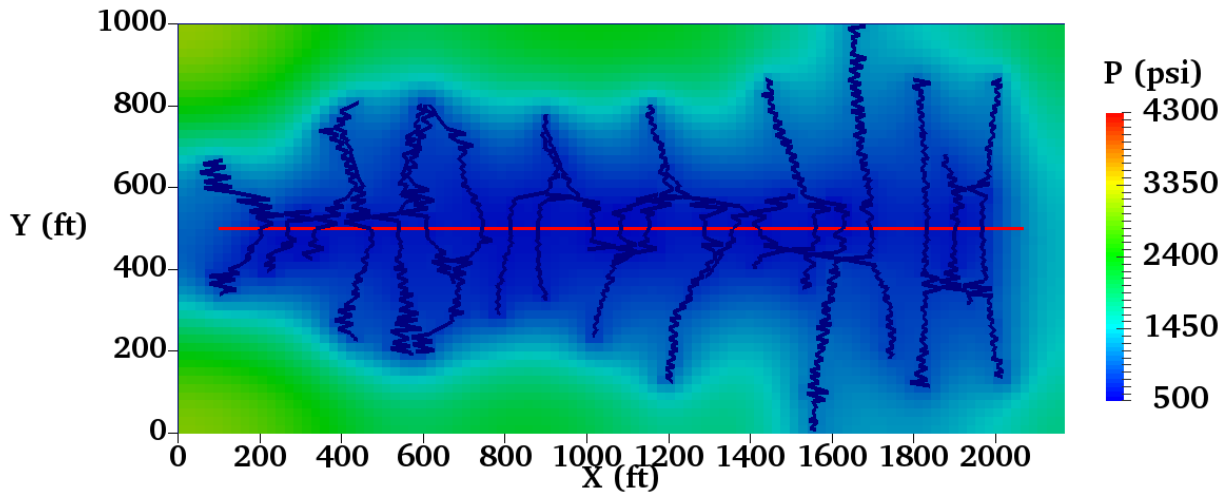


(a)

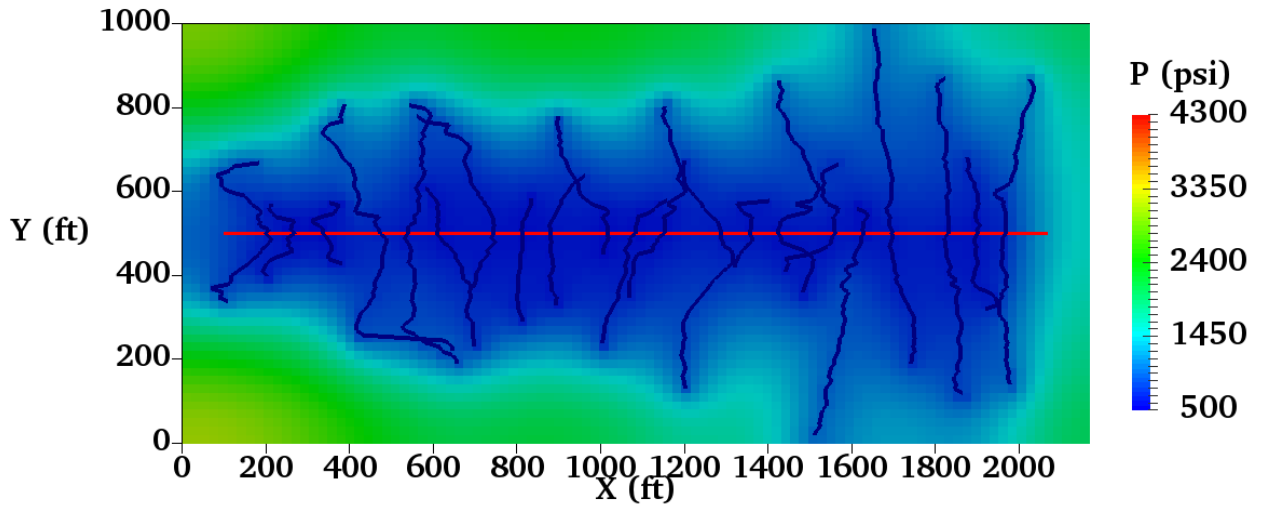


(b)

Figure 5.11 Comparison of pore pressure distribution after 190 days of production using: (a) zig-zag fractures, (b) smooth fractures.



(c)



(d)

Figure 5.12 Comparison of pore pressure distribution after 10 years of production using: (a) zig-zag fractures, (b) smooth fractures.

The change of matrix permeability and fracture conductivity due to decline of BHP were investigated. As BHP decreases, both fracture and reservoir matrix pores will close. Fracture closure is characterized using:

$$\log\left(\frac{C_f}{C_i}\right) = -0.004p_c + 0.2191, R^2 = 0.998, \quad (15)$$

where  $C_f$  is the fracture conductivity after production,  $C_i$  is the initial fracture conductivity,  $\frac{C_f}{C_i}$  represents normalized fracture conductivity, and  $p_c$  is the fracture closure pressure (Yu et al., 2018a).

Jones (1988) proposed an empirical equation to describe change of matrix permeability due to pressure decline:

$$\frac{k_m}{k_i} = \frac{e^{[a_k(e^{-pc/p^*} - 1)]}}{(1 + C_0 pc)}, \quad (16)$$

where  $k_m$  is matrix pressure after depletion,  $k_i$  is original matrix pressure,  $\frac{k_m}{k_i}$  denotes normalized matrix permeability,  $a_k$  is a slop coefficient set to be 1.9,  $p^*$  is decay constant set to be 3000 psi, and  $C_0$  is an arbitrary constant set to be  $3 \times 10^{-6}$  psi (Jones, 1988).

Equations (10) and (11) were used to obtain the curves of both normalized fracture and matrix permeability versus pressure, as shown in Figure 5.13. It is observed that as BHP decreases from initial reservoir pressure of 4300 psi to 500 psi, fracture and matrix permeability reduce 80% and 69%, respectively.

Influence of matrix shrinkage and fracture closure on 30 years of cumulative production are presented in Figure 5.14. Moving tip clustering algorithm was used for all the simulation results. It is observed that fracture closure, matrix shrinkage, and all mechanisms result in cumulative production reduction of 9.25%, 9.28%, and 20.1%, respectively comparing to the case without fracture closure or matrix shrinkage.



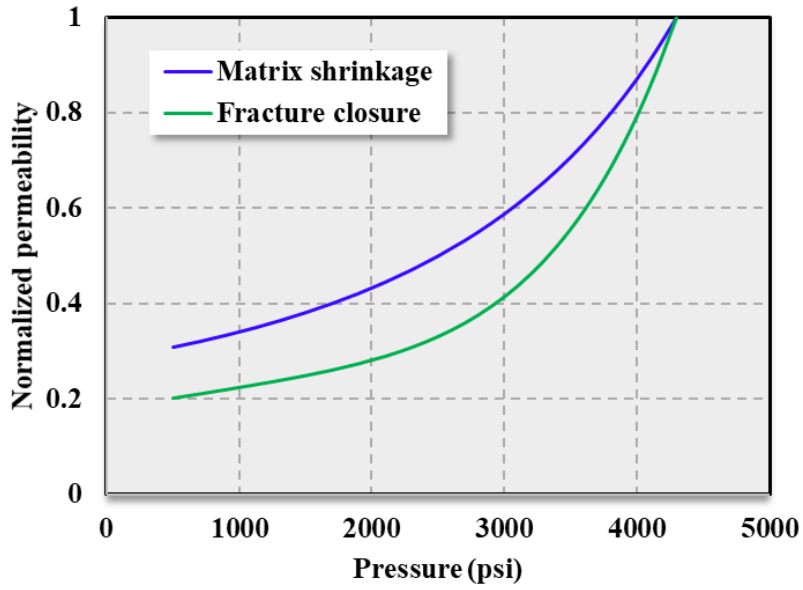


Figure 5.13 Relationship of normalized fracture and matrix permeability over pressure (modified from Yu et al., 2018a).

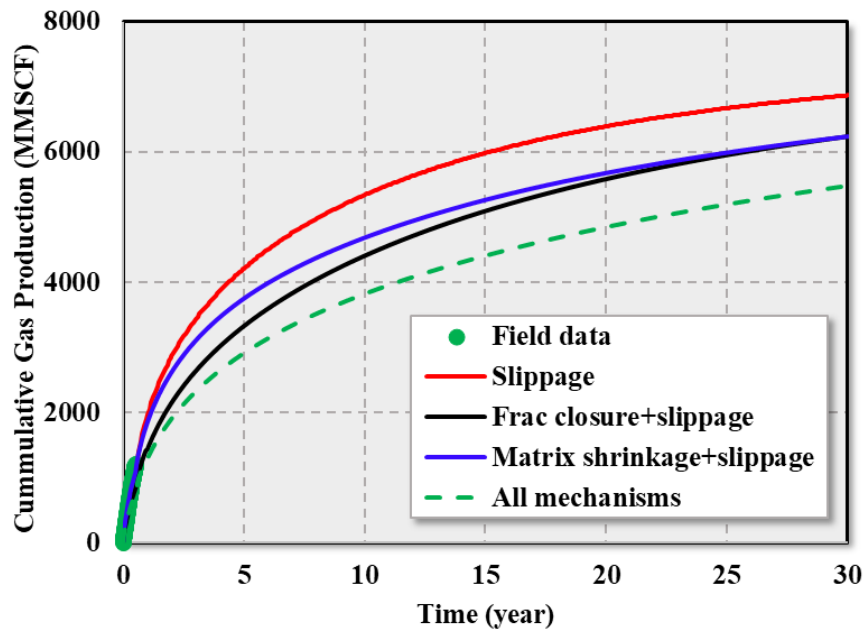


Figure 5.14 Impacts of fracture closure, and matrix shrinkage on cumulative gas production in 30 years.

## 5.7 Summary

In this chapter an integrated model coupling multi-stage hydraulic fracturing and reservoir simulation was built using a lattice based hydraulic fracturing simulator, EDFM method, and a third-party reservoir simulator. The fracture geometry obtained by a hydraulic fracturing simulator was characterized using both moving tip clustering and linear regression clustering algorithms. The former algorithm provides zig-zag fracture paths while the latter generates smooth fracture paths. The obtained fracture paths were imported into the reservoir simulator through the EDFM method which ensures that the reservoir simulator can model hydrocarbon production under complex fracture conditions.

It is observed that the apparent matrix permeability becomes 4.6 times of the intrinsic matrix permeability as BHP declines from the initial 4300 psi to 500 psi, contributing to additional shale gas production. The configuration of fracture path also has a significant impact on gas production. The zig-zag fractures can produce an additional 5.2% shale gas in 30 years than the smooth fractures when fracture conductivity of 4 md-ft was used. The negative impact by both matrix and fracture should be accounted. The pressure-dependent matrix permeability and fracture conductivity result in 9.25% and 9.28% reduction of gas production in 30 years respectively when each effect was accounted separately. The combination effect of matrix shrinkage and fracture closure leads to 20.2% reduction of total gas production in 30 years.

The next chapter will present an integrated model for hydraulic fracturing, production, refracturing, and post-refrac production. Stress reversal regime created by Proppant injection and pore pressure decline will be analyzed. The extent of stress reversal regime on refracture propagation will be investigated.

# Chapter 6

## Integrated Model for Refracturing Optimization

This Chapter is modified from the published paper: Wan et al. (2019).

### 6.1 Introduction

The stimulated volume of the shale as a result of hydraulic fracturing contributes to increase of the relative conductivity and large folds of increase in productivity. However, the side effect is the fast depletion of the reservoir. Therefore, more and more operators and service companies start applying refracturing treatments to enhance productivity after primary production. An integrated model is presented in this paper to simulate the full process of hydraulic fracturing, shale oil production, and refracturing in a horizontal Bakken well. The lattice-based hydraulic fracturing simulator (XSite) was used to simulate the hydraulic fracturing process (Damjanac et al., 2011). The resultant fracture geometry was imported into the continuum modeling software (FLAC3D, 2017) to simulate pore pressure depletion. The pore pressure distribution was imported back to the hydraulic fracturing simulator to calculate stresses and simulate the propagation of the refracture. The simulation results indicated that the production from the horizontal well leads to stress reversal near the initial hydraulic fracture. This effect is favorable for the refracture to propagate perpendicular to the initial hydraulic fracture for growth of branches of secondary fractures at the tip of the initial hydraulic fracture.

## 6.2 Model description

Hydraulic fracturing and refracturing in this chapter were simulated using the lattice-based hydraulic fracturing simulator. Detailed Theory and formulation of this simulator has been discussed in the previous chapters.

Production decline and change of pore pressure distribution were simulated using the continuum modeling software. The software has the capability to build continuum models and simulate fluid flow-mechanical coupling process. The governing differential equations are Transport Law, Balance Law, and Constitutive Laws. In this work, since the coupling effect between pore pressure and mechanical deformation during production is relatively weak, a simplified hydro-mechanical coupling approach was utilized in simulation. The first step was the simulation of pore pressure drawdown, where fluid modulus was modified using equation (6-1) to account for true diffusivity considering deformability of the reservoir (FLAC3D, 2017).

$$K_f^a = \frac{\lambda}{\frac{n}{K_f} + \frac{1}{K + 4/3G}} \quad (6-1)$$

Here,  $K_f$  is the given fluid bulk modulus,  $n$  is porosity,  $K$  is drained bulk modulus,  $G$  is shear modulus.  $\lambda$  is mobility coefficient.  $K_f^a$  is modified fluid bulk modulus.

The pressure field at the end of production was imported in the hydraulic fracturing simulator which is used to calculate the stress changes and deformations associated with depletion. The model equilibrium after hydro-mechanical calculation of depletion is the initial state for simulation of refracturing.

### 6.3 Numerical Simulation

Numerical simulations were conducted for hydraulic fracturing, well production, and production in a horizontal well under typical Middle Bakken Formation properties and stress conditions. For simplification, reservoir model geometry in all simulations was assumed to be cubic with side length  $L = 40 \text{ m}$ . The reference point was located at the center of the right top side of the cube. A horizontal well was placed at the center of the model, as is shown in Figure 6.1. Input parameters for all the simulations were chosen based on typical reservoir rock properties and in-situ stresses of the Middle Bakken Formation, as are shown in Table 6.1. The models were assumed to be homogeneous and isotropic in terms of all the rock properties.

Table 6.1 Reservoir properties for numerical simulations

Parameters	Value
Young's modulus, $E$ (GPa)	90
Poisson's ratio, $\nu$	0.2
Uniaxial compressive strength, $UCS$ (MPa)	130
Tensile strength, $T$ (MPa)	13
Fracture toughness, $KIC$ (MPa · m <sup>0.5</sup> )	1
Friction angle, $\phi$ (°)	37
Permeability, $k$ (mD)	0.001
Porosity, $n$ (%)	1
Vertical stress, $\sigma_v$ (MPa)	69
Maximum horizontal stress, $\sigma_H$ (MPa)	62
Minimum horizontal stress, $\sigma_h$ (MPa)	55
Reservoir pressure, $P_p$ (MPa)	30

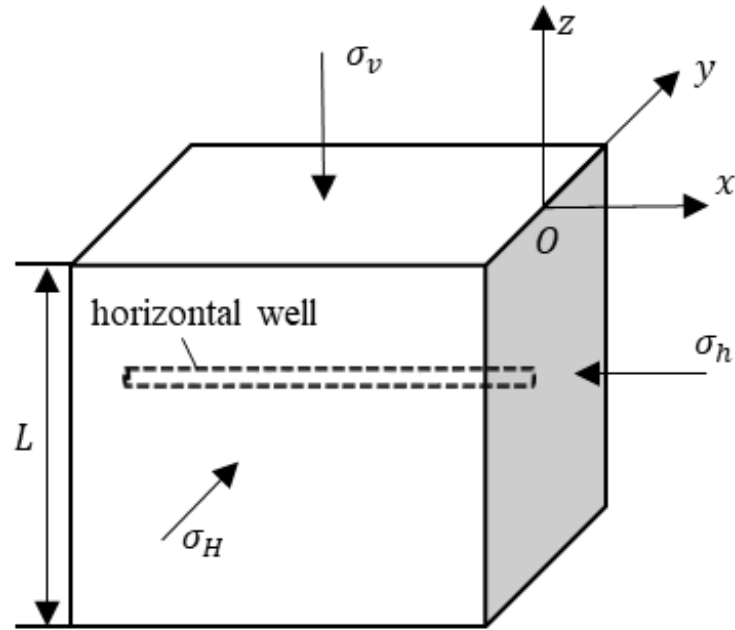


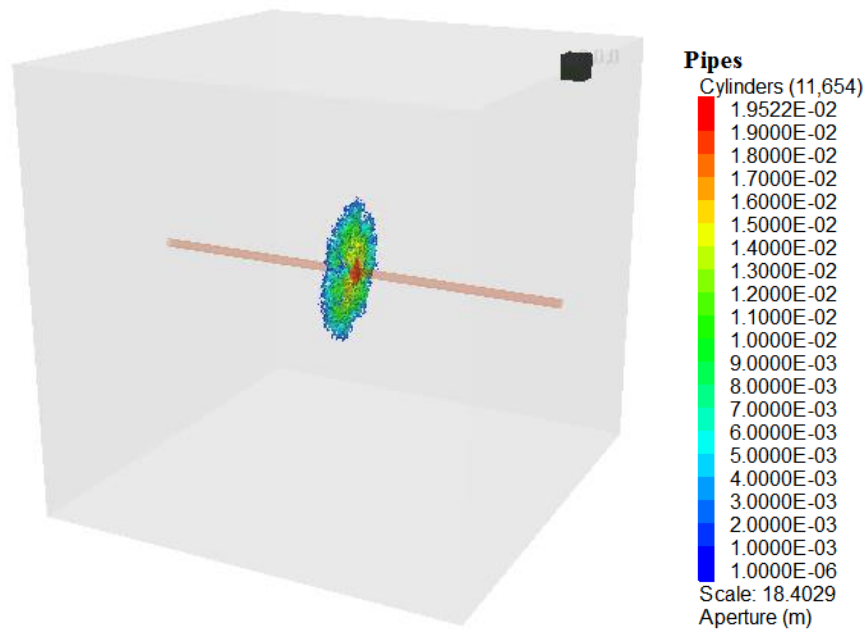
Figure 6.1 Reservoir model and horizontal well geometry used for simulations

### 6.3.1 Hydraulic fracturing simulation

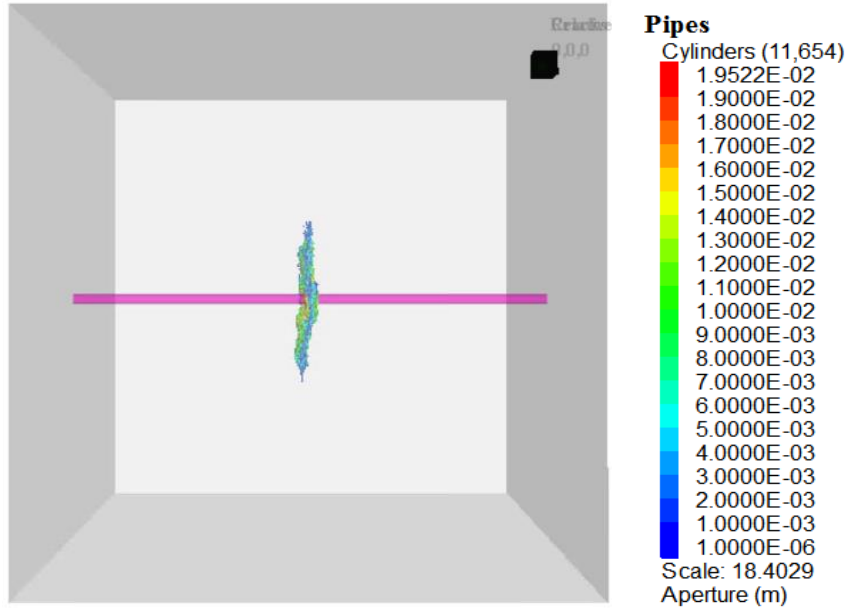
The hydraulic fracturing simulator was used to simulate hydraulic fracturing in the Middle Bakken Formation. The reservoir model and stress conditions were shown in Figure 6.1. Lattice resolution was set to be 0.4 m, thus there were 100 cells in each side of the cube and a total of 1,000,000 cells in the reservoir model. The pumping schedule was simplified by injecting slick water with viscosity of 1 cP ( $0.001 Pa \cdot s$ ) at constant injection rate of  $0.078 m^3/s$  (about 30 BPM). The hydraulic fracturing simulator used 40-70 Ottawa Sand as the default proppant. The proppant concentration was set to be  $30 kg/m^3$  during the injection. The slurry was injected at the center of the wellbore for 10 s and a penny shaped hydraulic fracture with a radius of about 6 m was obtained as are shown in Figure 6.2. The fracture geometry is not ideally symmetric because the mechanical properties of the micro-scale lattices and springs were randomly assigned to match that of the macro-scale model. In the field, a hydraulic fracturing operation will take several hours

and the hydraulic fracture will be as large as 100 m. In this work, however, a small fracture was created in order to avoid the boundary effect. The result shows that the hydraulic fracture has been initiated and propagated perpendicular to the x direction, i.e. the  $\sigma_h$  direction.

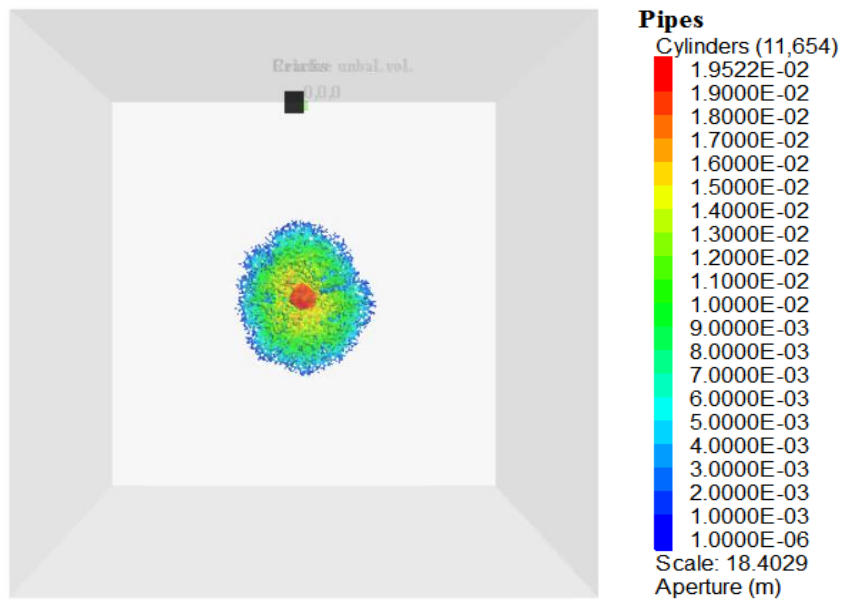
During the simulation of hydraulic fracturing, proppants were filled into the induced fractures, resulting in high permeability ( $> 1$  darcy) in the hydraulic fracture zones. This high permeability zone was used to represent the geometry of hydraulic fracture and was imported into the continuum modeling software to simulate production from the hydraulic fractured well, as is shown in the dark blue zones in Figure 6.4(a).



(a)



(b)



(c)



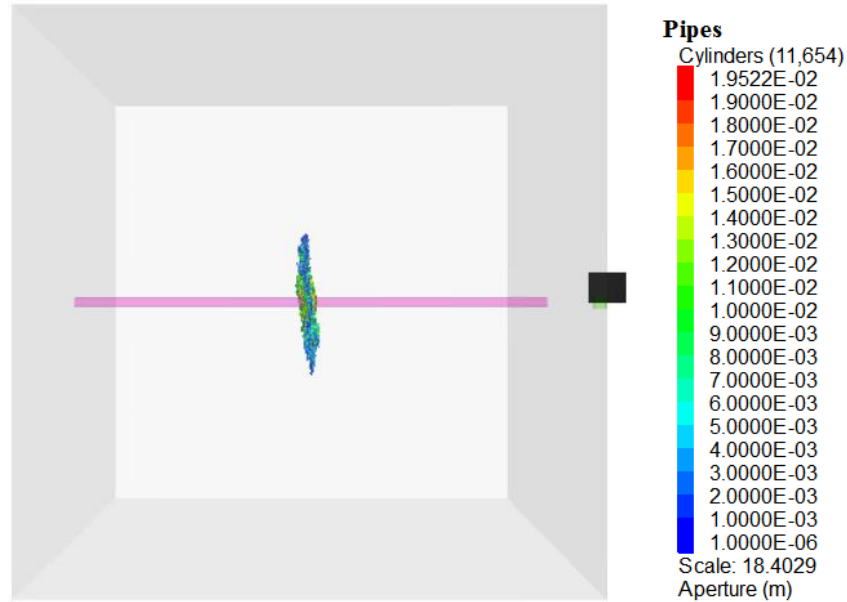


Figure 6.2 Reservoir model, well location and aperture contours for hydraulic fracture (a) general view, (b) front view, (c) side view, (d) top view

### 6.3.2 Well production simulation

The volume of the fracture zones could be considered as the stimulated reservoir volume (SRV) which contained the hydraulic fractures. Since permeability of SRV is much larger than that of reservoir matrix, the pressure decline would be much faster in the SRV than that of the reservoir matrix during oil production. Therefore, it could be expected that the pressure of the fracture zones would quickly drop to the magnitude of bottomhole pressure (BHP) during oil production. Therefore, the boundary conditions for the continuum modeling software models are as followings:

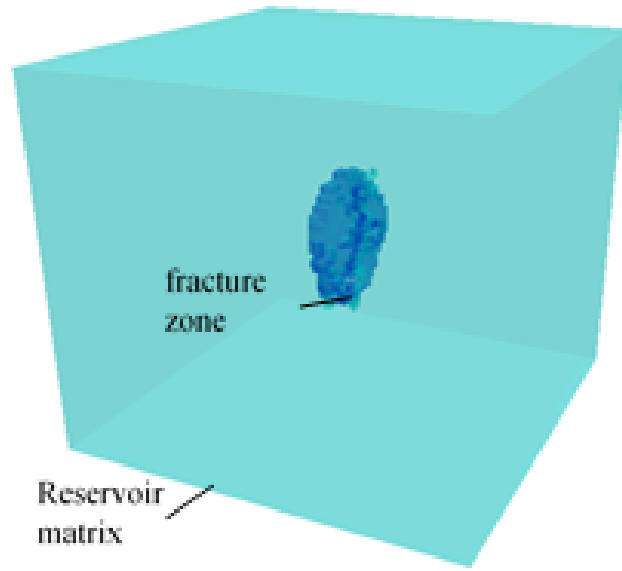
Initial constant reservoir pressure in the reservoir matrix:  $p_i = 30 \text{ MPa}$ ;

Constant pressure in the fracture zones equal to BHP:  $p_w = 10 \text{ MPa}$ ;

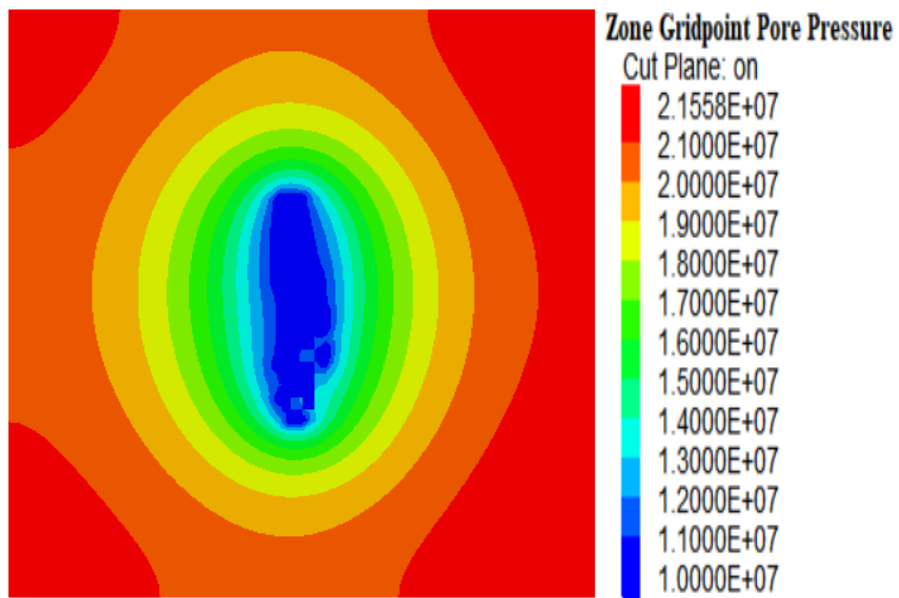
No-flow at the model boundaries:  $-40 \text{ m} < x < 0, -20 \text{ m} < y < 20 \text{ m}, -40 \text{ m} < z < 0$ ;

Constant stresses applied to the model boundaries:  $\sigma_{zz} = \sigma_v = 69 \text{ MPa}$ ,  $\sigma_{yy} = \sigma_H = 62 \text{ MPa}$ ,  $\sigma_{xx} = \sigma_h = 55 \text{ MPa}$ ;

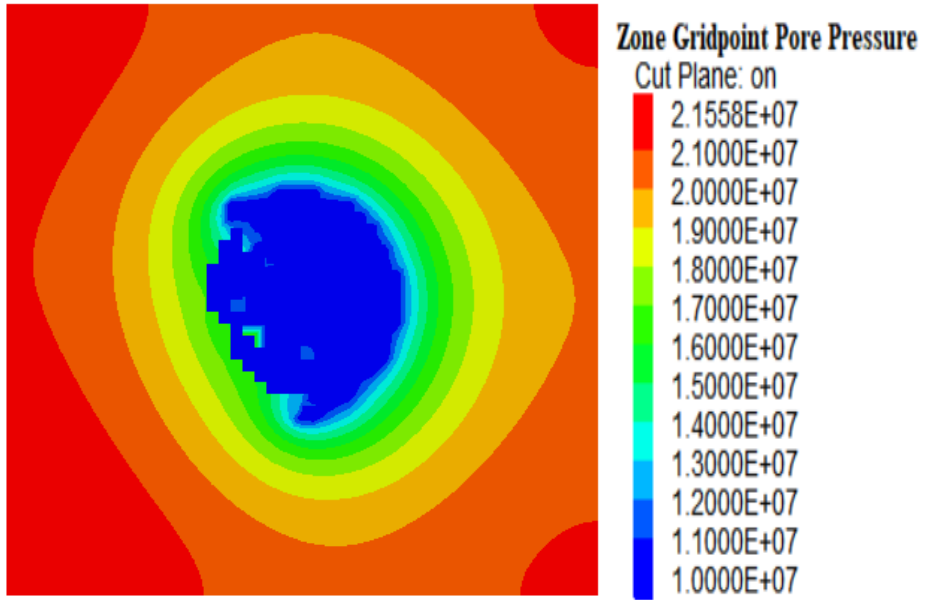
The stress distribution before production was calculated in the hydraulic fracturing simulator, as is shown in Figure 6.4. Then the model was simulated in the continuum modeling software for one year of well production, as shown in Figure 6.3. The simulated pore pressure distribution was imported back to the hydraulic fracturing simulator for calculation of stresses. After one year of well production, the pore pressure decreases faster near fracture zone than away from the fracture zones, as is shown in Figure 6.3. Due to the reservoir depletion and the change of pore pressure, the minimum horizontal stress near the fracture tip rotates and decreases in magnitude, as is observed by comparing Figure 6.5(c) with Figure 6.4(c). Before depletion, the minimum horizontal stresses near the fracture tip are generally in the x direction, as is observed in Figure 6.4(c), thus they are favorable for the fracture to propagate in the initial direction. After depletion, the minimum horizontal stresses near the fracture tip rotate to the y direction, as is observed in Figure 6.5(c). The stress rotation results from the change of pore pressure and creates a stress reversal regime near the fracture tip. The red areas in Figure 6.4(a) and (b) represent stress shadow, i.e., minimum and maximum horizontal stress increase due to injection proppant embedment. These areas show insignificant change after production simulation, as shown in Figure 6.5(a) and (b). This is because fracture closure during production due to proppant loss is not simulated, thus the stress shadow by proppant may be overestimated. Further investigation should be done on whether proppant embedment or reservoir depletion dominates growth of stress shadow area.



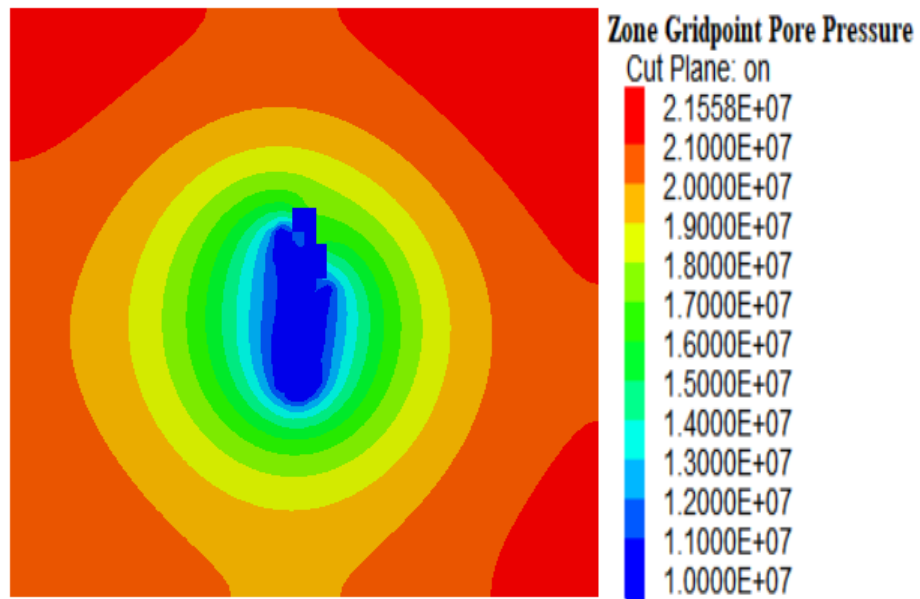
(a)



(b)

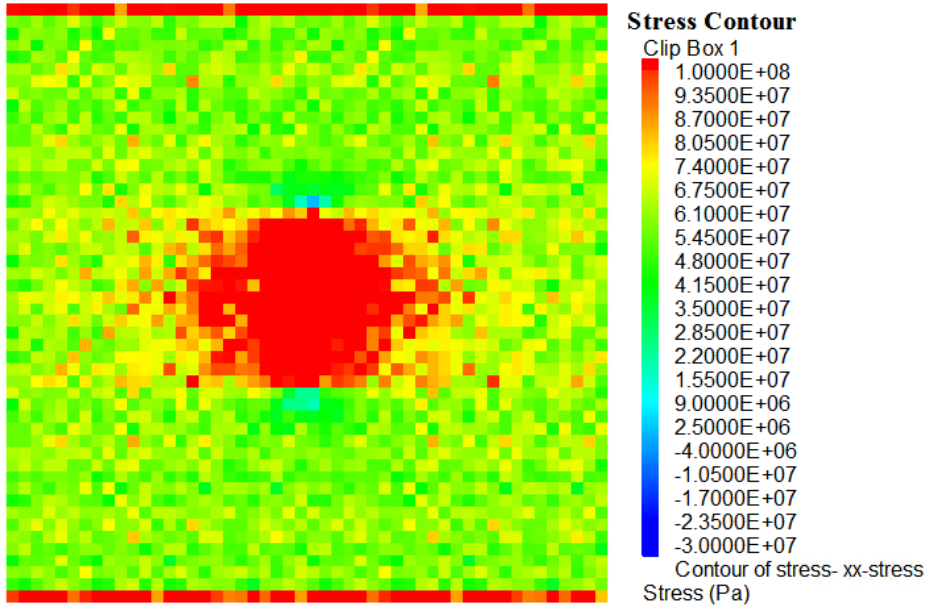


(c)

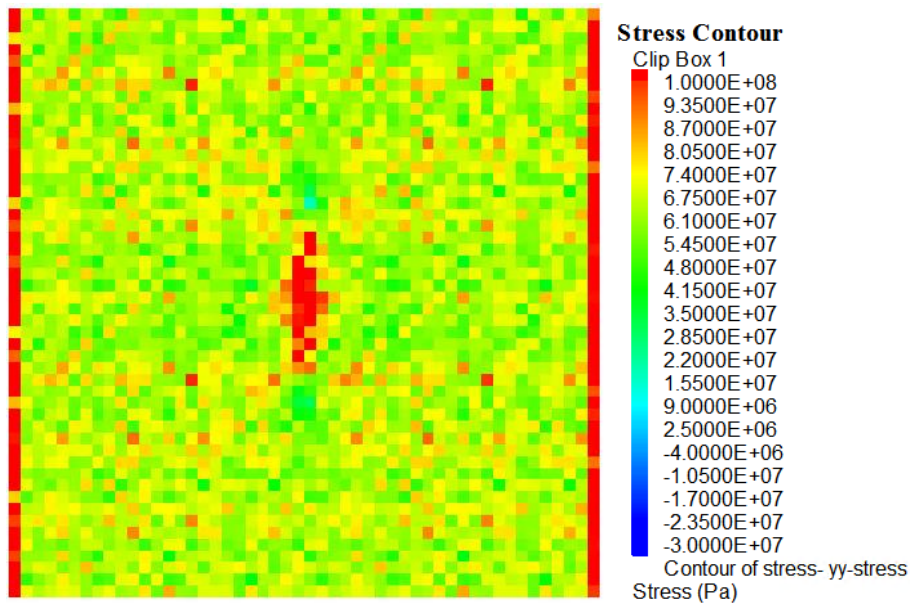


(d)

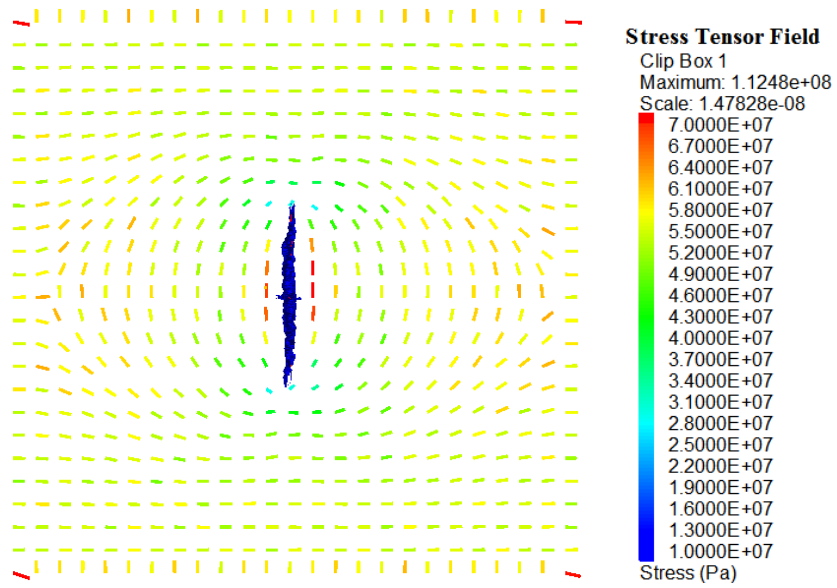
Figure 6.3 Model geometry (a) and pore pressure contours after 1 year of production: (b) center XZ plane, (c) center YZ plane, (d) center XY plane



(a)

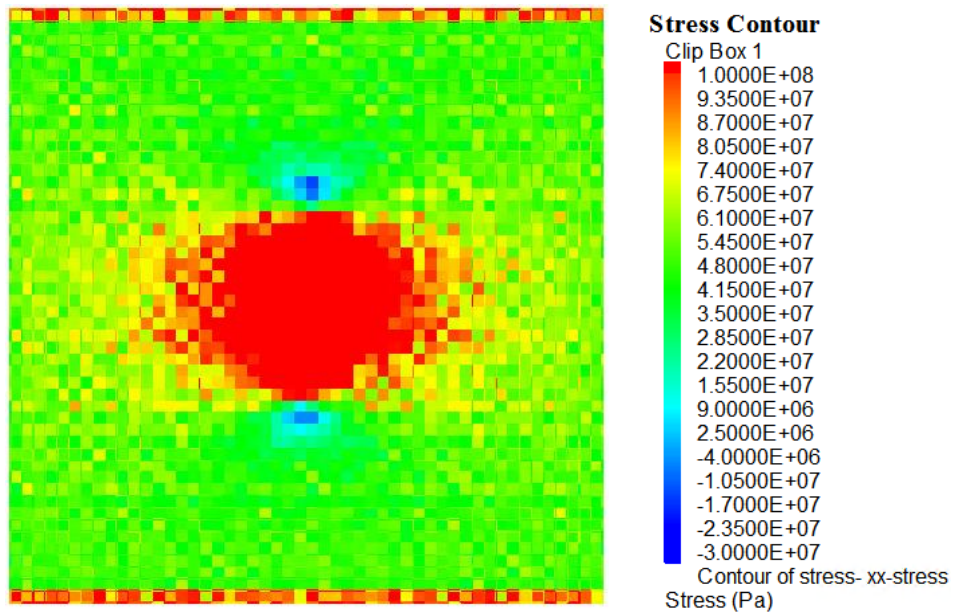


(b)

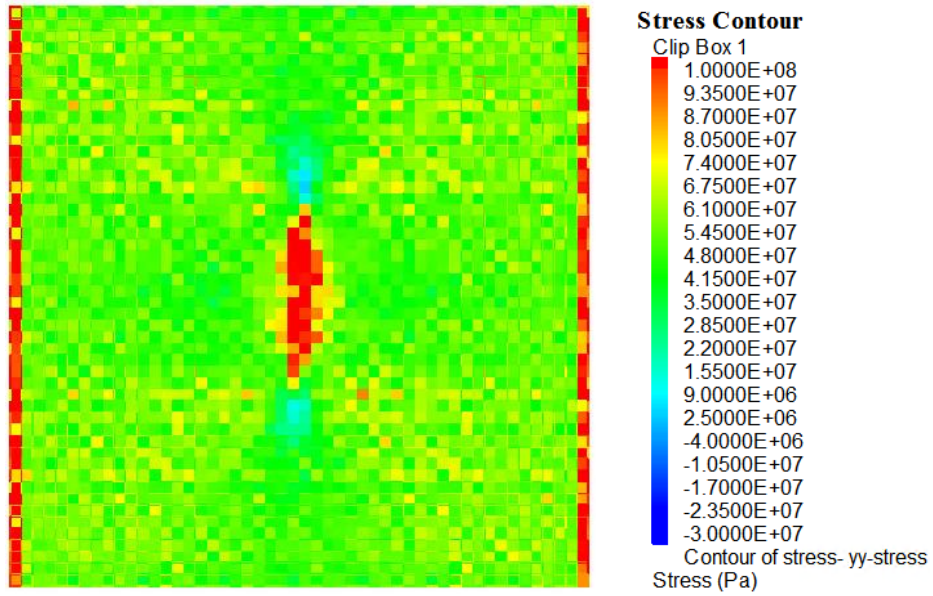


(c)

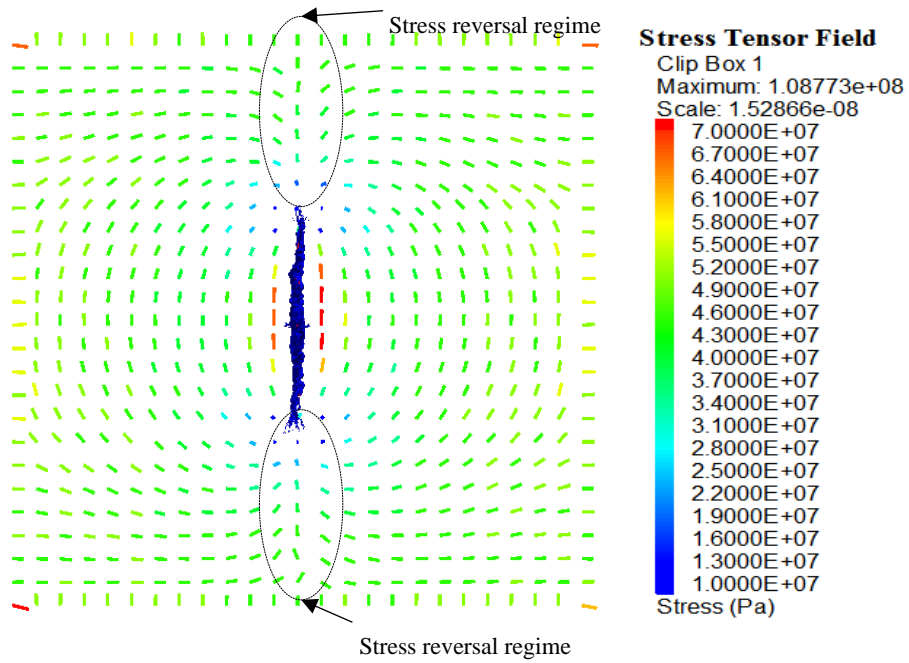
Figure 6.4 Distribution of total stresses before well production at the center XY plane: (a) x direction total stress  $\sigma_{xx}$ , (b) y direction total stress  $\sigma_{yy}$ , (c) tensor field of the minimum horizontal stress



(a)



(b)

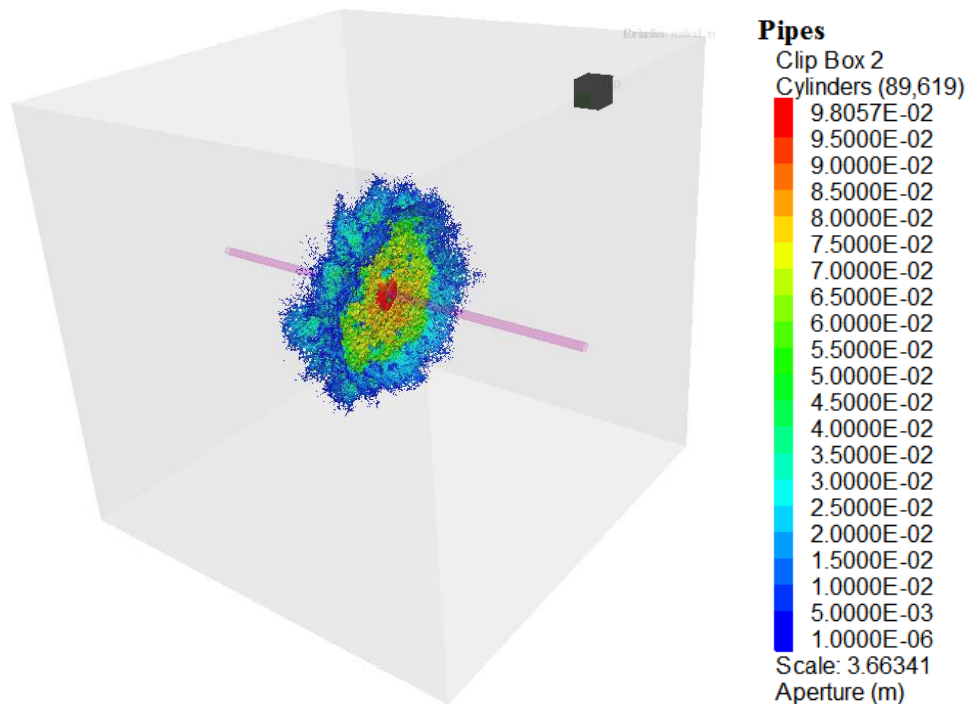


(c)

Figure 6.5 Distribution of total stresses after 1 year of production at the center XY plane: (a) contour of x direction total stress  $\sigma_{xx}$ , (b) contour of y direction total stress  $\sigma_{yy}$ , (c) tensor field of the minimum horizontal stress

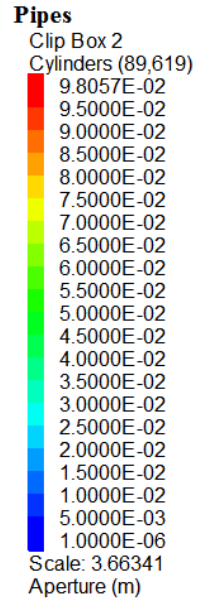
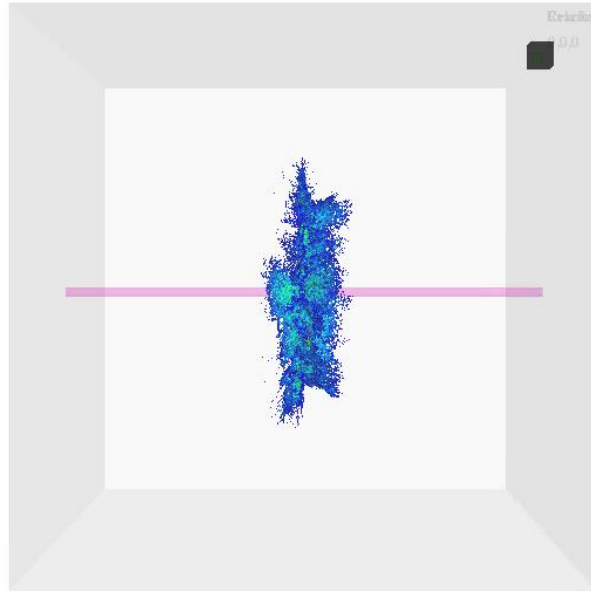
### 6.3.3 Refracturing simulation

Pore pressure distribution obtained from well production simulation in the continuum modeling software was imported back to the previous hydraulic fracturing model to simulate refracturing. The simulation was run for another 100 s with a larger injection rate of  $0.156 \text{ m}^3/\text{s}$  (about 60 BPM) and a larger proppant concentration of  $60 \text{ kg}/\text{m}^3$ . The fracturing fluid was kept the same with the previous hydraulic fracturing simulation. It was observed that several branches of secondary fractures were initiated and propagated perpendicular to the initial maximum horizontal stress direction near the tip of the initial hydraulic fracture, as is shown in Figure 6.6. The observation is corresponding to the stress reversal regime indicated by Figure 6.5(c). The results suggest refracturing operation can create multiple secondary fractures near the tip of the initial hydraulic fracture where stress reversal occurs, thus potentially increasing SRV and boosting production after the operation.

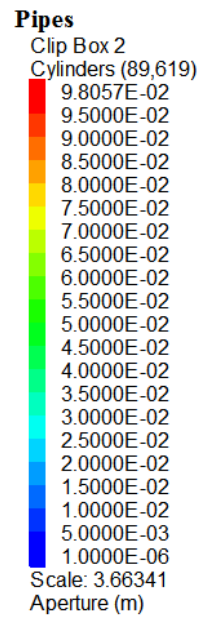
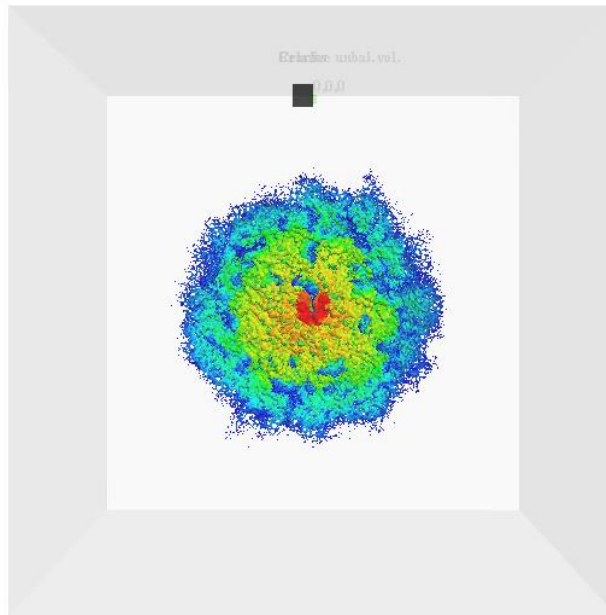


(a)

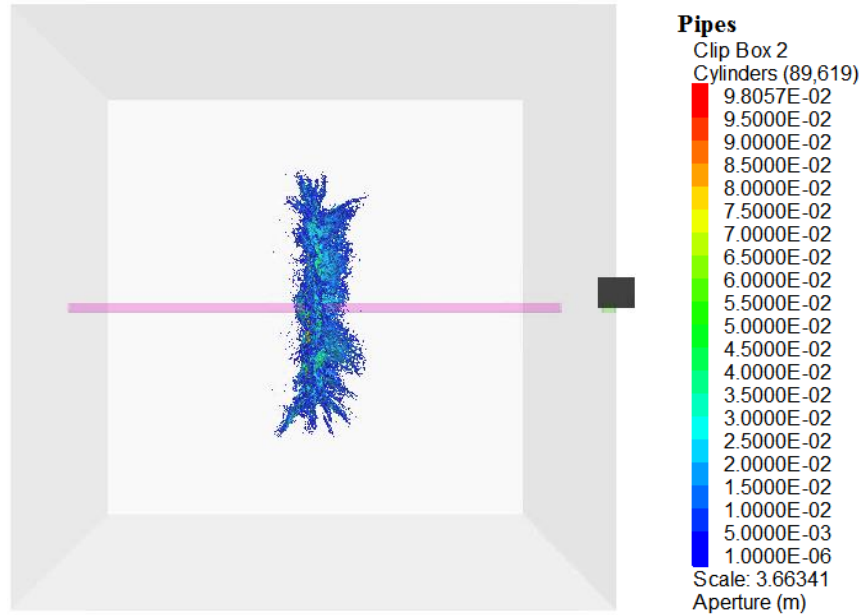




(b)



(c)

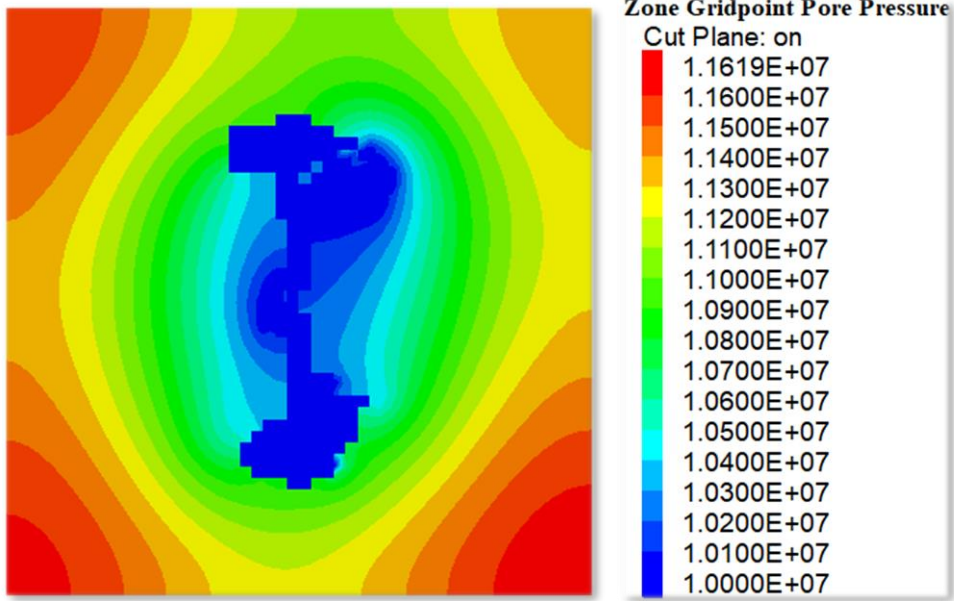


(d)

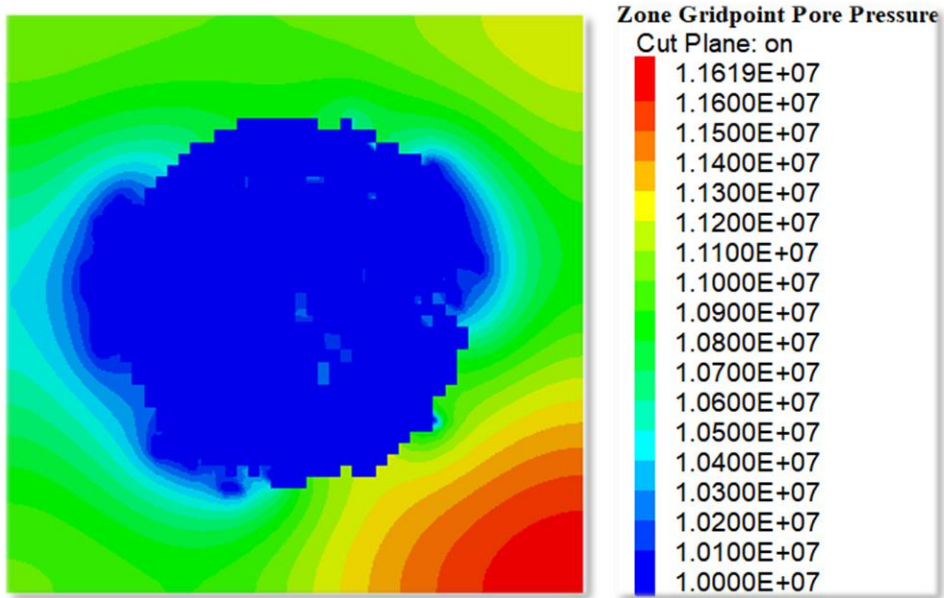
Figure 6.6 Reservoir model, well location and aperture contour for initial hydraulic fractures and refractures: (a) general view, (b) front view, (c) side view, (d) top view

#### 6.3.4 Post refracturing production simulation

The fracture geometry simulated from the hydraulic fracturing simulator was imported back into the continuum modeling software for production prediction after refracturing. The pore pressure after primary production, as shown in Figure 6.3, was used as the initial condition of the post refracturing production simulation. Pressure in fracture and bottomhole was set to be 1000 psi. After 1 year of post refracturing production simulation, the pore pressure near the model boundary drops significantly from about 21 MPa to less than 12 MPa, as observed in Figure 6.7, indicating refracturing contributes to fast depletion. Further investigation is needed to analyze production decline in primary and post refracturing production.



(a)



(b)

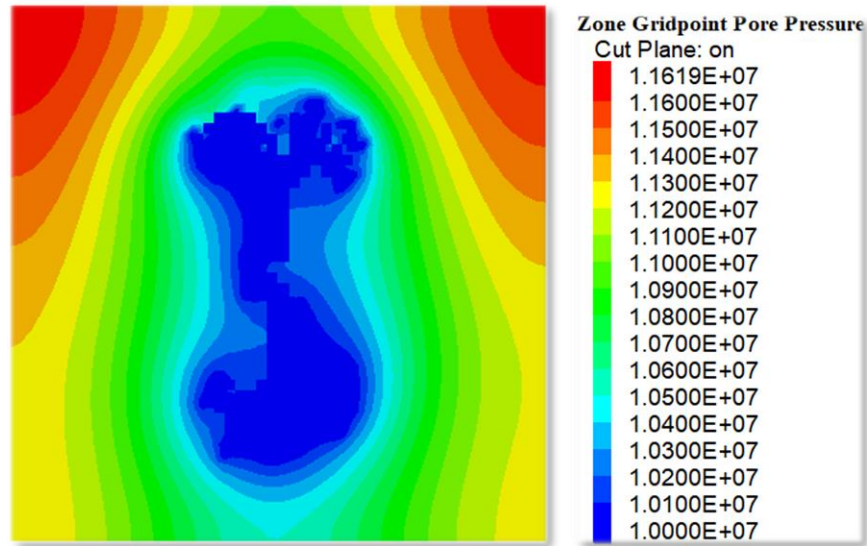


Figure 6.7 pore pressure contours after 1 year of production: (a) center XZ plane, (b) center YZ plane, (c) center XY plane

## 6.4 Summary

In this chapter a new integrated hydraulic fracturing-production-refracturing model was proposed using a lattice based software with coding in a continuum modeling software. Simulation results using the Middle Bakken Formation rock properties and stress data showed that the initial hydraulic fracture was initiated and propagated perpendicular to the minimum horizontal stress direction. The fracture propagation created a stress reversal regime near the hydraulic fracture. After simulating one year of well production using constant bottom hole pressure, stress reversal regime was observed to expand. The stress reversal regimes is favorable for the propagation of the refractures. During refracturing simulation, it was observed that the initial hydraulic fracture grew into several branches near the initial fracture tip. The secondary fractures would potentially increase SRV and enhance post-refracturing production.

The findings and recommendations of this dissertation will be summarized in the next chapter.

# Chapter 7

## Conclusions and Recommendations

### 7.1 Conclusions

The main conclusions from this study are summarized below.

- The numerical models for viscosity dominated regime and toughness dominated regime can be verified against analytical results.
- Penetration area and penetration depth were first introduced to quantify degree of fracture containment based on fracture aperture outline.
- Formations with less brittleness and high minimum horizontal stress tend to inhibit fracture growth and cause containment.
- Innovative multi-stage hydraulic fracturing and production model using XSite, EDFM, and CMG were proposed to ensure simulating production from complex fracture geometry.
- Two newly proposed algorithms ensures transforming distributed fracture data points into multiple linear crack segments, so that the fracture geometry can be transferred into the reservoir simulator CMG for production history matching.

- Moving tip clustering algorithm detects both major fracture paths and microcracks, thus production from both fractures and SRV can be included for reservoir simulation.
- Linear regression clustering algorithm is more accurate in terms of capturing major fracture paths, however, less contribution from microcracks may cause underestimation of simulated production.
- For shale gas production simulation, the lesson that can be learnt from this work is that gas slippage, matrix shrinkage, and fracture play important roles in shale gas production. Thus they should not be excluded in reservoir simulation of shale gas.
- The newly proposed integrated hydraulic fracturing, production, refracturing, and post-refracturing production model presented in Chapter 6 is a creative approach to include fracture propagation, stress change, and pore pressure depletion in a coupled model using XSite and FLAC3D.
- The modeling results of the integrated model in Chapter 6 imply stress reversal at fracture tip due to reservoir depletion. This regime favors refracture to propagate perpendicular to existing hydraulic fracture, thus potentially improving SRV and boosting production.
- The simulation results in Chapter imply that both proppant imbedment and reservoir depletion can cause stress shadow which favors refracture to propagate with different orientation.

## **7.2 Recommendations and Future Works**

Recommendations from this study and potential future works are summarized below.

- The brittleness mentioned in Chapter 4 refers to larger stiffness, i.e., higher Young's modulus and low Poisson's ratio in this work. The brittleness impact on fracture propagation from mineralogy, rock strength, and energy criteria perspectives may need further investigation.
- For future investigation of reservoir simulation from complex fracture geometry, the proposed clustering algorithms should be cautiously be chosen for simulation purposes.
- The proposed clustering algorithms can potentially be compared to microseismic analysis taking into account that microseismic data obtained from field are also in the forms of distributed data points.
- The multi-stage hydraulic fracturing model presented in Chapter 5 shows relatively large stress shadow effect possibly because well shut-in between stages were not included in the simulation. Future works can further investigate the impact of fracture closure due to well shut-in on stress shadow and fracture interaction.
- In Chapter 6, the possible reason for no growth of refractures at the center of initially hydraulic fracture is that the model assumes initial hydraulic fracture is not sealed by diverters. The effect of diverter on refracture growth should be studied further in the future works.
- The applications of the partial and full process of hydraulic fracturing, production, refracturing, and post-refracturing production models presented in this work may be practiced in field operation. These innovative approaches can potentially be adopted by operators in the future to improve production from unconventional reservoirs.





## References

- Adachi, J., Siebrits, E., Peirce, A., and Desroches, J. (2007). Computer simulation of hydraulic fractures. *International Journal of Rock Mechanics and Mining Sciences*, 44(5), 739-757.
- Advani, S. H., Lee, T. S., and Lee, J. K. (1990). Three-Dimensional Modeling of Hydraulic Fractures in Layered Media: Part I—Finite Element Formulations. *Journal of Energy Resources Technology*, 112(1), 1-9.
- Bakhshi, E., Rasouli, V., Ghorbani, A., Marji, M. F., Damjanac, B., and Wan, X. (2018). Lattice Numerical Simulations of Lab-Scale Hydraulic Fracture and Natural Interface Interaction. *Rock Mechanics and Rock Engineering*, 1-23.
- Blanton, T. L. (1982). An Experimental Study of Interaction Between Hydraulically Induced and Pre-Existing Fractures. SPE-10847-MS, presented at the SPE Unconventional Gas Recovery Symposium. Pittsburgh, Pennsylvania: Society of Petroleum Engineers.
- Bohlooli, B. and Pater, C. J. (2006). Experimental study on hydraulic fracturing of soft rocks: Influence of fluid rheology and confining stress. *Journal of Petroleum Science and Engineering*, 53(1-2), 1-12.
- Chang, H. (2004). Hydraulic Fracturing in Particulate Materials (Doctoral dissertation). Atlanta, Georgia, USA: Georgia Institute of Technology.
- Chen, Y., Guo, N., Wu, D., and Hu, R. (2018). Numerical investigation on immiscible displacement in 3D rough fracture: Comparison with experiments and the role of viscous and capillary forces. *Advances in Water Resources*, 118, 39-48.
- Cheng, Y. (2012). Impact of Water Dynamics in Fractures on the Performance of Hydraulically Fractured Wells in Gas-Shale Reservoirs. *Journal of Canadian Petroleum Technology*, 51(02), 143 - 151.
- Cipolla, C., and Wallace, J. (2014). Stimulated Reservoir Volume: A Misapplied Concept? SPE-168596-MS, presented at the SPE Hydraulic Fracturing Technology Conference. The Woodlands, Texas, USA: Society of Petroleum Engineers.
- Coulter, G. and Menzie, D. (1973). The Design of Refrac Treatments for Restimulation of Subsurface Formations. SPE-4400-MS, presented at the SPE Rocky Mountain Regional Meeting. Casper, Wyoming: Society of Petroleum Engineers.
- Crouch, S. L., and Starfield, A. M. (1983). *Boundary element methods in solid mechanics*. Londer: George Allen and Unwin.
- Cundall, P. A., and Strack, O. D. (1979). A discrete numerical model for granular assemblies. *geotechnique*, 29(1), 47-65.
- Cundall, P. (2011). Lattice method for modeling brittle, jointed rock. Presented at the 2nd International FLAC/DEM Symposium. Melbourne, Australia: Itasca International Inc.

- Dahi-Taleghani, A. (2009). Analysis of hydraulic fracture propagation in fractured reservoirs: an improved model for the interaction between induced and natural fractures (PhD Dissertation). Austin, Texas: The University of Texas at Austin.
- Damjanac, B., Detournay, C., and Cundall, P. A. (2016). Application of particle and lattice codes to simulation of hydraulic fracturing. *Computational Particle Mechanics*, 3(2), 249-261.
- Damjanac, B., Detournay, C., Cundall, P., Purvance, M., and Hazzard, J. (2011). XSite Description of Formulation Revision I. Itasca Consulting Group, Inc.
- Detournay, E., Cheng, A. H., Roegiers, J. C., and McLennan, J. D. (1989). Poroelasticity Considerations in Insitu Stress Determination By Hydraulic Fracturing. *International Journal of Rock Mechanics and Mining Sciences and Geomechanics Abstracts*, 26(6), 507-513.
- Djabekhir, N., Song, X., Wan, X., Akash, O., Rasouli, V., and Damjanac, B. (2019). Notch Driven Hydraulic Fracturing in Open Hole Completions: Numerical Simulations of Lab Experiments. 53rd U.S. Rock Mechanics/Geomechanics Symposium, 23-26 June, New York City, New York.
- Du, S., Yoshida, N., Liang, B., and Chen, J. (2016). Application of Multi-Segment Well Approach: Dynamic Modeling of Hydraulic Fractures. *Journal of Natural Gas Science and Engineering*, 34, 886-897.
- Dusseault, M., McLennan, J. (2011). Massive multi-stage hydraulic fracturing: where are we? 45th American Rock Mechanics Association, e-Newsletter, Winter 2011.
- Fan, L., Thompson, J. W., and Robinson, J. R. (2010). Understanding Gas Production Mechanism and Effectiveness of Well Stimulation in the Haynesville Shale Through Reservoir Simulation. SPE-136696-MS, presented at the Canadian Unconventional Resources and International Petroleum Conference. Calgary, Alberta, Canada: Society of Petroleum Engineers.
- FLAC3D. (2017). FLAC3D version 6.0 documentation. Itasca Consulting Group, Inc.
- Feng, Runhua, et al. (2020). Brittleness Index: From Conventional to Hydraulic Fracturing Energy Model. *Rock Mechanics and Rock Engineering*, 53(2), 739–753.
- Fu, W. and Bungler, A. P. (2019). 3D DEM Simulation on the Interference of Multiple Hydraulic Fractures in Horizontal Wells. 53rd U.S. Rock Mechanics/Geomechanics Symposium, 23-26 June, New York City, New York.
- Fu, W., Savitski, A. A., Damjanac, B., and Bungler, A. P. (2019). Three-dimensional lattice simulation of hydraulic fracture interaction with natural fractures. *Computers and Geotechnics*, 107, 214-234.
- Garagash, D. I., and Detournay, E. (1999). The Tip Region of a Fluid-Driven Fracture in an Elastic Medium. *Journal of Applied Mechanics*, 67(1), 183-192.
- Geertsma, J. and Klerk, F. (1969). A Rapid Method of Predicting Width and Extent of Hydraulically Induced Fractures. *Journal of Petroleum Technology*, 21(12), 1,571-1,581.

- Germanovich, L. N., Hurt, R. S., Ayoub, J. A., Stanchits, S., Norman, D., Ispas, I., Montgomery, C. T. (2012). Experimental Study of Hydraulic Fracturing in Unconsolidated Materials. SPE-151827-MS, presented at the SPE International Symposium and Exhibition on Formation Damage Control, Lafayette, Louisiana, USA: Society of Petroleum Engineers.
- Ghassemi, A., Nygren, A., and Cheng, A. (2008). Effects of heat extraction on fracture aperture: A poro-thermoelastic analysis. *Geothermics*, 37(5), 525-539.
- Gholami, R., Rasouli, V., Sarmadivaleh, M., Minaeian, V., and Fakhari, N. (2016). Brittleness of gas shale reservoirs: A case study from the north Perth basin, Australia. *Journal of Natural Gas Science and Engineering*, 33, 1244-1259.
- Grieser, B., Bray, J. (2007). Identification of production potential in unconventional reservoirs. Production and Operations Symposium, Oklahoma, Society of Petroleum Engineers.
- Guo, S. (2013). Experimental Study on Isothermal Adsorption of Methane Gas on Three Shale Samples from Upper Paleozoic Strata of the Ordos Basin. *Journal of Petroleum Science and Engineering* 110: 132-138.
- Gwaba, D. C., Germanovich, L. N., Hurt, R. S., Ayoub, J. A., and Stanchits, S. (2019). Laboratory Study of Hydraulic Fracturing Behavior of Weakly-Consolidated Sediments Under True-Triaxial Stress Regimes. ARMA-2019-1760, presented at the 53rd U.S. Rock Mechanics/Geomechanics Symposium. New York City, New York: American Rock Mechanics Association.
- Huang, J., Yang, C., Xue, X. and Gupta A. D. (2016). Simulation of Coupled Fracture Propagation and Well Performance under Different Refracturing Designs in Shale Reservoirs. SPE-180238-MS, presented at the SPE Low Perm Symposium, Denver, Colorado.
- Hucka, V. and Das, B. (1974). Brittleness determination of rocks by different methods. *J. Rock Mech*, 11(10), 389-392.
- Ingram, G. M., and Urai, J. L. (1999). Top-seal leakage through faults and fractures: the role of mudrock properties. Geological Society, London, Special Publications, 158, 125-135.
- Itasca. (2008a). PFC2D Version 5.0. Itasca Consulting Group, Inc, Minneapolis.
- Itasca. (2008b). PFC3D Version 5.0. Itasca Consulting Group, Inc, Minneapolis.
- Iwere, F. O., Heim, R. N., and Cherian, B. V. (2012). Numerical Simulation of Enhanced Oil Recovery in the Middle Bakken and Upper Three Forks Tight Oil Reservoirs of the Williston Basin. SPE-154937-MS, presented at the SPE Americas Unconventional Resources Conference. Pittsburgh, Pennsylvania USA: Society of Petroleum Engineers.
- Javadpour, F., Fisher, D., and Unsworth, M. (2007). Nanoscale Gas Flow in Shale Gas Sediments. *Journal of Canadian Petroleum Technology* 46(10): 55-61.
- Jin, L., Hawthorne, S., Sorensen, J., Pekot, L., Bosshart, N., Gorecki, C., Steadman, E., and Harju, J. (2017). Utilization of Produced Gas for Improved Oil Recovery and Reduced Emissions from the Bakken Formation. SPE-184414-MS, presented at the SPE Health, Safety, Security,

Environment, and Social Responsibility Conference - North America. New Orleans, Louisiana, USA: Society of Petroleum Engineers.

Jin, X., Shah, S.N., Roegiers, J.C., Zhang, B. (2015) An integrated petro- physics and geomechanics approach for fracability evaluation in shale reservoirs. SPE J, 20, 518-526.

Joshi, S. D. (2003). Cost/Benefits of Horizontal Wells. SPE-83621-MS, presented at the SPE Western Regional/AAPG Pacific Section Joint Meeting. Long Beach, California: Society of Petroleum Engineers.

Klinkenberg, L.J. (1941). The Permeability Of Porous Media To Liquids And Gases. API-41-200, presented at the Drilling and Production Practice, New York, New York, 1 January.

Kumar, D., Masouleh, S. F., Ghassemi, A., Riley, S. and Elliott, B. (2018). A 3D Geomechanical Analysis of Horizontal Well Refracturing and “Frac- Hits”. ARMA-2018-729, presented at the 52nd U.S. Rock Mechanics /Geomechanics Symposium, Seattle.

Lamont, N. and Jessen, F. W. (1963). The Effects of Existing Fractures in Rocks on the Extension Hydraulic Fractures. Journal of Petroleum Technology, 15(02), 203-209.

Lecampion, B., Desroches, J., Weng, X., Burghardt, J., and Brown, J. E. (2015). Can We Engineer Better Multistage Horizontal Completions? Evidence of the Importance of Near-Wellbore Fracture Geometry From Theory, Lab and Field Experiments. SPE-173363-MS, presented at the SPE Hydraulic Fracturing Technology Conference. The Woodlands, Texas, USA: Society of Petroleum Engineers.

Luan, X., Di, B., Wei, J., Li, X., Qian, K., Xie, J., and Ding, P. (2014). Laboratory Measurements of brittleness anisotropy in synthetic shale with different cementation. 2014 SEG Annual Meeting (pp. 3005-3009). Denver: Society of Exploration Geophysicists.

Martha, L. F., Wawrzynek, P. A., and Ingraffea, A. R. (1993). Arbitrary crack representation using solid modeling. Engineering with Computers, 9(2), 63-82.

Mirzaei, M., and Cipolla, C.L. (2012). A Workflow for Modeling and Simulation of Hydraulic Fractures in Unconventional Gas Reservoirs. SPE-153022-MS, presented at the SPE Middle East Unconventional Gas Conference and Exhibition, Abu Dhabi, UAE, 23-25 January.

Moës, N., Dolbow, J., and Belytschko, T. (1999). A finite element method for crack growth without remeshing. International Journal for Numerical Methods in Engineering, 46(1), 131-150.

Moinfar, A. (2013). Development of an Efficient Embedded Discrete Fracture Model for 3D Compositional Reservoir Simulation in Fractured Reservoirs. PhD dissertation. The University of Texas at Austin.

Nagel, N. B., Zhang, F., Sanchez-Nagel, M. A., and Lee, B. (2013). ISRM-EUROCK-2013-147, presented at the Evaluation of Stress Changes Due to Multi-Stage Hydraulic Fracturing - Consideration of Field Results. ISRM International Symposium - EUROCK 2013. Wroclaw, Poland: International Society for Rock Mechanics and Rock Engineering.

- Nordgren, R. (1972). Propagation of a Vertical Hydraulic Fracture. *Society of Petroleum Engineers Journal*, 12(04), 306-314.
- Olson, J. E. (2004). Predicting fracture swarms - the influence of subcritical crack growth and the crack-tip process zone on joint spacing in rock. *Geological Society, London, Special Publications*, 231(1), 73-88.
- Palmer, I. D., and Carroll Jr., H. (1983). Three-Dimensional Hydraulic Fracture Propagation in the Presence of Stress Variations. *Society of Petroleum Engineers Journal*, 23(06), 870-878.
- Perkins, T. K. (1985). The Effect of Thermoelastic Stresses on Injection Well Fracturing. *Society of Petroleum Engineers Journal*, 25(01), 78-88.
- Perkins, T. and Kern, L. (1961). Widths of Hydraulic Fractures. *Journal of Petroleum Technology*, 13(09), 937-949.
- Pierce, M., Cundall, P., Potyondy, D., and Ivars, D. M. (2007). A synthetic rock mass model for jointed rock. Presented at the 1st Canada-U.S. Rock Mechanics Symposium. Vancouver, Canada: American Rock Mechanics Association.
- Rickman, R., Mullen, M.J., Petre, J.E., Grieser, W.V., Kundert, D. (2008) A practical use of shale petrophysics for stimulation design optimization: all shale plays are not clones of the Barnett Shale. SPE annual technical conference and exhibition. Society of Petroleum Engineers
- Ross, D.J.K., and Bustin, R.M. (2007). Impact of Mass Balance Calculations on Adsorption Capacities in Microporous Shale Gas Reservoirs. *Fuel* 86 (17-18): 2696-2706.
- Roussel, N. P. and Sharma, M. M. (2011). Optimizing Fracture Spacing and Sequencing in Horizontal-Well Fracturing. SPE-127986-PA. *SPE Production & Operations*, 26(02), 173 - 184.
- Rubin, M. (1983). Experimental study of hydraulic fracturing in an impermeable material. *J. Energy Resour. Technol. Trans. ASME*, 105:116-124.
- Sarmadivaleh, M. (2012). Experimental and Numerical Study of Interaction of a Pre-Existing Natural Interface and an Induced Hydraulic Fracture (Doctoral dissertation). Bentley, Western Australia, Australia: Curtin University.
- Savitski, A. A., and Detournay, E. (2002). Propagation of a penny-shaped fluid-driven fracture in an impermeable rock: asymptotic solutions. *International Journal of Solids and Structures*, 39(26), 6311-6337.
- Settari, A., and Cleary, M. P. (1982). Development and Testing of a Pseudo-Three-Dimensional Model of Hydraulic Fracture Geometry. *SPE Production Engineering*, 1(06), 449-466.
- Sharma, M. (2013). Improved Reservoir Access Through Refracture Treatments in Tight Gas Sands and Gas Shales (Report). Austin, Texas: The University of Texas at Austin
- Shou, K.-J., Siebrits, E., and Crouch, S. L. (1997). A higher order displacement discontinuity method for three-dimensional elastostatic problems. *International Journal of Rock Mechanics and Mining Sciences*, 34(2), 317-322.

- Teufel, L. W. and Clark, J. A. (1981). Hydraulic-fracture propagation in layered rock: experimental studies of fracture containment. Joint SPE/DOE symposium. Denver, CO, USA.
- Tripoppoom, S., Xie, J., Yong, R., Wu, J., Yu, W., Sepehrnoori, K., Miao, J., Chang, C., and Li, N. (2020). Investigation of different production performances in shale gas wells using assisted history matching. Hydraulic fractures and reservoir characterization from production data. *Fuel*, 267, 117097.
- U.S. Energy Information Administration. (2019a). International energy statistics-petroleum and other liquids production. <https://www.eia.gov/beta/international/data/browser> (Retrieved in Dec 30, 2019).
- U.S. Energy Information Administration. (2019b). Horizontally drilled wells dominate U.S. tight formation production. <https://www.eia.gov/todayinenergy/detail.php?id=39752> (Retrieved in Nov 24, 2019).
- Vincent, M. (2010). Restimulation of Unconventional Reservoirs: When Are Refracs Beneficial? *Journal of Canadian Petroleum Technology*, 50(05), 36-52.
- Wan, X., Rasouli, V., Damjanac, B., Torres, M., Qiu, D. (2019). Numerical Simulation of Integrated Hydraulic Fracturing, Production and Refracturing Treatments in the Bakken Formation. 53rd U.S. Rock Mechanics/Geomechanics Symposium, 23-24 June, New York, NY, USA.
- Wan, X., Rasouli, V., Damjanac, B., Pu, H. (2020a). Lattice Simulation of Hydraulic Fracture Containment in the North Perth Basin. *Journal of Petroleum Science and Engineering*, 188, 1-18.
- X. Wan, V. Rasouli, B. Damjanac, Yu, W., Li, N., Rabiei, M., Miao, J., Liu, M. (2020b). An Integrated Simulation of Multi-Stage Hydraulic Fracturing and Production Simulation for the Marcellus Shale Gas Reservoir, under review.
- W. Yu, N. Li, M. Rabiei, J. Miao, M. Liu. 'An Integrated Simulation of Multi-Stage Hydraulic Fracturing and Production Simulation for the Marcellus Shale Gas Reservoir', *Fuel*
- Wang, H. (2015). Numerical modeling of non-planar hydraulic fracture propagation in brittle and ductile rocks using XFEM with cohesive zone method. *Journal of Petroleum Science and Engineering*, 135, 127-140.
- Wang, D., Chen, M., Jin, Y., and Chen, Z. (2016). Theoretical and experimental study on fracture network initiation and propagation in shale that considers the capillary effect. *Journal of Natural Gas Science and Engineering*, 34, 486-498.
- Warpinski, N. R., Clark, J. A., Schmidt, R. A., and Huddle, C. W. (1981). Laboratory investigation on the effect of in situ stresses on hydraulic fracture containment. Presented at the Joint SPE/DOE symposium. Denver, CO, USA.
- Warpinski, N. R. and Branagan, P. (1989). Altered-Stress Fracturing. *Journal of Petroleum Technology*, 41(09), 990 - 997
- Wu, K. (2014). Numerical Modeling of Complex Hydraulic Fracture Development in Unconventional Reservoirs (PhD Dissertation). Austin, Texas: The University of Texas at Austin.

- Xing, P., Yoshioka, K., Adachi, J., El-Fayoumi, A., Damjanac, B., and Bungler, A. (2018). Lattice simulation of laboratory hydraulic fracture containment in layered reservoirs. *Computers and Geotechnics*, 100, 62-75.
- Yildirim, B., Durucan, S., Cao, W., Cai, W., Shi, J., Korre, A., Wolf, K-H. (2019). Experimental and Numerical Investigation into Hydraulic Fracture and Natural Fracture Interaction in Shale Formations. 53rd U.S. Rock Mechanics/Geomechanics Symposium, 23-26 June, New York City, New York.
- Yu, W., Luo, Z., Javadpour, F., Varavei, A., and K. Sepehrnoori. (2014). Sensitivity analysis of hydraulic fracture geometry in shale gas reservoirs. *Journal of Petroleum Science and Engineering*, 13, 1-7.
- Yu, W., Hu, X., Wu, K., Sepehrnoori, K., Olson, J. E. (2017). Coupled Fracture-Propagation and Semianalytical Models to Optimize Shale Gas Production. SPE-175109-PA. *SPE Reservoir Evaluation & Engineering* 20(04): 1004-1019.
- Zhang, D., Ranjith, P.G., Perera, M. (2016). The brittleness indices used in rock mechanics and their application in shale hydraulic fracturing: a review. *Journal of Petroleum Science and Engineering*. 143, 158-170.
- Zhang, F., Damjanac, B., and Maxwell, S. (2019). Investigating Hydraulic Fracturing Complexity in Naturally Fractured Rock Masses Using Fully Coupled Multiscale Numerical Modeling. *Rock Mechanics and Rock Engineering*, 1-24.